Theory of optical and THz transitions in carbon nanotubes, graphene nanoribbons and flat nanoclusters

Submitted by

Vasil Saroka

to the University of Exeter as a thesis for the degree of Doctor of Philosophy in Physics, June 2017.

I certify that all material in this thesis which is not my own work has been identified and that no material is included for which a degree has previously been conferred upon me.

. . . .

Vasil Saroka

Abstract

This thesis is devoted to the optical properties of low-dimensional structures based on such two-dimensional materials as graphene, silicene and phosphorene.

We investigate optical properties of a variety of quasi-one dimensional and quasi-zero-dimensional structures, which are promising for future optoelectronics. Primarily we focus on their low-energy optical properties and how these properties are influenced by the structures' geometry, external fields, intrinsic strain and edge disorder.

As a consequence of this endeavor, we find several interesting effects such as correlation between the optical properties of tubes and ribbons whose periodic and 'hard wall' boundary conditions are matched and a universal value of matrix element in narrow-gap tubes and ribbons characterizing probability of transitions across the band gap opened up by intrinsic strain originating from the tube's surface curvature or ribbon's edge relaxation. The analytical study of the gapped 2D Dirac materials such as silicene and germanene, which have some similarity to the aforementioned quasi-one-dimensional systems in terms of physical description, reveals a valley- and polarization-dependent selection rules. It was also found that absorption coefficient should change in gapped materials with increasing frequency and become a half of its value for gap edge transitions when the spectrum is linear.

Our analysis of the electronic properties of flat clusters of silicene and phosphorene relates the emergence and the number of the peculiar edge states localized at zero energy, so-called zero-energy states, which are know to be of topological origin, to the cluster's structural characteristics such as shape and size. This allows to predict the presence and the number of such states avoiding complicated

topological arguments and provides a recipes for design of metallic and dielectric clusters. We show that zero-energy states are optically active and can be efficiently manipulated by external electric field. However, the edge disorder is important to take into account. We present a new fractal-based methodology to study the effects of the edge disorder which can be applied also to modeling of composite materials.

These finding should be useful in design of optoelectronic devices such as tunable emitters and detectors in a wide region of electromagnetic spectrum ranging form the mid-infrared and THz to the optical frequencies.

Contents

List of Figures

List of Tables

Acknowledgements

Firstly, I would like to sincerely thank my supervisor Prof. Mikhail Portnoi for his guidance, support, endless enthusiasm and engaging discussions of various parts of this thesis. It has been a great experience to be a part of EU FP7 ITN NOTEDEV (Grant No. FP7-607521). I am also grateful to Dr. Polina Kuzhir for opportunity to present numerous preliminary results of this research in a series of seminars organized within EU H2020 RISE project CoExAN (Grant No. H2020-644076) at the Belarusian State University.

Part I of this thesis was produced in collaborations with colleagues form the Belarusian State University (Minsk, Belarus). In particular, I would like to thank Dr. Mikhail Shuba and Prof. Konstantin Batrakov for their interest in the subject of Chapter 2 and provision of a constructive feedback. The results of Chapter 3 are an extension of the research carried out by Prof. Richard Hartmann during his PhD in Exeter and I acknowledge providing me with the results of his research.

The Part II of this thesis was produced in a close collaboration with colleagues from the Universite de Picardie Jules Vernes (Amiens, France) therefore I am indebted to Prof. Igor Lukyanchuk and Dr. Hazem Abdelsalam for introducing me into physics of silicene quantum dots and offering collaboration on optical properties of phosphorene quantum dots. I also acknowledge the help of Prof. Olivia Pulci from University of Rome Tor Vergata with the first principles calculations.

I would like to thank Dr. Charles Downing, Dr. Hai-Yao Deng and Dr. Andrey Shytov for a lot of fruitful discussions on various topics of this thesis and R. Keens for help with English.

Finally, I would like to acknowledge the support of my family.

Chapter 1

Introduction

The last two decades have witnessed great progress in the synthesis of atomically-thin two-dimensional (2D) systems such as graphene, silicene, germanene and phosphorene. In 2004 a group from the Manthcester Univesity, led by A. Geim, obtained a monolayer of carbon atoms arranged in a honeycomb lattice – graphene – in a free-standing form [2]. A continuous monolayer of silicon atoms termed silicene was grown on a substrate by several groups in 2012 [3, 4, 5], which was followed by the production of germanene [6] and monolayer of black phosphorous – phosphorene [7].

These materials are different by their physical and chemical properties. For instance, in contrast to graphene, silicene and germanene can only be grown on a metallic (Au, Ag) substrates and as such cannot be directly used for device fabrication and electrical testing. At the same time they are not stable in a free form which impedes their transfer to other substrates for further investigation. On the other hand, it was demonstrated that phosphorene can be obtained in a stable free form by liquid exfoliation or by the scotch-type peeling technique very much like graphene. However, the yield of small size flakes with a few number of phosphorene layers is high and there are an on-going efforts to produce larger size single-layer phosphorene flakes [8]. Similar to graphene, silicene and germanene have a cone-like linear dispersion for electrons, but with a small band gap of approximately 4 meV predicted to be opened by the spin-orbit interaction [9]. This contrasts with a single layer phosphorene having a significant band gap of about 2 eV [8, 10]. Despite these differences all these materials have in common that they are well-described within the single orbital tight-binding model.

The aforementioned 2D materials can be a base for a variety of nanostructures of lower dimensions. The second and third chapters of this thesis deal with quasi-one-dimentional structures based on graphene, the primary representative of the 2D materials family. Below we briefly present briefly a classification of graphene-based quasi-one-dimensional structures – carbon nanotubes (CNTs) and graphene nanoribbons (GNRs).

A single-walled carbon nanotube (CNT) is a quasi-one dimensional structure formed from rolled graphene. The whole variety of such tubes can be described by the chiral vector defining the crystallographic direction along which the rolling is performed. This vector can be written in terms of graphene lattice primitive translations $\boldsymbol{a}_1$ and $\boldsymbol{a}_2$ as [11]

$$\boldsymbol{C}_h = n\boldsymbol{a}_1 + m\boldsymbol{a}_2\,. \tag{1.1}$$

The vector $\boldsymbol{C}_h$ is usually presented by a pair of indexes (n, m) describing uniquely any particular tube. Depending on their structural symmetry single-walled carbon nanotubes can be classified as an achiral: armchair (n, n) and zigzag $(n, 0)$, – and chiral (n, m), where $n \neq m$. The three main types of tubes are presented in Fig. 1.1. A graphene nanoribbon (GNR) is a nanometer size strip of graphene. Similar to nanotube, it is quasi-one-dimensional. As one can see from Fig. 1.1 the strip can be also classified as zigzag or armchair depending on its edge geometry. It is also seen from Fig. 1.1 that any zigzag or armchair ribbon can be uniquely identified by the integer number w counting the pairs of carbon atoms in their unit cells. All zigzag graphene nanoribbons are metalic structures while only armchair ribbons with $w = 3p + 2$, where p is an integer, are metallic. Various generalizations to this basic ribbon classification are easily imagined. In particular, this classification can be extended to encompass structures somewhat similar to chiral tubes or with even more peculiar geometries [12, 13, 14, 15]. Interestingly, some of such lower-dimensional structures were obtained even earlier than their 2D host materials. For instance, carbon nanotubes were synthesised in 1991 by the arc-dischage

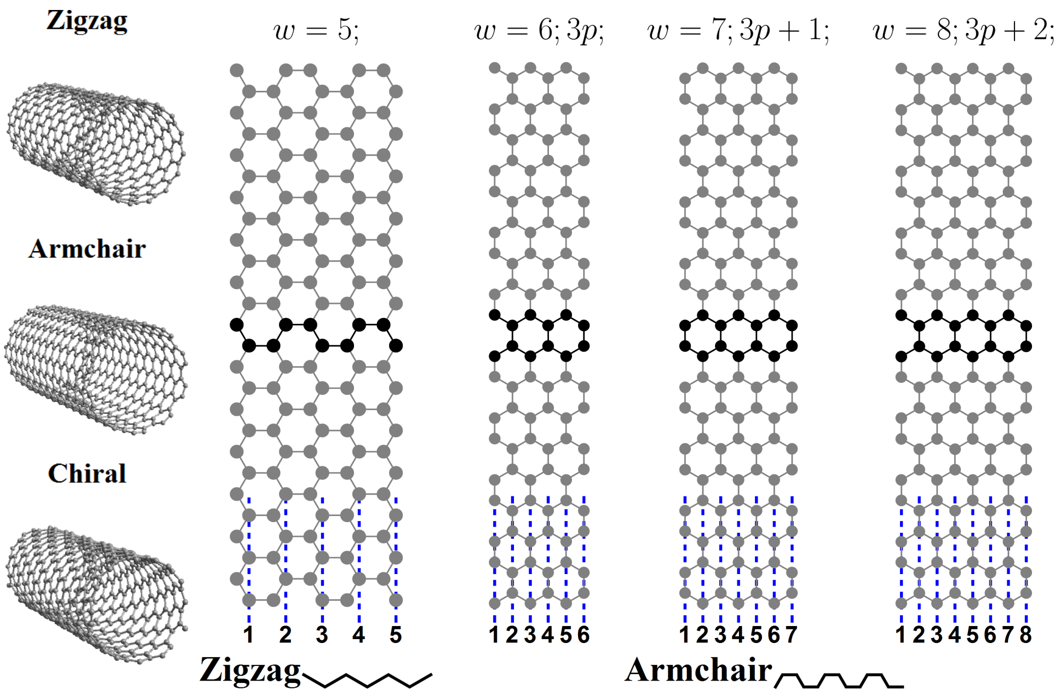

Figure 1.1: The classification of single-walled carbon nanotubes and single-layer graphene nanoribbons.

evaporation method [16] almost a decade prior to graphene mechanical exfoliation [2]. Another example is silicene nanoribbons which were grown on Ag(110) in 2010 [17, 18] two years before the realization of a continuous silicene monolayer.

The methods of synthesis of low-dimensional structures are developing fast, but those that deals with graphene seems to be the most advanced in terms of quality, yield and efficiency. For instance, recently carbon nanotubes growth at low temperatures (270°C) has been demonstrated [19]. Their chirality sorting techniques such as multicolumn gel chromotography [20] and DNA-tube recognition [21, 22] are constantly improved. At the same time, various families of graphene nanoribbons can be synthesised with atomically smooth edges [23, 24, 25, 26] in macroscopic amounts and in solutions [27] so that they can be easily transferred to any substrate. Graphene quantum dots have been also produced with well-defined shapes by decomposition of C_{60} fullerene [28]. Structures with well-defined crystallographic orientation or patterned edges can be also obtained by plasma etching [29, 30] and nanolithography [31, 32]. However, not all methods used for synthesis of graphene nanostructures are suitable for silicene or phosphorene ones. Some of them, such as self-assembling techniques [33, 23, 24, 25, 26] rely on organic molecular precursors, and, therefore, cannot be transferred to other materials in a straightforward way.

Moving to lower dimensions is motivated by advantages this could provide. Low-dimensional systems are very desirable in optical applications due to the increased density of states which facilitates lasing by reducing threshold current and therefore reducing devices' power consumption [34]. A variety of such devices is of great demand for different frequency ranges, especially for the THz frequency range [35, 36, 37, 38]. A number of schemes for generating THz radiation based on graphene have been considered [39, 40, 41, 42, 43, 44, 45]. One can single out an interesting schemes based on Cerenkov synchronization [41, 42, 43, 44]. In general, low-dimensional structures are anticipated to play an important role in future THz technology [46]. Thus, it is evident that a good understanding of electronic and optical properties of low-dimensional graphene, silicene and phosphorene structures is required.

Nowadays the most trusted theoretical tools for optical properties investigation are those based on so-called first principles calculations such as density functional theory (DFT) or Hartree-Fock methods. However, despite being treated by many as impeccable they also have their limitations. Firstly, they contain a number of assumptions making them, strictly speaking, approximate [47]. For instance, the exchange-correlation part of the energy functional in DFT is not known. The simplest approximation to this functional based on the homogeneous electron gas is referred to as local density approximation (LDA). The LDA approximation is notorious by underestimation of the band gaps [48]. At the same time, a more sophisticated approximations such as generalized gradient approximation (GGA) are not always better. Secondly, the first principle methods require solving the self-consistent problem, which is computationally costly. In the case of Hartree-Fock method this issue is also exacerbated by the necessity to deal with Slater determinants [49]. Although nowadays computers are becoming faster providing researchers more freedom in this matter, the current limit of a structure size is about

100 atoms (subjected to the complexity level of the theory and supercomputer availability).

On one hand these methods are, of course, very useful and should be used in the calculations because they are readily transferable between the structures made of different elements. On the other hand, the large number of various effects taken into account as well as a sophistication of the black-box-like commercial programs in use often hides the main physics behind the results of the numerical experiments. Therefore, one should not forget about simple tractable models such as tight-binding one. There are a lot of examples when the phenomena predicted within a simple nearest-neighbour tight-binding model later found experimental confirmation. The one cannot but mention the history of graphene. The linear electron dispersion and, therefore, relativistic nature of the electrons in this materials was predicted by Wallace in 1947 within the nearest-neighbour approximation of the single p_z-orbital tight-binding model [50]. Once graphene has become available for experimental study the measurements of the cyclotron mass confirmed this prediction with high accuracy [51]. Another unusual and important effect discovered in graphene in 2005 was the quantum Hall effect with the square root dependence on the magnetic field strength and the number of the Landau level [52]. In graphene this effect can be observed even at room temperatures [53]. The prediction of the unconventional quantum Hall effect for graphene was made within the low-energy tight-binding model [54] two years before the Nobel prize winning work of A. Geim and K. Novoselov on graphene exfoliation [2]. Graphene is an excellent material for metrological applications. It has a universal absorption almost independent of the frequency [55, 56], which can be expressed in terms of the fundamental physical constants only $\pi e^2/(\hbar c) = 2.3\%$. This surprising result can be easily restored by applying the Fermi's golden rule within the low-energy tight-binding model but was never predicted using DFT or any *ab initio* numerical techniques.

The relativistic nature of the electrons in graphene lead to observation of such phonomenon as Klein paradox [57]. In nonrelativistic quantum mechanics, tunneling probability for a particle bumping a potential barrier decays exponentially into a barrier. Thus, the probability to find the particle on the opposite side of the barrier is always smaller than the probability for the particle to reflect from the barrier. In relativistic quantum mechanics governed by the Dirac equation, the probability of tunneling can achieve unity if the height of the barrier is exceeding the rest mass of the particle. In the low-energy tight-binding model with the nearest-neighbour approximation graphene electrons are described by the effective massless Dirac equation [58, 59]. Thus, the conditions for the observation of the Kein paradox is readily met. Indeed, this the tunneling probability for normal incidence of the electrons on the barrier has been observed experimentally in graphene [60]. One more remarkable manifestation of the relativistic physics in graphene which has been also observed on experiment is “atomic collapse” [61].

Thus, it is evident that the simple tight-bidning model allows to understand, explain and even predict an essential physical phenomena, which can be observed in a real or numerical experiment. This is a great advantage of a simple tractable model along with saving the computational time and resources.

Graphene is not only an interesting system on its own but it is also a model system for other structures such as carbon nanotubes. Therefore, the tight-binding model can be also applied to single-walled carbon nanotubes. In fact, many predictions of CNT electronic and optical properties have been made within this model. One of the important things worth mentioning is the so-called Kataura plot. This plot is basically a convenient way of presenting the dependence of low-energy interband transitions on the tube diameter. This type of plot was proposed by Hiromichi Kataura in 1999 [62]. The experimental version of the Kataura plot obtained four years later showed a remarkable agreement with the numerical results obtained within the tight-binding model. Weisman et al. [63] reported the results of optical transition frequency measurements of a striking number (more than 100 semiconducting tubes of different chirality) of carbon nanotubes species in aqueous surfactant suspensions. Although the agreement was not perfect because of the many-body effects such as electron-electron interaction the pattern was reproduced in detail. A more recent experimental research collected the data of the optical transition measurements by Rayleigh spectroscopy in 206 different single-walled nanotubes with diameter range 1.3-4.7 nm [64]. Fitting this data with a limited number of parameters led to an empirical formula. The given formula interpretation is based on picture provided by the tight-binding description. This again shows an exceptional importance of the tight-binding model for carbon nanotubes. Another example related to the narrow-gap single-walled carbon nannotubes can be given. These tubes are the subjects of investigation in Chaper 3 of this thesis. In the early work based on a simple tight-binding model the curvature effects were foreseen [65]. The first study specially dedicated to this effect was performed by Kane and Mele with the effective massless Dirac equation [66]. The existence of the small curvature induced band gaps in single-walled tubes predicted by them were confirmed experimentally by scanning tunneling microscopy [67] and transport [68] measurements. The band gaps values given by Ouyang et al. [67] for CNT $(9, 0)$, $(12, 0)$ and $(15, 0)$ were different from those arising in the tight-binding model. At the same time the DFT calculations were as helpless as tight-binding ones in providing quantitative agreement with the results of the experiment. The agreement between the first principles calculations and the scanning tunneling microscopy measurements by Ouyang et al. had been reported only nine years later by Matsuda et al. [69].

The tight-binding model has also proven to be of great importance in graphene nanoribbons. Edge states in zigzag graphene nanoribbons where predicted by Fujita and co-authors in their pioneering work [70] well before graphene exfoliation. The subsequent investigation of their stability with respect to the edge disorder based on tight-binding model followed shortly [70]. Recently, the room temperature edge magnetization resulting from these states in zigzag graphene nanoribbons has been confirmed experimentally [32]. The existence of the edge states has also been confirmed by scanning tunneling spectroscopy in highest quality samples produced by self-assembling technique [71, 25]. The systematic study of graphene nanoribbons including curved ones, subjected to the external fields was carried out by group of Prof. M. F. Lin. The comprehensive review of their results can be found in Ref. [72]. The studies based on the first principles approach are somewhat less systematic and are dealing with very narrow graphene ribbons only.

The role of first principles studies increases when tight-binding model is to be transferred to structures made of elements other than carbon. The fitting of tight-binding results to those obtained form the first principles should be done if experimental data are not available. For instance, unlike carbon orbitals in graphene, in phospherene phoshorous atomic orbitals are sp^3 hybridized. Therefore phosphorene band structure is described by a mixture of s and p orbitals. However, the largest contribution for the states near the Fermi energy comes from p_z-orbitals (see Fig. 1 in Ref. [73] and a discussion in the last paragraph in Sec. 2 of Ref. [74]). As a result, the low-energy spectrum of single-layer phosphorene can be described by an effective tight-binding model accounting for only p_z-orbitals [10]. Within this tight-binding model, it is sufficient to consider only five nearest-neighbour hopping integrals for a correct description of the low-energy electronic properties of single- and double-layer phosphorene [10]. The tight-binding formalism has been widely used for the monolayer of black phosphorous [75, 75, 76], phosphorene nanoribbons [77, 78] and phosphorene quantum dots [79, 80]. This simple approach is employed in Chapter 5 of this thesis for phosphorene quantum dots. Similar to phosphorene, the fist principles calculations have been performed for low-buckled silicene [1]. The tight-binding description encompassing the main low-energy features of the silicene band structure has been provided by Liu et al. [9]. We also use this simple tractable model for our silicene quantum dots study presented in Chapter 4. Finally, we notice that the tight-binding model has been deployed successfully for group IV 2D materials [81] and GaAs monolayers [82].

The above discussion reviews the success and abundant use of a simple tight-binding description of flat-structured materials. This model can also be used for flat quasi-one- and -zero-dimensional structures. Although moving from 2D materials to such structures reduces the structure's size, it also inevitably increases the number of atoms in the structure unit cell, soaring the demand for computational power in first principles calculations. Thus, it is reasonable to use semi-empirical tight-binding model to create a roadmap for a more thorough investigation.

As we have seen, the general trends and the main insights about the optical properties of the low-dimensional structures can be obtained within semi-empirical methods such as the Huckel tight-binding model. In this approach the optical properties can be efficiently evaluated, avoiding a computationally-consuming self-consistent treatment. In many cases analytical results can be obtained, which is ideal for identifying major trends and qualitative description. It also greatly contributes to understanding of such materials and developing intuition with respect to their properties. In systems well-described by a single orbital tight-binding model, evaluation of optical matrix elements which usually requires knowledge of the actual wave functions can be reduced to the matrix elements based on the envelope wave functions and as such does not require information other than the semi-empirical tight-binging Hamiltonian [83].

In this thesis we use the advantage of the semi-empirical single orbital tight-binding model to gain a deeper understanding of optical properties of carbon nanotubes and graphene nanoribbons which have being intensively investigated by the research community for some time and to investigate the optical properties of novel structures such as silicene and phosphorene quantum dots, which we expect to be produced in the future. Our particular focus is on low-energy optical properties (mid-infrared and THz) and their tunabilily. Although some of the obtained results are related to optical and even ultraviolet range.

This thesis is organized into two parts and four chapters. Part I is devoted to carbon nanotubes and graphene nanoribbons (Chapter 2 and 3) and Part II to silicene and phosphorene nanoclusters (Chapter 4 and 5). Each chapter starts from introduction identifying problems to be solved within the outlined general framework and finishes with detailed conclusions. Future directions of the research are discussed in the concluding Chapter 6.

Chapter 2 is based on a paper published in *Physical Review B* [84] (see also Refs. [85, 86]). In this chapter an analytical tight-binding theory of the optical properties of graphene nanoribbons with zigzag edges is developed. Applying the transfer matrix technique to the nearest-neighbour tight-binding Hamiltonian, analytical expressions are derived for electron wave functions and optical transition matrix elements for incident light polarized along the structure axis. It follows from the obtained resutls that optical selection rules result from the wave function parity factor $(-1)^J$, where J is the band number. These selection rules are that ΔJ is odd for transitions between valence and conduction subbands and that ΔJ is even for transitions between only valence (conduction) subbands. Despite the fact that these selection rules are different from those in armchair carbon nanotubes, it is shown in this chapter there is a hidden correlation between absorption spectra of the two structures. This correlation implies that in some applications these two types of quasi-one-dimensional structures can be used interchangeably. The correlation originates from the fact that van Hove singularities in the tubes are centered between those in the ribbons if the ribbon width is about a half of the tube circumference. The analysis of the matrix elements dependence on the electron wave vector for narrow ribbons shows a smooth non-singular behavior at the Dirac points and the points where the bulk states meet the edge states. The aforementioned results were obtained in collaboration with Dr. Mikhail Shuba. The author of the current thesis acknowledges Dr. Shuba's ideas to investigate the doping dependent absorption spectra and optical transitions between the conduction (valence) subbands only. All the derivations were carried out by the author of this thesis who also wrote the manuscript. All the authors participated in the analysis of the obtained results and polishing the final version of the manuscript.

Chapter 3 of this thesis has not been published in any journal yet. Some result of this chapter have been presented at various conferences during the PhD course, therefore some of its ideas and preliminary results can be found in the extended conference abstracts (see Refs. [87, 88]). In this chapter, the interband dipole transitions are calculated in quasi-metallic single-walled carbon nanotubes (*zigzag* and *chiral*). The optical matrix elements in zigzag nanotubes for the incident radiation polarized parallel to the axis of the translation symmetry are compared with the corresponding matrix elements in *armchair* graphene nanoribbons. It is shown that the curvature effects for the tubes and the edge effects for the ribbons result not only in a small band gap opening, corresponding to THz frequencies, but also in a significant enhancement of the transition probability rate across the band gap. The velocity matrix element characterizing the rate of transitions has a universal value equal to the Fermi velocity of electrons in graphene. This makes these nanostructures perspective candidates for sources and detectors of THz radiation. A possible THz generation scheme is presented and discussed. It is also shown that in gapped honeycomb lattices, additionally to the strong transitions across the band gap and momentum alignment for linearly polarized light, valley dependent selection rules arise for circular polarized light.

Optical properties revealed in the Part I of this thesis pave the way to a number of possible device applications. Ideally, these devices would require frequency tunability. An obvious way to tune the properties of the structures is to apply external magnetic or electric fields. Although the application of external fields to tune electronic and optical properties of single-walled carbon nanotubes and single layer graphene nanoribbons is possible, this also impose high standards on fabrication technology. For instance, the symmetry of the carbon nanotubes does not allow using homogeneous electric fields [89], while application of the magnetic field requires either alignment of the tubes in samples or measurements on individual tubes [90]. In the case of graphene nanoribbons electronic properties can be tuned by the in-plane electric field [91, 14, 15], which relies on a technology of side gates deposition. The usage of the electric fields for flat quantum dots in the back gate geometry, when the electric field vector is perpendicular to the surface of the structure, is seen as more compatible with the current planar technology. In terms of optical properties reducing the dimension of the structures should also results in the advantage of a discrete density of states. Therefore, in Part II of this thesis I consider quasi-zero-dimensional structures – phosphorene and silicene quantum dots. Unlike single-layer graphene, silicene and phosphorene quantum dots have buckled and puckered structures allowing application of the electric field via the electrode deposited on the back side of the wafer holding the dots. It is also evident that this geometry is less sensitive to the in-plane quantum dot disorientation.

Chapter 4 of this thesis is based on a collaboration with the colleagues from the Department of Physics, Universite de Picardie Jules Vernes, Amiens, France. My secondment to France was funded by the Marie Curie Initial Training Network "NOTEDEV", EU FP7 ITN NOTEDEV (Grant No. FP7-607521). The results of this collaboration have been published in *Journal of Applied Physics* [92]. This chapter is devoted to the numerical study of optical properties of low-buckled silicene and AB-stacked bilayer graphene quantum dots subjected to an external electric field. Within the tight-binding model, the optical absorption is calculated for quantum dots of triangular and hexagonal shapes with zigzag and armchair edge terminations. It is shown that in triangular silicene nanoclusters with zigzag edges a rich and widely tunable infrared absorption peak structure originates from transitions involving zero-energy states. The edge of absorption in silicene quantum dots undergoes a red shift in the external electric field for triangular dots, whereas a blue shift takes place for hexagonal ones. In bilayer graphene quantum dots with zigzag edges the edge of absorption undergoes a blue(red) shift for triangular(hexagonal) geometry. In armchair quantum dots of silicene a blue shift of the absorption edge takes place for both dot shapes, while red shift is inherent for both shapes of bilayer graphene quantum dots.

The problem investigated in this chapter was formulated and proposed by Prof. Mikhail Portnoi and Prof. Igor Luckyanchuk to the author of this thesis and another collaborating PhD student Hazem Abdelsalam form Universite de Picardie Jules Vernes. During the secondment to the Universite de Picardie Jules Vernes the author of this thesis learned the physics of silicene and developed the programme in *Wolframe Mathematica* for optical absorption spectrum calculations. He also helped Hazem Abdelsalam to extend his code based on MATLAB *MathWorks* for treatment of optical properties of quantum dots. All the results were obtained in the two software packages independently and verified by thorough comparison and analysis. The manuscript was written in cooperation with Hazem Abdelsalam. The supervisors of Hazem Abdelsalam – M. H. Talaat in Egypt and I. A. Lukyanchuk in France – and M. E. Portnoi helped in the interpretation of the numerical results. All the authors discussed and edited the final version of the manuscript and helped responding to the referee comments. Both early stages researchers made equal contribution to this work. The order of the authors in the published paper reflects the funding conditions imposed on Hazem Abdelsalam by his fellowship. To emphasise Vasil Saroka contribution and overall coordinating role in this work he was offered the last author position, the place usually allocated for a supervisor.

Chapter 5 of this thesis is a continuation of the collaboration between the author of this thesis and Hazem Abdelsalam. This chapter is based on the manuscript submitted to the *Physical Review B*. Prof. Mikhail Portnoi and Prof. Igor Luckyanchuk helped with the result interpretation and editing the manuscript. In this chapter, we study numerically electronic and optical properties of single layer black phosphorous – phosphorene – quantum dots with various shapes, sizes, and edge types (including disordered edges) subjected to an external electric field normal to the structure plane. Compared to graphene quantum dots, in phosphorene quantum dots of similar shape and size there is a set of edge states with energies dispersed at around the Fermi level due to a redistribution of the nearest-neighbour hopping intergrals in the puckered structure of the phosphorene lattice. These states make the majority of phosphorene quantum dots metallic and enrich the phosphorene absorption gap with low-energy absorption peaks tunable by the electric field. The presence of edge states dispersed at around the Fermi level is a characteristic feature that is independent of the edge morphology and roughness. This makes phosphorene nanoclusters a good filler for electromagnetic shielding composites. Combined with the tunability in an external field this paves the way to a variety of practical applications. At the same time, we show that dielectric quantum dots which are almost insensitive to the external field perturbation can be engineered as well.

In summary, in this introductory chapter, I have presented an outline of the research field and justified the research methodology for this thesis. This chapter also overviews the main results and explains my role in the collaborative research. More detail and specific discussions are provided in the following chapters.

Part I

Optical and THz transitions in quasi-one dimensional carbon nanostructures

Chapter 2

Energy spectra and interband transitions in zigzag nanoribbons and armchair nanotubes

2.1 Introduction

Graphene nanoribbons with zigzag edges are quasi-one dimensional nanostructures based on graphene [2] that are famous for their edges states. These states were theoretically predicted for ribbons with the zigzag edge geometry by Fujita [93] and for a slightly modified zigzag geometry by Klein [94], although the history could be dated back to the pioneering works on polymers [95, 96]. Since then edge states in zigzag ribbons have been attracting much attention from the scientific community [70, 97, 98, 99, 100, 101, 102, 91, 103, 104, 105, 106, 107, 108, 109, 110, 111, 112, 113, 114, 72], because such peculiar localization of the states at the edge of the ribbon should result in the edge magnetization due to the electron-electron interaction. Although the effect was proved to be sound against an edge disorder [70], such an edge magnetization had not been experimentally confirmed until quite recently [32]. A fresh surge of interest to physics of zigzag nanoribbons is expected due to the recent synthesis of zigzag ribbons with atomically smooth edges [25] and a rapid development of the self-assembling technique [26].

The edge states in zigzag ribbons have been predicted to be important in transport [113, 114, 115], electromagnetic [116] and optical properties [99, 91, 117]. Although considerable attention has been given to zigzag ribbons' optical properties [99, 91, 117, 118, 119, 120, 121, 111, 122, 123, 124, 72], including many body effects [125, 126, 121], the effect of external fields [91, 121], curvature [72], wave function overlapping integrals [122, 123], the finite length effect [127] and the role of unit cell symmetry [128], a number of problems have not been covered yet. In particular, it is known that the optical matrix element of graphene is anisotropic at the Dirac point [129, 130] due to the topological singularity inherited from the wave functions [131, 132]. However, the fate of this singularity in the presence of the edge states, i.e. in zigzag nanoribbons, has not been investigated. This requires analysis of the optical transition matrix element dependence on the electron wave vector, in contrast to the usual analysis limited solely to the selection rules.

It was obtained numerically by Hsu and Reichl that the optical selection rules for zigzag ribbons are different from those in armchair carbon nanotubes [117]. By matching the number of atoms in the unit cell of a zigzag ribbon and an armchair tube, it was demonstrated that the optical absorption spectra of both structures are qualitatively different [117]. However, a comparison of these structures based on the matching of their boundary conditions, similar to what has been accomplished for the band structures [133] and optical matrix elements [87] of armchair graphene nanoribbons and zigzag carbon nanotubes, has not been reported yet.

The distinctive selection rules of zigzag graphene nanoribbons were noticed as early as 2000 by Lin and Shyu [99]. This remarkable and counter-intuitive result, especially when compared to the optical selection rules of carbon nanotubes [134, 129, 135, 136, 137, 138], was obtained numerically and followed by a few attempts to provide an analytical explanation [111, 120].

Within the nearest-neighbour approximation of the π-orbital tight-binding model the optical selection rules for graphene nanoribbons with zigzag edges is a result of the wave function parity factor $(-1)^J$, where J numbers conduction (valence) subbands. This factor has been obtained numerically as a connector of wave function components without explicit expressions for the wave functions being presented [111]. Concurrently, the factor $(-1)^J$, responsible for the optical selection rules, is missing in some papers providing explicit expressions for the electron wave functions (see Appendix of Ref. [109]). Although it emerged occasionally in later works dealing with the transport and magnetic properties of the ribbons [112, 114], its important role was not emphasised and its origin remains somewhat obscure. At the same time, Sasaki and co-workers obtained the optical matrix elements which, although providing the same selections rules, are very different from those in Ref. [111]. Moreover, despite being reduced to the low-energy limit around the Dirac point the matrix elements in Ref. [120] remain strikingly cumbersome.

It is the purpose of the present chapter to demonstrate a simple way of obtaining analytical expressions for optical transition matrix elements in the orthogonal tight-binding model. The essence of this work is an analytical refinement of the paper by Chung et al. [111], which provides an alternative explanation of the selection rules to that given in terms of pseudospin [120]. However, we do not simply derive analytically the results of the study [111] showing their relation to the zigzag ribbon boundary condition and secular equation, but extend the approach to the transitions between conduction (valence) subbands considered by Sasaki et al. [120]. Unlike both mentioned studies we go beyond a ‘single point’ consideration of the optical matrix elements and analyse the matrix elements as functions of the electron wave vector. The presence of possible singularities in these dependencies at $k = 2\pi/3$, corresponding to the Dirac point, and at the transition point k_t, where the edge states meet bulk states, is in the scope of our study. In this chapter we shall also investigate relations between zigzag ribbons’ and armchair nanotubes’ optical properties by matching their boundary conditions in lieu of matching the number of atoms in the unit cells as was done by Hsu and Reichl [117].

This chapter is organized as follows: in Section 2.2 we present the tight-binding Hamiltonian and solve its eigenproblem by the transfer matrix method, following the original paper by Klein [94], in this section many analogies can be drawn with the treatment of finite length zigzag carbon nanotubes [139]; optical transition matrix elements are derived within so-called gradient (effective mass) approximation and optical selection rules are obtained. The analytical results are discussed and supplemented by a numerical study in Section 2.3. Finally, the summary is provided in Section 2.4. We relegate to the appendices some technical details on ribbon wave functions and supplementary results on matching periodic and 'hard wall' boundary conditions.

2.2 Analytical tight-binding model

2.2.1 Hamiltonian eigenproblem

Let us consider a zigzag ribbon within the tight-binding model, which is the orthogonal π-orbital model taking into account only nearest neighbour hopping integrals. The atomic structure of a graphene nanoribbon with zigzag edges is presented in Fig. 2.1. A ribbon with a particular width can be addressed by index w, numbering trans-polyacetylene chains – so-called "zigzag" chains. For such a ribbon the tight-binding Hamiltonian can be constructed in the usual way by putting $k_x \to 0$, where k_x is the transverse component of the electron wave vector. We avoid the procedure described by Klein [94], since it results in a Hamiltonian for which concerns were raised by Gundra and Shukla [128]. Thus, for the ribbon with $w = 2$ it reads

$$H = \begin{pmatrix} 0 & \gamma q & 0 & 0 \\ \gamma q & 0 & \gamma & 0 \\ 0 & \gamma & 0 & \gamma q \\ 0 & 0 & \gamma q & 0 \end{pmatrix} \tag{2.1}$$

where γ is the hopping integral and $q = 2\cos(k/2)$ with $k = k_y a$ being the dimensionless electron wave vector and $a = |\boldsymbol{a}_1| = |\boldsymbol{a}_2| = 2.46$ Å being the graphene lattice constant. The Hamiltonian H has a tridiagonal structure, therefore its eigenproblem can be solved by the transfer matrix method, which is a general mathematical approach for analytical treatment of tridiagonal and tri-block diagonal matrix eigenproblems [140]. This approach was developed and widely used

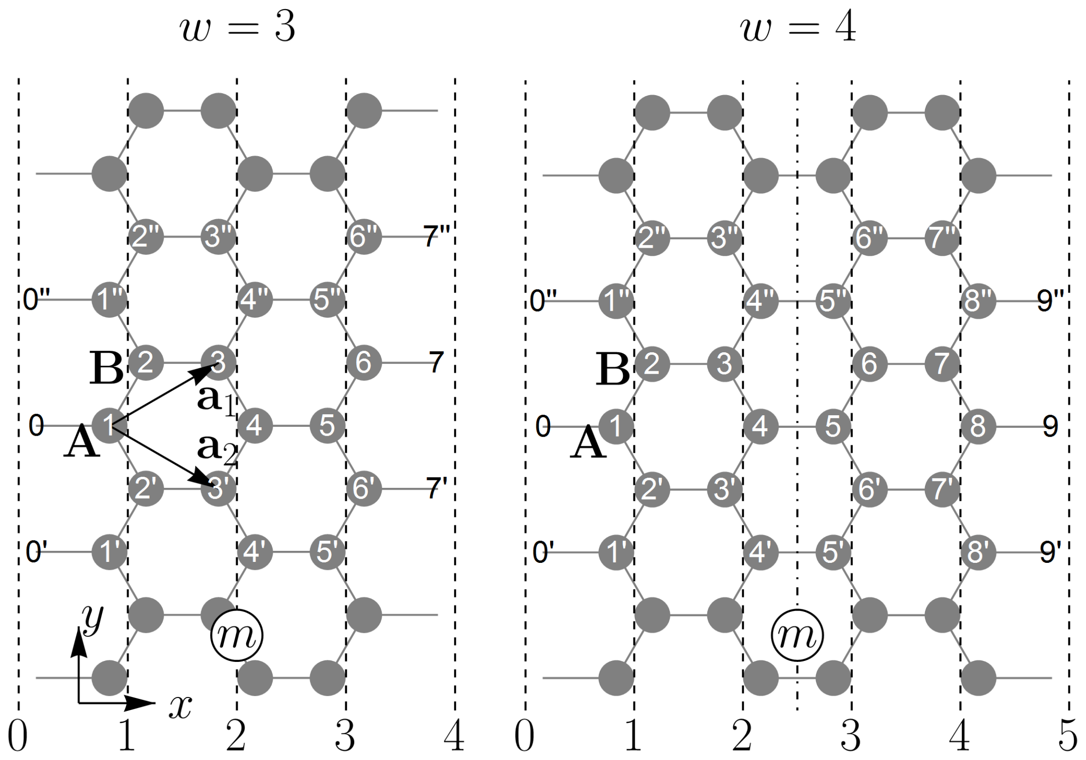

Figure 2.1: The atomic structure of zigzag ribbons consisting of $w = 3$ and 4 zigzag chains. The carbon atoms are numbered within the ribbon unit cells. The two outermost sites, where the electron wave function vanishes, are labeled by black numbers. The graphene lattice primitive translations $\boldsymbol{a}_1$ and $\boldsymbol{a}_2$ are shown along with the two nonequivalent atoms from the A and B sublattices forming the honeycomb lattice of graphene. The positions of zigzag chains, including auxiliary ones, where the electron wave function vanishes, are marked by dashed lines. m labels the dashed dotted line of the mirror symmetry for even w and the ribbon center for odd w.

for investigation of one-dimensional systems [141, 142, 143, 144]. An alternative approach may be based on continuants, which also have been used for the investigation of conjugated π-carbons such as polyenes and aromatic molecules [145, 146] and carbon nanotubes [147], (see also Refs. [148, 149, 150]).

We use H to derive the relations between the eigenvector components presented in the paper by Chung et al. [111]. In particular, we pay special attention to the origin of the $(-1)^J$ factor and its relation to the eigenstate parity. In the rest of this section we solve the eigenproblem for H.

Eigenvalues: proper energy

In this part of the section we find eigenvalues by the transfer matrix method [141, 142, 143, 144]. The eigenvalue problem for the Hamiltonian given by Eq. (2.1) can be written as follows:

$$\begin{aligned} &c_{j-1}\gamma - c_j E + c_{j+1}\gamma q = 0; && j = 2p-1 \\ &c_{j-1}\gamma q - c_j E + c_{j+1}\gamma = 0; && j = 2p\,, \end{aligned} \tag{2.2}$$

where $p = 1 \ldots w$, $w = N/2$, and N is the number of atoms in the ribbon unit cell. Each of the equations above can be rewritten in the transfer matrix form [142]:

$$\begin{aligned} &\begin{pmatrix} c_j \\ c_{j+1} \end{pmatrix} = \begin{pmatrix} 0 & 1 \\ -\frac{1}{q} & \frac{\alpha}{q} \end{pmatrix} \begin{pmatrix} c_{j-1} \\ c_j \end{pmatrix}; && j = 2p-1\,, \\ &\begin{pmatrix} c_j \\ c_{j+1} \end{pmatrix} = \begin{pmatrix} 0 & 1 \\ -q & \alpha \end{pmatrix} \begin{pmatrix} c_{j-1} \\ c_j \end{pmatrix}; && j = 2p\,. \end{aligned} \tag{2.3}$$

where $\alpha = E/\gamma$. Introducing

$$T_1 = \begin{pmatrix} 0 & 1 \\ -\frac{1}{q} & \frac{\alpha}{q} \end{pmatrix}; \qquad T_2 = \begin{pmatrix} 0 & 1 \\ -q & \alpha \end{pmatrix} \tag{2.4}$$

and substituting j into (2.3) yield

$$\begin{pmatrix} c_{2p-1} \\ c_{2p} \end{pmatrix} = T_1 \begin{pmatrix} c_{2p-2} \\ c_{2p-1} \end{pmatrix}, \qquad (2.5)$$

$$\begin{pmatrix} c_{2p} \\ c_{2p+1} \end{pmatrix} = T_2 \begin{pmatrix} c_{2p-1} \\ c_{2p} \end{pmatrix},$$

whence the following recursive relation can be readily noticed:

$$\begin{pmatrix} c_{2p} \\ c_{2p+1} \end{pmatrix} = T_2 T_1 \begin{pmatrix} c_{2p-2} \\ c_{2p-1} \end{pmatrix}, \qquad (2.6)$$

and the following transfer matrix equation can be obtained:

$$C_{2p+1} = \begin{pmatrix} c_{2p} \\ c_{2p+1} \end{pmatrix} = T^p C_1 \,. \qquad (2.7)$$

Thus, the transfer matrix in question is

$$T = T_2\, T_1 = \begin{pmatrix} -\dfrac{1}{q} & \dfrac{\alpha}{q} \\ -\dfrac{\alpha}{q} & \dfrac{\alpha^2 - q^2}{q} \end{pmatrix}. \qquad (2.8)$$

The characteristic equation for finding the eigenvalues of T, $\det(T - \lambda I) = 0$, is a quadratic one:

$$\lambda^2 + \left(\frac{1}{q} + q - \frac{\alpha^2}{q}\right)\lambda + 1 = 0\,. \qquad (2.9)$$

This equation has the following solution:

$$\lambda_{1,2} = A \pm \sqrt{A^2 - 1}\,, \qquad (2.10)$$

where

$$A = \frac{\alpha^2 - q^2 - 1}{2q} = -\cos\theta\,. \qquad (2.11)$$

A new variable θ has been introduced above to reduce the eigenvalues $\lambda_{1,2}$ to the complex exponent form, which is favourable for further calculations:

$$\lambda_{1,2} = -e^{\mp i\theta}\,, \qquad (2.12)$$

where the upper (lower) sign is used for λ_1 (λ_2). We must note that another choice of variable θ, i.e. $A = \cos\theta$, is also possible, but it results in the inverse numbering of the proper energy branches. The minus sign is a better choice because it allows one to avoid a change of the lowest (highest) conduction (valence) subband index when the ribbon width increases.

Equation (2.11) allows one to express the proper energy in terms of θ and q:

$$\alpha = \frac{E}{\gamma} = \pm\sqrt{q^2 - 2q\cos\theta + 1}\,. \tag{2.13}$$

Taking into account that $q = 2\cos(k/2)$, for the proper energy we obtain

$$E = \pm\gamma\sqrt{4\cos^2\frac{k}{2} - 4\cos\frac{k}{2}\cos\theta + 1}\,, \tag{2.14}$$

where θ is to be found from the secular equation for the fixed ends boundary condition as in the case of a finite atomic chain [142, 143, 144]. The physical interpretation of the parameter θ is to be given later. We note that Eq. (2.14) has similar form not only to the graphene energy band structure [50, 65, 11] but also to the eigenenergies of the finite length zigzag carbon nanotubes [139] (cf. with Eq. 32 therein).

Secular equation

For the fixed end boundary condition, which, in the context of the electronic properties being considered, is better referred to as the 'hard wall' boundary condition, the general form of the secular equation is $(T^w)_{22} = 0$ [144]. This equation can be obtained by imposing the constraint $c_0 = c_{N+1} = 0$ on Eq. (2.7), where $p = w$, which physically means the vanishing of the tight-binding electron wave functions on sites 0 and $N+1$, or equivalently on zigzag chains 0 and $w+1$ as illustrated in Fig. 2.1. Hence, for the secular equation the w-th power of the transfer matrix T is needed. The simplest way of calculating T^w is $T^w = S\Lambda^w S^{-1}$, where Λ is the diagonal form of T and S is the matrix making the transformation to a new basis in which T is diagonal. The eigenvalues of T are given by Eq. (2.12), therefore Λ can be easily written down. Concurrently, the S matrix can be constructed from eigenvectors of T written in columns. By setting the first components of the vectors to be equal to unity, one can reduce them to

$$V_1 = \begin{pmatrix} 1 \\ \xi_1 \end{pmatrix}; \qquad V_2 = \begin{pmatrix} 1 \\ \xi_2 \end{pmatrix}, \tag{2.15}$$

where the following notation is used:

$$\xi_{1,2} = \frac{1 + q\lambda_{1,2}}{\alpha}\,. \tag{2.16}$$

Then the matrix S and its inverse matrix S^{-1} can be written as follows:

$$S = \begin{pmatrix} 1 & 1 \\ \xi_1 & \xi_2 \end{pmatrix}; \qquad S^{-1} = \frac{1}{\xi_2 - \xi_1} \begin{pmatrix} \xi_2 & -1 \\ -\xi_1 & 1 \end{pmatrix}. \tag{2.17}$$

Expressions (2.17) are of the same form as in the atomic ring problem [143]. Using (2.17), the T^w calculation yields

$$T^w = \frac{1}{\xi_2 - \xi_1} \begin{pmatrix} \xi_2\lambda_1^w - \xi_1\lambda_2^w & \lambda_2^w - \lambda_1^w \\ \xi_1\xi_2\left(\lambda_1^w - \lambda_2^w\right) & \xi_2\lambda_2^w - \xi_1\lambda_1^w \end{pmatrix}. \tag{2.18}$$

Now with the aid of (2.16) and (2.12) from (2.18) we can find the explicit form of the secular equation for θ:

$$\sin w\theta - 2\cos\frac{k}{2}\,\sin\left[(w+1)\theta\right] = 0\,. \tag{2.19}$$

The equation above is very much like that analysed by Klein [94] for so-called "bearded" zigzag ribbons, therefore the same basic analysis can be carried out.

As can be seen from Fig. 2.2, all non-equivalent solutions of Eq. (2.19) reside in the interval $\theta \in (0, \pi)$. When the slope of $q\sin[(w+1)\theta]$ at $\theta = 0$ is greater than that of $\sin w\theta$, i.e. $(q\sin[(w+1)\theta])'_{\theta=0} > (\sin w\theta)'_{\theta=0} \Rightarrow 2\cos(k/2) > w/(w+1)$, there are w different solutions in the interval, which give $2w$ branches of the proper energy (2.14). This is indicated in Fig. 2.2 (a) and (b). However, as seen from Fig. 2.2 (c) and (d), when $2\cos(k/2) \leq w/(w+1)$, one solution is missing and Eq. (2.14) defines only $2w - 2$ branches. The missing solution can be restored by analytical continuation $\theta = i\beta$, where β is a parameter to be found. In this case the secular equation (2.19) and the proper energy (2.14) must be modified accordingly by changing trigonometric functions to hyperbolic ones.

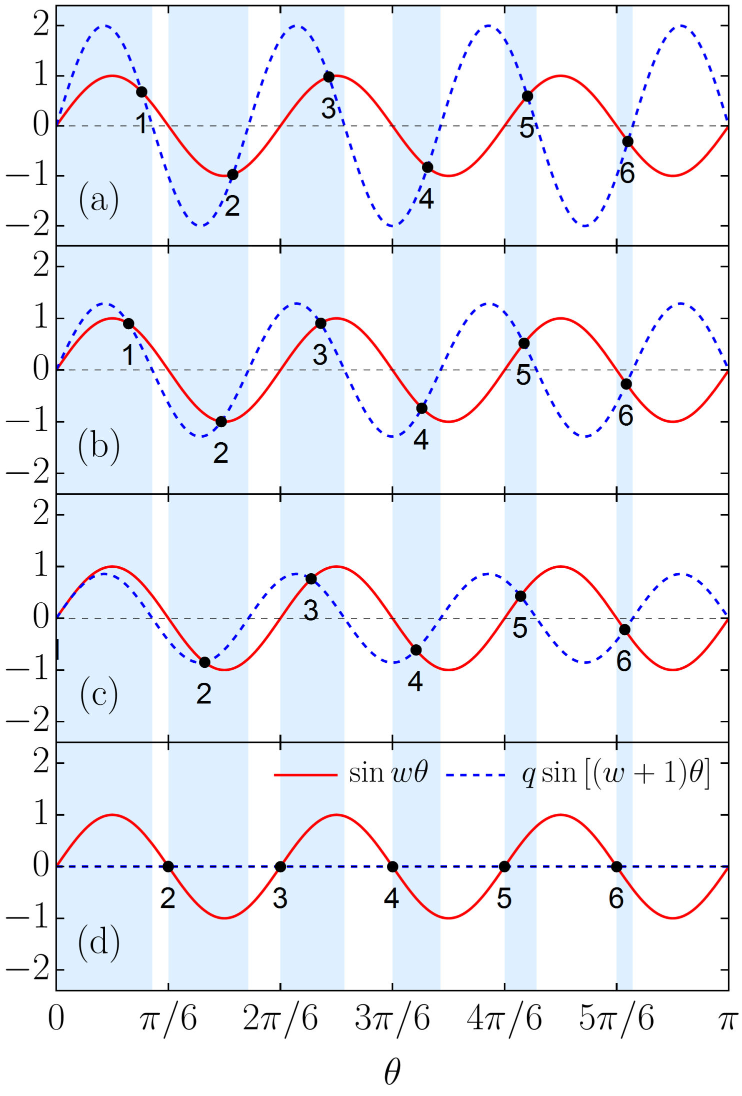

Figure 2.2: Solutions of the secular equation (2.19) for zigzag graphene nanoribbon with $w = 6$ and the following values of the parameter $q = 2\cos(k/2)$: (a) 0; (b) $w/(w+1)$; (c) $3w/2(w+1)$; (d) 2. The light blue shading signifies the θ-intervals to which the secular equation solutions are confined for q's ranging from 0 to ∞.

The above introduced parameter θ (β) can be interpreted as a transverse component of the electron wave vector and the secular equation (2.19) can be referred to as its quantization condition.

Eigenvectors: wave functions

Let us now find eigenvectors of the Hamiltonian given by Eq. (2.1). To obtain the eigenvector components we choose the initial vector $C_1 = (c_0, c_1)$ as a linear combination of the transfer matrix eigenvectors that satisfies the 'hard wall' boundary condition $c_0 = 0 : \; C_1 = 1/(2i)(V_1 - V_2)$. It is to be mentioned here that the opposite end boundary condition, $c_{N+1} = 0$, is ensured by Eq. (2.19). The chosen C_1 yields

$$\begin{aligned} C_{2p+1} = T^p C_1 &= \frac{1}{2i}\left(\lambda_1^p V_1 - \lambda_2^p V_2\right) \\ &= \frac{1}{2i}\begin{pmatrix} \lambda_1^p - \lambda_2^p \\ \lambda_1^p \xi_1 - \lambda_2^p \xi_2 \end{pmatrix} \end{aligned} \tag{2.20}$$

or equivalently

$$\begin{aligned} c_{2p} &= \frac{1}{2i}\left(\lambda_1^p - \lambda_2^p\right); \qquad\qquad p = 1 \ldots w \\ c_{2p+1} &= \frac{1}{2i}\left(\lambda_1^p \xi_1 - \lambda_2^p \xi_2\right); \end{aligned} \tag{2.21}$$

Substituting (2.12) and (2.16) into (2.21) and keeping in mind the definition of α, one readily obtains,

$$c_{2p} = (-1)^{p+1} \sin p\theta; \qquad\qquad p = 1 \ldots w \tag{2.22}$$

$$c_{2p+1} = \frac{(-1)^{p+1}\gamma}{E}\left\{\sin p\theta - 2\cos\frac{k}{2}\,\sin\left[(p+1)\theta\right]\right\}. \tag{2.23}$$

It is worth pointing out that for the starting $p = 1$ from the equations above one gets components c_2 and c_3. Although it may seem strange because of the missing c_1, this is how it should be for c_1 has already been specified by the proper choice of the initial vector C_1.

Equation (2.23) can be further simplified (see Appendix A) so that for the eigenvector components one has

$$c_{2p}^{(j)} = (-1)^{p+1} \sin p\theta_j; \qquad\qquad p = 1 \ldots w \tag{2.24}$$

$$c_{2p+1}^{(j)} = \pm(-1)^{p+1}(-1)^{j-1} \sin\left[(p-w)\theta_j\right]. \tag{2.25}$$

where we have introduced the index j to number various values of θ, which are solutions of Eq. (2.19). As one may have noticed the above expressions still have one drawback: $p = 1$ defines components c_2 and c_3, while it would be much more convenient if $p = 1$ would instead specify c_1 and c_2. To obtain desired dependence of the eigenvector components on the variable index one needs to re-define in Eq. (2.25) the index $p \to n - 1$:

$$\begin{aligned} c_{2n-1}^{(j)} &= \pm(-1)^n(-1)^j \sin\left[(w+1-n)\theta_j\right] \, ; && n = 1\dots w \\ c_{2p}^{(j)} &= (-1)^{p+1} \sin p\theta_j \, . && p = 1\dots w \end{aligned}$$

and then put $n \to p$. The latter is permissible since n is a dummy index that can be denoted by any letter. Note that due to the change of the terms order in the sine function one (-1) factor in the coefficient $c_{2p+1}^{(j)}$ above cancels therefore $j - 1$ in the exponent has been replaced by j. Thus, for the Hamiltonian (2.1) we end up with the following eigenvectors:

$$\begin{aligned} c_{2p-1}^{(j)} &= \mp(-1)^p(-1)^j \sin\left[(w+1-p)\theta_j\right] \, ; \\ c_{2p}^{(j)} &= (-1)^p \sin p\theta_j \, , \qquad p = 1\dots w \, , \end{aligned} \tag{2.26}$$

where we have got rid of (-1) in $c_{2p}^{(j)}$. Since the whole eigenvector $\left|c^{(j)}\right\rangle = \left(c_1^{(j)}, c_2^{(j)}, \dots, c_N^{(j)}\right)$ can be multiplied by any number, one can choose this number to be (-1). Having multiplied $\left|c^{(j)}\right\rangle$ by (-1), one has to change ± to ∓ in the coefficient $c_{2p+1}^{(j)}$, therefore in Eq. (2.26) the upper "−" stands now for the conduction band, while the lower "+" for the valence band. The $(-1)^p$ factor, however, cannot be eliminated in a similar way because it determines the signs of various components differently. Nevertheless, this factor is of no significance, too, for it can be eliminated by a unitary transform U, which is a diagonal matrix with the main diagonal defined as

$$\{u_{2p-1,2p-1}, u_{2p,2p}\} = \{(-1)^p, (-1)^p\}|_{p=1\dots w} \, . \tag{2.27}$$

For $w = 2$ it reads

$$U = \begin{pmatrix} -1 & 0 & 0 & 0 \\ 0 & -1 & 0 & 0 \\ 0 & 0 & 1 & 0 \\ 0 & 0 & 0 & 1 \end{pmatrix} . \tag{2.28}$$

As follows from (2.27), U is both a unitary and an involutory matrix. It can be straightforwardly checked that applying the unitary transform (2.27) to the eigenvector of H given by Eq. (2.1), i.e. $\left|\widetilde{c}^{(j)}\right\rangle = U\left|c^{(j)}\right\rangle$, we obtain eigenvectors of the Hamiltonian $\widetilde{H} = UHU^{\dagger}$. For $w = 2$ the explicit form of the new Hamiltonian is

$$\widetilde{H} = \begin{pmatrix} 0 & \gamma q & 0 & 0 \\ \gamma q & 0 & -\gamma & 0 \\ 0 & -\gamma & 0 & \gamma q \\ 0 & 0 & \gamma q & 0 \end{pmatrix} . \tag{2.29}$$

The general form of the eigenvectors of $\widetilde{H}$ is the same as (2.26) but without $(-1)^p$ factor:

$$\begin{aligned} \widetilde{c}^{(j)}_{2p-1} &= \mp(-1)^j \sin\left[(w+1-p)\theta_j\right] \; ; \\ \widetilde{c}^{(j)}_{2p} &= \sin p\theta_j \, , \qquad p = 1 \ldots w \, . \end{aligned} \tag{2.30}$$

Equations (2.30) and (2.26) present components of non-normalized eigenvectors $\left|c^{(j)}\right\rangle$. Normalization constant N_j for these vectors can be found from the normalization condition $N_j^2 \left\langle c^{(j)} \,\middle|\, c^{(j)}\right\rangle = N_j^2 \sum_{p=1}^{w} c^{(j)*}_{2p-1} c^{(j)}_{2p-1} + c^{(j)*}_{2p} c^{(j)}_{2p} = 1$, which yields

$$N_j = \frac{1}{\sqrt{w - \cos\left[(w+1)\theta_j\right] \dfrac{\sin w\theta_j}{\sin\theta_j}}} . \tag{2.31}$$

We do not use "$\sim$" two distinguish the two types of eigenvectors mentioned above because, by definition, unitary transform preserves the dot product, therefore the normalization constant is the same in both cases.

As in the case of the secular equation, eigenvectors and normalization constants for the missing solution θ are obtained by the substitution $\theta \to i\beta$, which results in wave functions being exponentially decaying from the ribbon edges to its interior. These wave functions describe the so-called edge states [94, 93, 70]. In contrast to them the wave functions given by normal solutions θ_j extend over the whole ribbon width, therefore they describe the so-called extended or bulk states. It can be shown that normalized eigenvectors' components for extended and edge states seamlessly match in the transition point k_t defined by $2\cos(k/2) = w/(w+1)$ (see Appendix B).

The matching of the bulk and edge state wave functions is shown in Figure 2.3, where the wave functions of the zigzag ribbon with $w = 15$ are plotted as functions of the atomic site positions $x_{2p-1} = (\sqrt{3}a/2)(p-1)$ and $x_{2p} = (a/2\sqrt{3}) + x_{2p-1}$ normalized by the ribbon width $W = x_{2w}$. Figure 2.3 presents wave functions for several energy branches $J(s)$, where J is the energy branch number and $s = c$ or v refers to the conduction or valence branch, respectively. As one can see, a bulk state wave function $|1(v)\rangle$, Fig. 2.3 (a), transforms into a wave function $|1(v)\rangle$ predominantly concentrated at the ribbon edges and decaying towards the ribbon center, Fig. 2.3 (c), by becoming a linear function of x_i/W at $k = k_t$ as shown in Fig. 2.3 (b). One can also see that the parity factor can be associated with the mirror or inversion symmetry of the electron wave function. For conduction subbands if the parity factor $(-1)^J$ is positive then the wave function is symmetric with respect to the inversion center denoted by the large black point as seen for $|2(c)\rangle$ and $|4(c)\rangle$ in Fig. 2.3 (a) and (c). This means the wave function is odd. However, if $(-1)^J$ is negative then the wave function is even, i.e. it is symmetric with respect to the reflection in the the dashed dotted line signifying the ribbon center. This happens for $|3(c)\rangle$ in Fig. 2.3 (b). For the valence subbands the behaviour is opposite: if $(-1)^J$ is negative then the state wave function is odd, as can be seen from Fig. 2.3 for the subband $1(v)$, but it is even for positive parity factor $(-1)^J$. Such behaviour is in agreement with the general properties of motion in one dimension [151]. The parity factor attributed to the mirror symmetry with respect to the line bisecting the ribbon longitudinally (see Fig. 2.1) has been discussed in the literature [95, 117, 122, 123]. In this view, it should be noted that the unit cells of ribbons with odd w do not have such a reflection symmetry (see Fig. 2.1 for $w = 3$), nevertheless as we see from Fig. 2.3 for such ribbons the wave functions can still be classified as even or odd in aforementioned sense. This suggests that the symmetry argument developed in Ref. [128] as a criterion for the usage of the gradient approximation, which is to be discussed in the next section, is

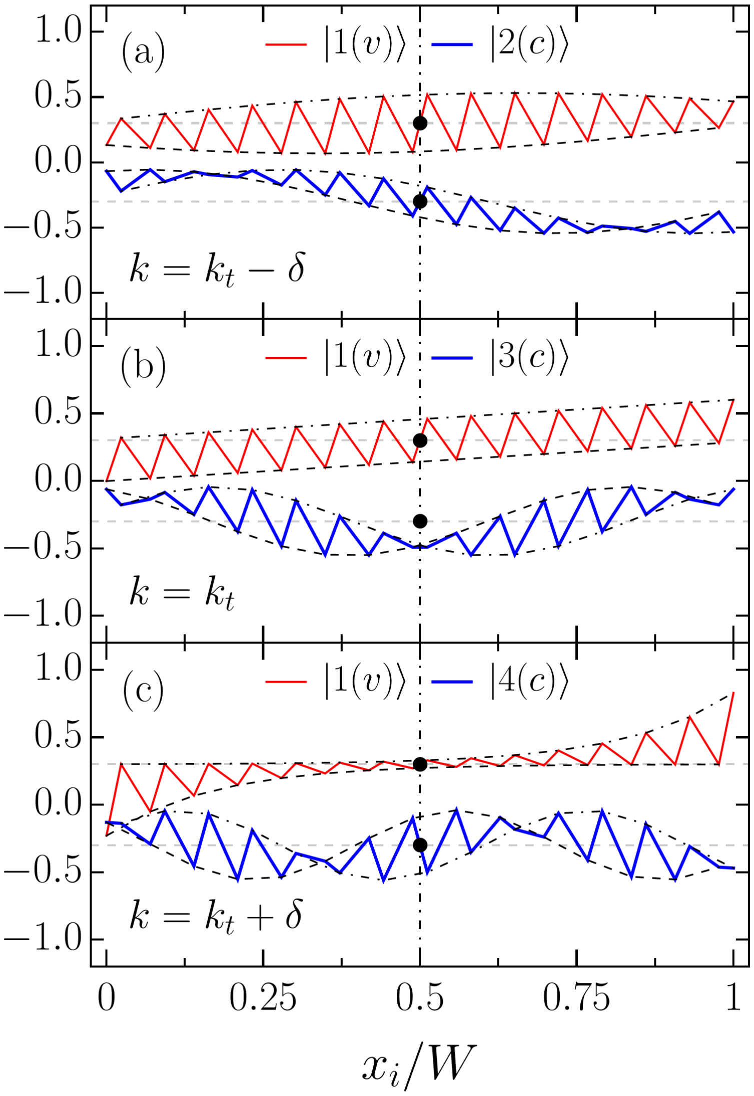

Figure 2.3: The bulk-edge transformation and parity of a zigzag nanoribbon wave function. The normalized wave functions $|J(s)\rangle$ of the zigzag nanoribbon with $w = 15$ for various bands $J(s)$ and the Brillouin zone points $k = k_t + \delta$: (a) $\delta = -0.3$; (b) $\delta = 0$ (c) $\delta = 0.3$. The solid lines are used for eye guidance, while the dashed and dashed-dotted curves represent the envelopes of the $2p-1$ (A) and $2p$ (B) sites. The horizontal axis is a normalized transverse coordinate x_i/W, with W being the ribbon width. The plots are shifted vertically by ± 0.3 for clarity. The dashed dotted vertical line and thick black points denote the line of the mirror and centers of the inversion symmetry, respectively.

not complete, since in that form it applies only to ribbons with even w. Finally, we notice that the state wave functions can be classified by a number of twists of the envelope functions presented in Fig. 2.3 by dashed and dashed dotted curves. The number of such twists (nodes) is equal to $J(c)$ and $J(v)-1$ for the conduction and valence subbands $J(s)$, respectively. This behaviour is similar to what is expected from the oscillation theorem [151].

2.2.2 Optical transition matrix elements

In this section we study the optical properties of graphene nanoribbons with zigzag edges. Optical transition matrix elements are worked out in the gradient (effective mass) approximation [152, 153, 154, 155] and optical selection rules are obtained. However, before moving to the matrix elements of the ribbons we shall introduce details of optical absorption spectra calculations where these matrix elements are to be used.

Within the first order time-dependent perturbation theory the transition probability rate between two states, say $|\Psi_f\rangle$ and $|\Psi_i\rangle$ having energy E_f and E_i, respectively, is given by the golden rule [156]:

$$A_{i\to f} = \frac{2\pi}{\hbar} \left| \left\langle \Psi_f \left| \widehat{H}_{\text{int}}(t) \right| \Psi_i \right\rangle \right|^2 \delta(E_f - E_i - \hbar\omega) \tag{2.32}$$

where $\delta(\dots)$ is the Dirac delta-function, and $\widehat{H}_{\text{int}}(t)$ is a time-dependent interaction Hamiltonian coupling a system in question to that causing a perturbation, which is periodic in time with frequency ω. Considering an incident plane electromagnetic wave as a perturbation, one can show in the dipole approximation, $e^{i\boldsymbol{k}\cdot\boldsymbol{r}} \approx 1$, that

$$\left\langle \Psi_f \left| \widehat{H}_{\text{int}}(t) \right| \Psi_i \right\rangle \sim \frac{E_0}{\omega} \left\langle \Psi_f \left| \widehat{\boldsymbol{v}} \cdot \boldsymbol{e}_p \right| \Psi_i \right\rangle \equiv \frac{E_0}{\omega} M_{f,i} \tag{2.33}$$

where $\widehat{\boldsymbol{v}}$ is the velocity operator, E_0 is the electric field strength amplitude and $\boldsymbol{e}_p$ is the vector of electromagnetic wave polarization. Thus, optical transition matrix elements can be reduced to the velocity operator matrix elements (VMEs).

The total number of transitions per unit time in solids irradiated by electromagnetic wave at zero temperature is a sum of $A_{i\to f}$ over all initial (occupied) states in the valence band and final (unoccupied) states in the conduction band. To account for losses such as impurity and electron-phonon scattering, the delta-function in Eq. (2.32) is replaced by a Lorentzian. The difference in occupation numbers of the initial and final states due to the finite temperature is introduced by the Fermi-Dirac distribution. Then, for the absorption coefficient due to the interband transitions one has

$$A(\omega) \sim \sum_{n,m,k,s,s'} \mathrm{Im}\left[\frac{f(E_{m,s}(k)) - f(E_{n,s'}(k))}{E_{n,s'}(k) - E_{m,s}(k) - \omega - i\Gamma}\right] \frac{\left|M_{n(s),m(s')}(k)\right|^2}{\omega}\,, \tag{2.34}$$

where $E_{m,s}(k)$ is the dispersion of the electron in the m-th conduction ($s = c$) or valence ($s = v$) subband, $f(E_{m,s}(k))$ is the Fermi-Dirac distribution function, $M_{n(s),m(s')}(k)$ is the optical transition matrix element being a function of the electron wave vector, Γ is the phenomenological broadening parameter ($0.004\,\gamma$) [99]. Note that for non-zero temperature summation over initial states should also include states in the conduction band, therefore indices s, s' have been introduced above. The frequency of an incident wave, ω, as well as the electron energy, is measured in units of the hoping integral γ.

Similar to Ref. [111] we follow the prescription of the gradient approximation [152, 154] to obtain the velocity operator right from the system Hamiltonian:

$$\widehat{\boldsymbol{v}} = \frac{i}{\hbar}\left[\widehat{H}, \widehat{r}\right] = \frac{1}{\hbar}\frac{\partial \widehat{H}}{\partial \boldsymbol{k}} \tag{2.35}$$

whence for a one dimensional case

$$v = \frac{1}{\hbar}\frac{\partial H}{\partial k}\,, \tag{2.36}$$

with H being the Hamiltonian of the unperturbed system. Note that the derivative $\partial H/\partial k$ is different from $\partial H/\partial \boldsymbol{A}$ mentioned in Ref. [120], where $\boldsymbol{A}$ is the vector potential. The former has a clear relation to the minimal coupling $\boldsymbol{k} \to \boldsymbol{k} + (e/\hbar)\boldsymbol{A}$ via the expansion $H(\boldsymbol{k} + (e/\hbar)\boldsymbol{A}) = H(\boldsymbol{k}) + (e/\hbar)\nabla_{\boldsymbol{k}} H \cdot \boldsymbol{A} + \ldots$, where higher order terms can be neglected for small $\boldsymbol{A}$. Such an approach is equivalent to the effective mass treatment since the commutator $[\ldots]$ in Eq. (2.35) implies that the crystal momentum $\boldsymbol{k}$ is an operator:

$$\boldsymbol{k} = \frac{1}{i}\frac{\partial}{\partial x}\boldsymbol{i} + \frac{1}{i}\frac{\partial}{\partial y}\boldsymbol{j} \tag{2.37}$$

which commutes with the position operator in the same way as real momentum $\boldsymbol{p}$, i.e. $[x, k_x] = i$. Note, however, that there is no formal restriction to low-energies around the Dirac point, $k = 2\pi/3$, as in the $\boldsymbol{k} \cdot \boldsymbol{p}$ theory with the effective mass approximation for graphene [59, 157], carbon nanotubes [158, 159] or graphene nanoribbons [101, 160].

In what follows we proceed with the calculation and analysis of the velocity operator matrix elements (VMEs) in the gradient (effective mass) approximation. Introducing the following vector:

$$\left|\zeta^{(m)}\right\rangle = \frac{a}{\hbar}\frac{\partial H(k)}{\partial k}\left|c^{(m)}\right\rangle , \tag{2.38}$$

the VME is evaluated as

$$\begin{aligned} M_{n(c),m(v)} &= \left\langle c_c^{(n)} \middle| \zeta_v^{(m)} \right\rangle \\ &= \sum_{p=1}^{w} \underset{c}{c_{2p-1}^{(n)*}} \underset{v}{\zeta_{2p-1}^{(m)}} + \underset{c}{c_{2p}^{(n)*}} \underset{v}{\zeta_{2p}^{(m)}} , \end{aligned} \tag{2.39}$$

where indices "c" and "v" denote the conduction and valence band, respectively, and the eigenvectors $\left|c^{(n,m)}\right\rangle$ are meant to be normalized. In equation (2.38), the graphene lattice constant a emerged because, in contrast to the general expression (2.36), the electron wave vector k is now treated again as a dimensionless quantity.

Let us calculate VMEs for the Hamiltonian $\widetilde{H}$ of the form presented by Eq. (2.29). Similar calculations for H results in the same final expression. Due to the nature of unitary transforms it is not essential which of the Hamiltonians and corresponding eigenvectors one uses. The components of vectors $\left|\widetilde{\zeta}^{(j)}\right\rangle$ are

$$\begin{aligned} \widetilde{\zeta}_{2p-1}^{(j)} &= -\frac{\gamma a}{\hbar}\sin(\frac{k}{2})\sin p\theta_j\,; \qquad p = 1\ldots w \\ \widetilde{\zeta}_{2p}^{(j)} &= \pm\frac{\gamma a}{\hbar}\sin(\frac{k}{2})(-1)^j \sin\left[(w+1-p)\theta_j\right] , \end{aligned} \tag{2.40}$$

with upper "+" (lower "−") being used for conduction (valence) subbands. Substituting Eqs. (2.30) and (2.40) into (2.39), one obtains

$$M_{n(c),m(v)} = \frac{\gamma a}{\hbar}\sin(\frac{k}{2})N_n N_m\left[(-1)^n - (-1)^m\right]S_{n,m} , \tag{2.41}$$

where $S_{n,m}$ is a sum. A similar form of the matrix element was obtained in Ref. [111] but explicit expressions for the sum $S_{n,m}$ and normalization constants $N_n(N_m)$ were not provided and potential singularities in VME due to N_j and $S_{n,m}$ dependence on k were not analysed. Such an analysis has not been carried out elsewhere including Ref. [120].

It is known that the topological singularity in the graphene wave functions [131, 132] leads to anisotropic optical matrix element and absorption in the vicinity of the Dirac point [129, 130]. This anisotropy is eliminated in the matrix element of carbon nanotubes [129, 135], but the matrix element can exhibit singular behavior at the Dirac point of the tube's Brillouin zone if a perturbation such as strain, curvature [87] or external magnetic field [161, 162, 163] is applied. The sharp dependence of the zigzag ribbon VME on the electron wave vector around $k = \pm 2\pi/3$ could be triggered by the presence of the edge states. This possibility, however, has not been analysed yet. The VME behaviour at the transition point k_t has not been investigated either. Being of practical interest [87] this requires a thorough analysis of possible singularities in the VME dependence on k. The $S_{n,m}$ sum is given by

$$\begin{aligned} S_{n,m} &= \sum_{p=1}^{w} \sin\left[(w+1-p)\theta_n\right] \sin p\theta_m\,; \\ &= \frac{\sin\theta_m \sin\left[(w+1)\theta_n\right] - \sin\left[(w+1)\theta_m\right]\sin\theta_n}{2(\cos\theta_n - \cos\theta_m)}\,. \end{aligned} \tag{2.42}$$

In equation (2.41) normalization constants have been added since the vectors given by Eq. (2.30) and used for obtaining Eq. (2.40) are not normalized. It is important to allow for normalization constants in the VMEs because otherwise due to their θ_j and therefore k dependency the VME curve's behaviour in the vicinity of the transition point k_t is incorrect. It is also worth noting that for $\theta_n = \theta_m$, or equivalently for $S_{n,n}$, there is an indeterminacy of $\frac{0}{0}$-type in the summation result of Eq. (2.42). This indeterminacy can be easily resolved by L'Hospital's rule, which yields

$$S_{n,n} = \frac{(w+2)\sin w\theta_n - w\sin\left[(w+2)\theta_n\right]}{4\sin\theta_n}\,. \tag{2.43}$$

In a similar fashion one can check that for $\theta_n \to 0$, $S_{n,n} \to 0$. Note, however, that if $\theta_n \to 0$, then the normalization constant N_n given by Eq. (2.31) becomes infinitely large, thereby introducing indeterminacy into the VME. For transitions between the valence and conduction subbands this indeterminacy is not essential for it is multiplied by an exact zero, originating from the square brackets in Eq. (2.41), which ensures a zero final result.

As can be seen from Eq. (2.41), $M_{n(c),n(v)}$ is zero, whereas

$$M_{n(c),n+1(v)} \sim N_n N_m S_{n,m} \sin(k/2)\,.$$

Thus, optical selection rules are: if $\Delta J = n - m$ is an even integer, then transitions are forbidden, whereas if $\Delta J = n - m$ is an odd integer, then transitions are allowed. The influence of the factor $S_{n,m}$ together with the normalization constants N_n and N_m on the transition probability, omitted in Ref. [111], will be discussed in detail in Sec. 2.3. In the remainder of this section, we consider transitions between only conduction (valence) subbands which are considered in Ref. [120] but are beyond the scope of Ref. [111].

If the temperature is not zero, then there is a non-zero probability to find an electron in the conduction subband states. Therefore, an incident photon can be absorbed due to transitions between conduction subbands. The same is true for valence subbands, which are not fully occupied. That is why, as has been pointed out above, the summation in Eq. (2.34) is to be carried out over transitions between conduction (valence) subbands too. Thus, for the absorption coefficient calculation one also needs VMEs for such transitions. Making use of Eqs. (2.30) and (2.40), we obtain

$$\begin{aligned} M_{n(s),m(s)} &= \left\langle c_s^{(n)} \left| \zeta_s^{(m)} \right.\right\rangle\,; \\ &= \pm\frac{\gamma a}{\hbar}\sin(\frac{k}{2}) N_n N_m \left[(-1)^n + (-1)^m\right] S_{n,m}\,, \end{aligned} \tag{2.44}$$

where "+" and "−" are used for VME of transitions between conduction, $s = c$, and valence, $s = v$, subbands. For the specified transitions the optical selection rules are the following: transitions are allowed if ΔJ is an even number and they are forbidden otherwise. These matrix elements and corresponding selection rules should be important in spontaneous emission (photoluminescence) calculations [164].

In the case of $n = m$, VME given by Eq. (2.44) is nothing else but the group velocity of an electron in the n-th band. If $n = m = 1$, then $\theta_n = \theta_m \to 0$ as k approaches the transition point k_t. As a result, in Eq. (2.44) the indeterminacy arises in precisely the same manner as discussed above for Eq. (2.41). In the present case, however, it is essential since the expression in square brackets of Eq. (2.44) is not an exact zero. The indeterminacy can be resolved by the application of L'Hospital's rule twice. This burden, however, can be bypassed by calculating the VME by the aid of simplified expressions for eigenvectors at the k_t provided in Appendix B. Such a calculation yields

$$M_{1(s),1(s)} = \mp\frac{\gamma a}{\hbar}\sin(\frac{k_t}{2})\frac{w+2}{2w+1}\,, \tag{2.45}$$

where the upper (lower) sign is used for the conduction (valence) subband. It is easily seen from the expression above that in the limit of a wide ribbon the electron group velocity at $k_t \approx 2\pi/3$, i.e. approaching to the Dirac point, is $\mp v_F/2$.

Velocity matrix elements for transitions involving edge states can be easily obtained from Eqs. (2.41) and (2.44) with $S_{n,m}$ given by Eq. (2.42) after $\theta \to i\beta$ replacement being applied. It should be noticed that the Eqs. (2.41) and (2.44) obtained here are incomparably simpler than their analogues in Ref. [120] (cf. with Eqs. (18) and (19) therein). In the next Sec. 2.3 we discuss and investigate numerically the obtained results.

2.3 Numerical results and discussion

2.3.1 Electronic properties

The physical properties of graphene nanoribbons are often related to those of carbon nanotubes (CNTs). In particular, one usually compares the electronic properties of graphene nanoribbons with those of carbon nanotubes [117, 118]. In most cases such a comparison is based merely on the fact that an unrolled carbon tube transforms into a graphene ribbon. However, this approach is a crude one. Firstly, because only zigzag (armchair) ribbons with even number of carbon atom pairs can be rolled up into armchair (zigzag) tubes. Secondly, because a more relevant and subtle comparison requires the matching of boundary conditions. It has been shown by White et al. [133] that periodic and 'hard wall' boundary conditions can be matched for armchair ribbons and zigzag carbon nanotubes if the width of the ribbons is approximately equal to half of the circumference of the tubes. In Figure 2.4 we demonstrate that a similar correspondence of the electronic properties takes place for zigzag graphene nanoribbons with w zigzag chains, ZGNR(w), and armchair carbon nanotubes, ACNT($w+1, w+1$) and ACNT(w, w) depending on which parts of the Brillouin zones are matched (see Appendix C). The impossibility of matching a zigzag ribbon with just one of the tubes arises from the secular equation (2.19) linking transverse wave vector θ with the longitudinal wave vector k. For sure, due to the presence of the edge states one should not expect the transport properties of undoped ribbons to be the same as those of tubes, but the equivalence of the optical properties seems to be quite natural thing. However, this is not the case. As was shown numerically [99, 117, 111, 72] and has been demonstrated above analytically, the optical selection rules of zigzag ribbons are different from those of armchair tubes [134, 165, 129, 135, 137] (see also Appendix D). This leads to transitions between the edge states being forbidden, which should also have important implications for zigzag ribbon based superlattices [13, 14, 12]. A somewhat similar picture is observed in the bilayer graphene quantum dots of triangular shape, where the edge states are dispersed in energy around the Fermi level [92].

2.3.2 Optical properties

Optical transition matrix elements

To scrutinise the velocity operator matrix elements (VMEs) for allowed transitions we focus on the zigzag ribbon with $w = 10$. In Figures 2.5 and 2.6 we plotted the VMEs given by Eqs. (2.41) and (2.44) as functions of the electron wave vector in the first Brillouin zone (BZ). Figure 2.5 includes results for an armchair tube for the sake of comparison. All plots are normalized by the graphene Fermi velocity

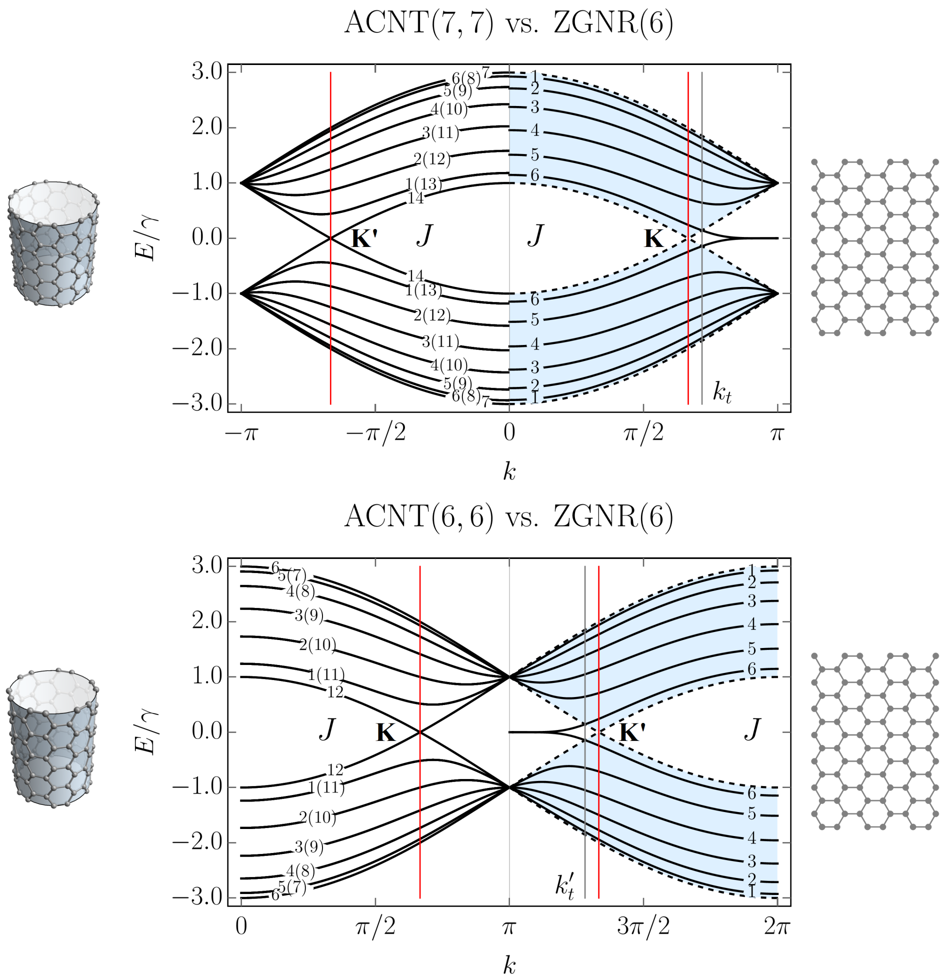

Figure 2.4: A zigzag nanoribbon and armchair nanotube band structure matching. (a) The band structure of an armchair carbon nanotube, ACNT$(7,7)$, compared to (b) that of a zigzag ribbon with $w = 6$, ZGNR(6). (c) and (d) The same as (a) and (b) but for ACNT$(6,6)$. The dashed gray curves encompass light blue area, which signifies the region of the graphene band structure. The vertical lines k_t and k'_t mark positions of the transitions points defined by equation $2\cos(k/2) = w/(w+1)$ in the vicinity of $\mathbf{K}$ and $\mathbf{K}'$ points (i.e. $k = \pm 2\pi/3$), respectively. The inverse band numbering for the ribbon used in Appendix C and direct band numbering for the tube, i.e. for $A = -\cos\theta$, are shown. The corresponding atomic structures are presented on both sides for clarity.

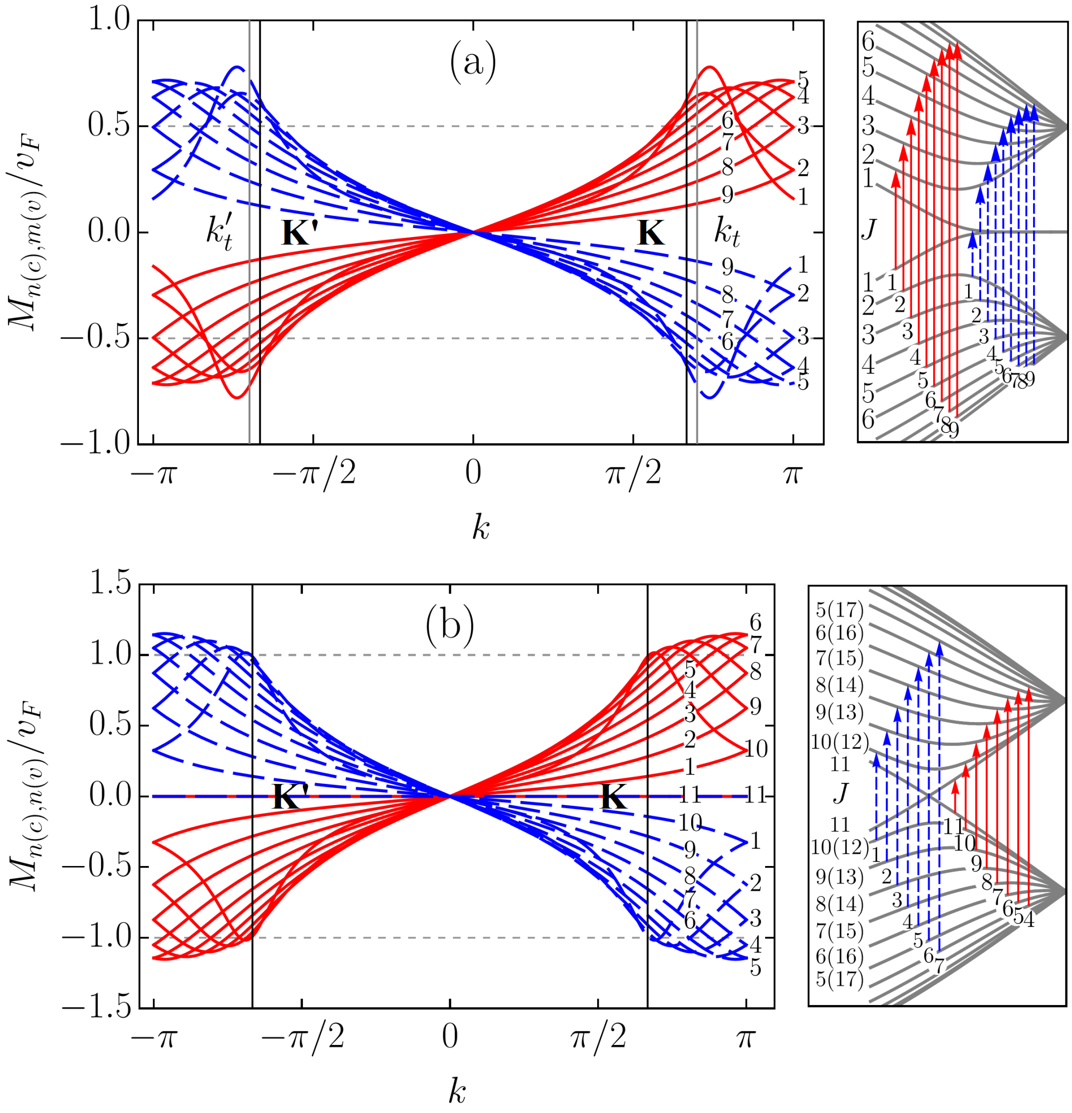

Figure 2.5: The velocity operator matrix elements of a zigzag nanoribbon and armchair carbon nanotube with similar k-dependence. (a) The VMEs of ZGNR(10) transitions $v \rightarrow c; \Delta J = 1$ within the first Brillouin zone in comparison with (b) those of ACNT(11, 11) transitions $v \rightarrow c; \Delta J = 0$. The labels of the VME curves correspond to those of vertical arrows presenting the transitions in the right panels. The index J shows the direct band numbering resulting from Eq. (2.11) for the ribbon and inverse numbering for the tube (see Appendix C). The double degenerate tube's bands have two labels. Dashed arrows represent transitions between the bands numbered in round brackets.

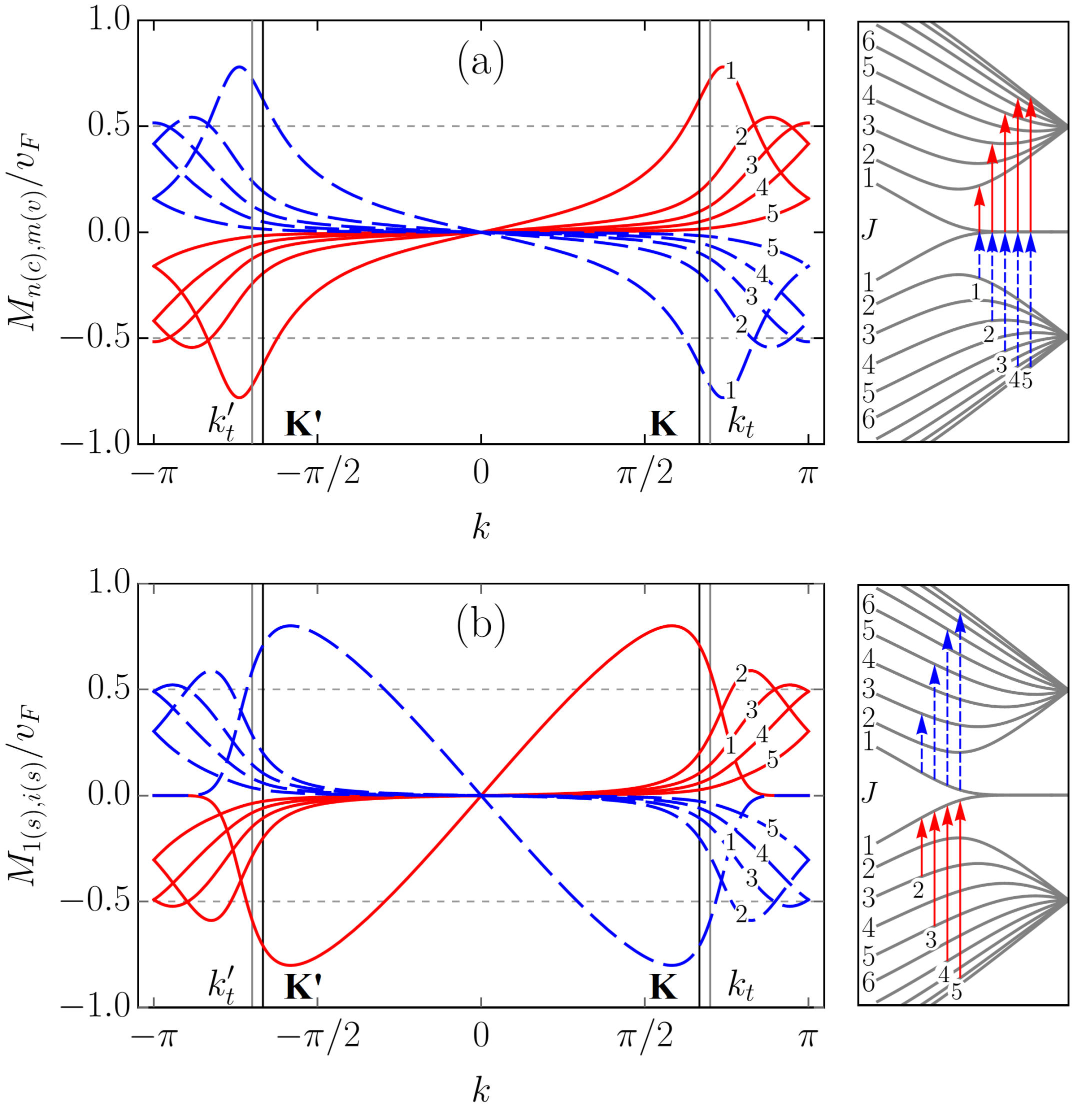

Figure 2.6: The velocity operator matrix elements for transitions inherent to zigzag ribbons. The VMEs of the allowed transitions of ZGNR(10) within the first Brillouin zone: (a) $v \to c; \Delta J = 1, 3, 5, \ldots$; (b) $v \to v; c \to c; \Delta J = 0, 2, 4, \ldots$. The VME curves and energy band labeling follows the same convention as in Fig. 2.5.

$v_F = \sqrt{3}a\gamma/(2\hbar)$. The arbitrary phase factor of the VMEs, which does not affect their absolute values, was chosen such that it favours plots' clarity. As in previous sections, we follow the adopted two index notation for the ribbon bands: $J(s)$, where $J = 1, \ldots, w$ is the band number and $s = c, v$ is the band type with 'c' and 'v' standing for conduction and valence band, respectively. With this notation in mind one can see that the VME curves for transitions $j(v) \to (j+1)(c)$ $[(j+1)(v) \to j(c)]$, where $j = 1, \ldots, w-1$ are shown in Fig. 2.5 (a). The VME curves for transitions $1(v) \to 2n(c)$ $[2n(v) \to 1(c)]$, where $n = 1, \ldots, w/2$ or $(w-1)/2$, and for transitions between conduction (valence) subbands only, i.e. $1(s) \to (2n-1)(s)$, where $n = 1, \ldots, w/2$ or $(w-1)/2$ are presented in Fig. 2.6 (a) and (b), respectively. As one can see, the VME curves deviate significantly from the previously reported $\sin(k/2)$ behaviour [111, 120], according to which extrema are to be at $k = \pi$, i.e. at the edge of the BZ. The deviation is due to the $S_{n,m}$ and N_j given by Eq. (2.42) and (2.31) (see also Eq. (B.4)), respectively. The shift of the VME curve extrema from the BZ edge is larger for low-energy transitions. Interestingly enough, the positions of these extrema in BZ do not coincide with those of the energy band extrema resulting in the van Hove singularities in the density of states. The curves labeled by '1' in Fig. 2.5 (a) and Fig. 2.6 (a) represent direct transitions from the edge states to the closest in energy bulk states. These curves have the largest magnitudes among the ribbons VMEs. However, even for them the maximum absolute values are well below v_F, in sharp contrast to what is seen in Fig. 2.5 (b) for ACNT(11, 11) (cf. Refs. [135, 161]). Though it is difficult to ignore the fact that shapes of the VME curves '2' to '9' in Fig. 2.5 (a) are very similar to those obtained for ACNT VMEs in Fig. 2.5 (b). The most profound curves in Fig. 2.6 (b) are also labeled by '1', but they do not have corresponding transitions depicted in the panel to the right. This is because these curves are, in fact, the electron group velocities in $1(v)$ and $1(c)$ subbands given by Eq. (2.44). As can be seen, at the transition points k_t and k_t' marked by vertical lines the group velocity curves have magnitudes about $v_F/2$. This is in accordance with Eq. (2.45). Ignoring the group velocity curve, one finds that the most prominent magnitudes of VME have transition $1(c) \to 3(c)$

$[3(v) \to 1(v)]$. The probability rate described by VMEs of $1(s) \to (2n-1)(s)$, where $n = 3, \ldots,$ transitions is comparable to that of transitions $1(v) \to 2n(c)$ $[1(c) \to 2n(v)]$, where $n = 2, \ldots,$ labeled by '2', '3', '4' etc., in Fig. 2.6 (a) and (b). However, these transitions are less intense compared to $1(v) \to 2(c)$ $[2(v) \to 1(c)]$, or majority of the $j(v) \to (j+1)(c)$ $[(j+1)(v) \to j(c)]$, where $j = 1, \ldots, w-1$, transitions presented in Fig. 2.5 (a). A regular smooth behavior of all matrix elements at the $\mathbf{K}(\mathbf{K}')$ and k_t (k_t') points is worth highlighting, especially for those including $1(s)$ subbands. We noticed, however, that for increasing ribbon width (up to $w = 25$) the VME curve peaks for transitions involving $1(s)$ subbands gain a sharper form, therefore a singular VME behaviour may still be expected for $1(v) \to 2(c)$ $[2(v) \to 1(c)]$ transitions in ribbons with $w > 25$.

Absorption

It follows from Figs. 2.5 and 2.6 (see also Appendix E) that the absorption spectra of zigzag ribbons are mostly shaped by $v \to c$ transitions with $\Delta J = 1$ presented in Fig. 2.5 (a). However, other transitions may play an important role at certain conditions created by interplay of the doping (or temperature) and ribbon width. To check this we investigated optical absorption spectra given by Eq. (2.34) for narrow ribbons with $w = 2 \ldots 10$. In what follows we discuss ZGNR(6) for it has the most prominent features and additionally it has been recently synthesised with atomically smooth edges [25].

Figure 2.7 compares the absorption spectra of ZGNR(6) for various positions of the Fermi level, E_F. As one can see, depending on E_F the absorption spectrum has 4 or 5 pronounced peaks, which we label in ascending order of their frequency as A, B, C, D, and E. Peaks D and E are not sensitive to the doping, whereas peaks A, B, and C are. In contrast to peaks A and C undergoing suppression with increasing E_F, peak B significantly strengthens. Such different behaviour of the three peaks is explained by their different nature.

Let us start with the most interesting case of the peak B at $\omega = 0.9\gamma$, which corresponds to the wavelength of about 400 nm if $\gamma \approx 3$ eV. This peak stems from

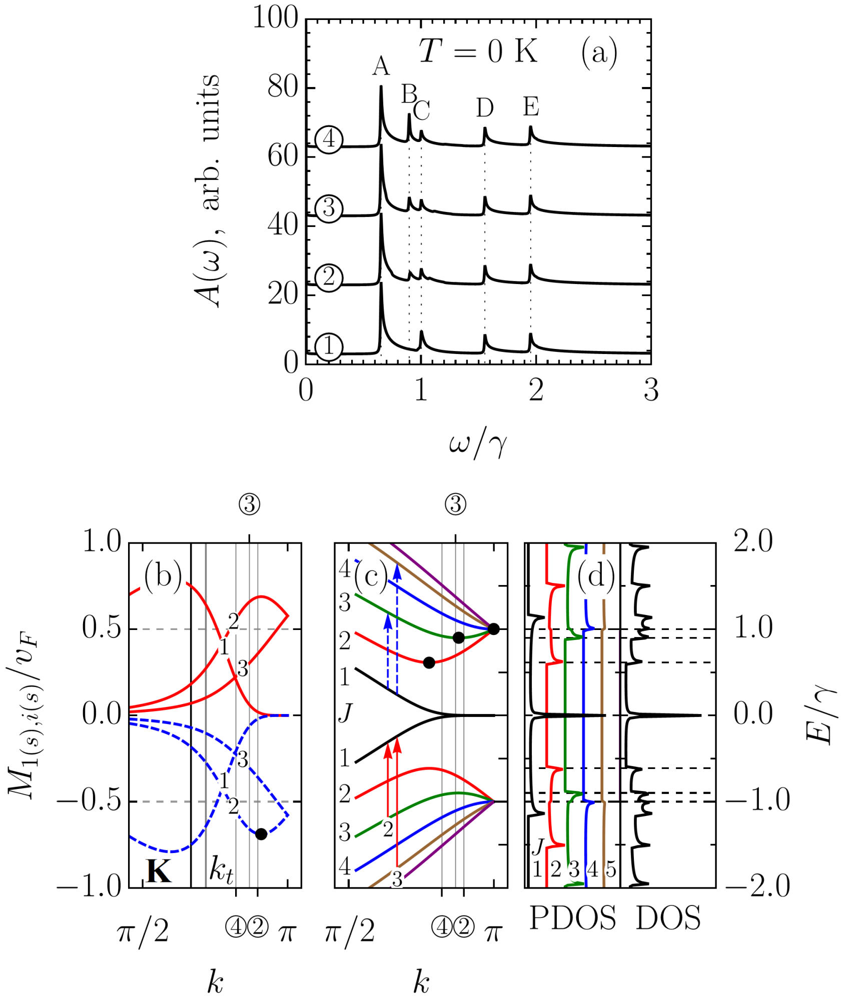

Figure 2.7: The doping-dependent absorption peaks in zigzag graphene nanoribbons. (a) The absorption spectra of ZGNR(6) for various positions of the Fermi level: $E_F = 0$, 0.001γ, 0.004γ and 0.02γ for the curves ①, ②, ③ and ④, respectively. The frequency ω is measured in hopping integrals γ. The spectra are shifted vertically for clarity. (b) The VMEs for transitions depicted in (c) the band structure of ZGNR(6). The vertical lines labeled by encircled numbers mark the positions of the points where the Fermi levels cross the $1(c)$ subband. The thick black points signify subband and VME extrema. (d) The partial, i.e. for each subband separately, and total density of states for ZGNR(6). The color and number of the partial density of states curves correspond to those of the relevant subbands presented in (c); these curves are also offset horizontally for clarity.

transitions $1(c) \to 3(c)$. At $T = 0$ K valence subbands are fully occupied therefore we can safely exclude from the consideration transition $3(v) \to 1(v)$, which must be blocked due to the exclusion principle. The steep doping dependence of the peak B observed in Fig. 2.7 (a) has two causes. Firstly, dispersion of subbands $1(c)$ and $3(c)$ and resulting density of states $\sim (\partial E_{j,s}(k)/\partial k)^{-1}$ presented in Fig. 2.7 (d). Secondly, the non-zero VMEs for transition $1(c) \to 3(c)$ in the k-interval $(2\pi/3, \pi)$, as shown in Fig. 2.7 (b).

Without doping the peak B is absent in the absorption spectrum because both subbands $1(c)$ and $3(c)$ are empty. The introduction of doping results in large number of edge states in the almost flat subband $1(c)$ being occupied with electrons. If the point of the Fermi level intersection with the subband $1(c)$ is denoted as k_F, then one can say that k_F rapidly shifts towards the $\mathbf{K}$ point upon ribbon doping. In Figure 2.7 (b) and (c) the values of k_F for $E_F = 0.001\gamma$, 0.004γ, and 0.02γ are marked by vertical lines labeled as ②, ③, and ④, correspondingly. As seen in Fig. 2.7 (b) at $E_F = 0.001\gamma$, i.e. $k_F =$②, VME of $1(c) \to 3(c)$ transition represented by curve '2' is close to the maximum magnitude, nevertheless the intensity of the peak B in Fig. 2.7 (a) presented by curve ② is not that large. The low intensity at such a level of doping is related to the fact that the subband $3(c)$ has a dispersion to the right of the vertical line ② which leads to transitions although being strong contribute into absorption at different frequencies. Upon further increase of the E_F up to 0.02γ, i.e. $k_F =$④, the VME for $1(c) \to 3(c)$ transition decreases in magnitude to about $v_F/2$. However, due to the flatness of subband $3(c)$ in the vicinity of the band minimum (thick black point in Fig. 2.7 (c)), all the transitions between lines ② and ④ contribute into absorption nearly at the same frequency, which corresponds to the van Hove singularity in the density of states shown in Fig. 2.7 (d). This results in the sharp enhancement of the peak B.

The filling of the subband $1(c)$ with electrons affects all the transitions: $1(c) \to 3(c)$, $5(c)$ etc. However, in ZGNR(6) the higher order transition $1(c) \to 5(c)$ is buried in the peak C for it has lower density of states compared to the subband $4(c)$. To observe higher order transitions one has to take a wider ribbon. Any of the ribbons $w = 8, 9, 10$ can be chosen but ribbon with $w = 9$ is the best choice for there transitions $1(c) \to 5(c)$ results in a clear peak at $\omega \approx \gamma$.

According to our calculations, ZGNR(6) and ZGNR(7) are the best choices for a detection of the tunable peak due to $1(c) \to 3(c)$ transitions. The latter is in agreement with the results of Sanders et al. [122, 123] based on the matrix elements of the momentum and with the wave function overlapping taken into account. For wider ribbons the peak broadens and loses intensity due to combined effect of the VME and density of states reduction.

As for peaks A and C at $\omega = 0.65\gamma$ and γ in Fig. 2.7 (a), they arise from interband transitions $1(v) \to 2(c)$ $[2(v) \to 1(c)]$ and $1(v) \to 4(c)$ $[4(v) \to 1(c)]$, respectively. Strictly speaking, many subbands converge into $E = \pm\gamma$ at $k = \pi$, therefore some other transitions also contribute into the peak C. By mentioning only one type of transition we mean the dominant contribution in terms of density of states as indicated in Fig. 2.7 (d). The intensity of the peak C decreases with doping for it results in the subband $1(c)$ being filled with the electrons whereby transitions $4(v) \to 1(c)$ are blocked due to the exclusion principle. The same Pauli blocking also takes place for transitions $2(v) \to 1(c)$, therefore intensity of the peak A decreases too. A more gentle decrease of peak A intensity compared to that of peak C is due to low doping. As one can see in Fig. 2.7 (c), for the chosen values of the Fermi level the point k_F does not reach position of the subband $2(c)$ minimum. For larger doping A peak intensity decreases as it happens for peak C, and it totally disappears if the doping is high enough to attain the $2(c)$ subband. The effect of the finite temperature is similar to that of doping discussed above (see Appedix E).

Finally, let us compare the zigzag nanoribbon absorption spectra with those of armchair nanotubes. In Figure 2.8 (a) the absorption spectra of ZGNR(10) and ACNT(11, 11) are presented together with that of ACNT(10, 10). For the sake of comparison each spectrum is not normalized by the number of atoms in the unit cell. The first peculiarity, which one can notice, is that in the ribbon all but the lowest in energy absorption peaks lose approximately half of their intensity compared to the peaks in the tubes. The second peculiarity is that ZGNR(10) and ACNT$(11, 11)$ have the same pattern of absorption peaks in the high frequency range $\omega > \gamma$, which is highlighted in the light blue. Both features are not accidental, as follows from the plots presented in Fig. 2.8 (b)-(d) for ribbons and tubes of larger transverse size.

In order to explain the noticed difference and similarity we focus on ZGNR(10) and ACNT$(11, 11)$. Obviously, a large difference in peak intensities between the tube and ribbon cannot be explained only by the velocity matrix elements being higher in the tube than in the ribbon, as follows from Fig. 2.5, therefore the density of states should be accounted for. Here we do not appeal to the suppression due to the momentum conservation as in Ref. [120] for we regard all transitions, even between subbands with different indices, as direct ones. At the same time, the correlation of the absorption peaks' positions is to be related to the van Hove singularities in the density of states too. Thus, we need to have a closer look at the band structures and density of states of ZGNR(10) and ACNT$(11, 11)$. In Figure 2.8 (e) the ZGNR(10) band structure (solid curve) is compared with that of ACNT$(11, 11)$ (dashed curve). Similar comparison is presented for the density of states in Fig. 2.8 (f). The peaks numbered as '1', '2', '3' and '4' in Fig. 2.8 (a) result from the transitions between ACNT$(11, 11)$ subband extrema marked by numbered circles in Fig. 2.8 (e). The same peaks in ZGNR(10) originate from the transitions involving the subband extrema marked in Fig. 2.8 (e) by the numbered squares (triangles) for the conduction (valence) subbands. Selection rules in both structures allow transitions between the markers of the same shape. Let us be more specific and focus on the peak '1'. In ACNT$(11, 11)$ this peak is due to transition between two van Hove singularities in the density of states. Although the density of states in the tube is nearly twice as high as than that in the ribbon due to the double degeneracy of the tube's subbands, this cannot explain the difference in the intensities of the tube and ribbons absorption peaks, since, according to the selection rules, two type of transitions with the same frequency are allowed in the ribbon: $3(v) \rightarrow 2(c)[2(v) \rightarrow 3(c)]$. The difference in intensities arises due

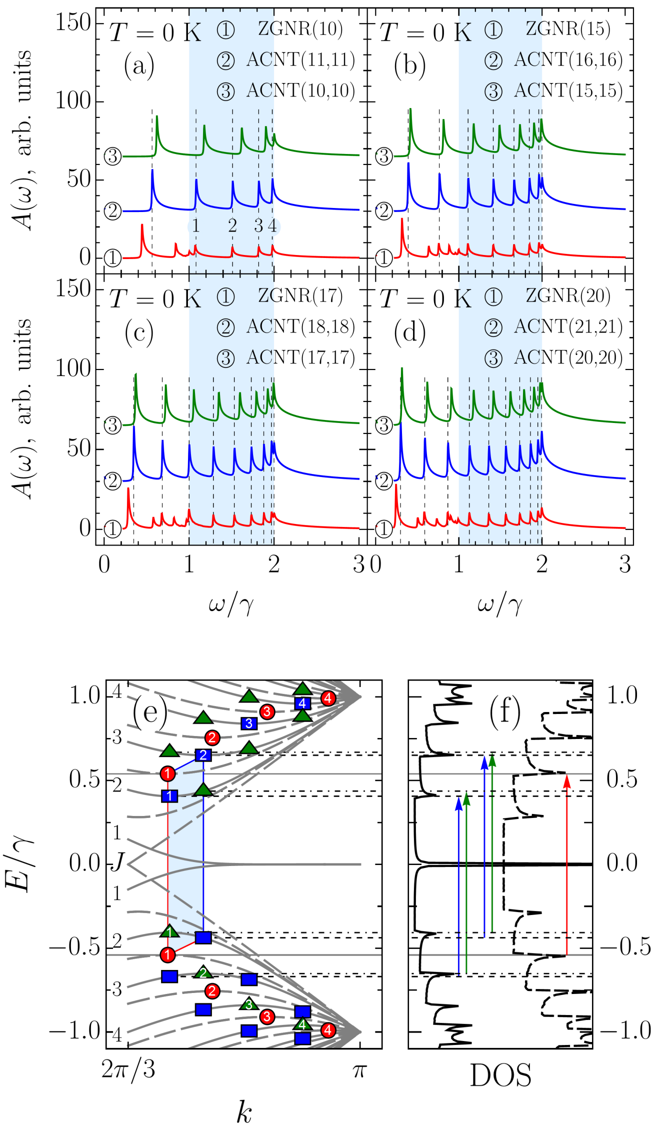

Figure 2.8: The absorption peak correlation in zigzag nanoribbons and armchair nanotubes. (a)-(d) The absorption spectra of ZGNR(w) compared to those of ACNT($w+1, w+1$) and ACNT(w, w) for various ribbon widths and $E_F = 0$. Absorption spectra are shifted vertically for clarity. (e), (f) The band structure and the density of states for ZGNR(10) (solid) and ACNT(11, 11) (dashed). The density of states curves are offset for clarity. The numbered circles denote the positions of the van Hove singularities in the tube. The numbered squares and triangles denote the van Hove singularities in the conduction and valence subbands of the ribbon, respectively. Transitions $v \to c$ are possible only between the markers of the same shape.

the fact that positions of the band extrema for adjacent bands in the ribbon are shifted in the k-space, thereby each of the specified in Fig. 2.8 (e) ribbon transitions happens either ‘from’ or ‘to’ the band extrema and not ‘between’ them as happens in the tube. In other words, each of these transitions involves only one van Hove singularity. In this view, the extremely high intensity of the lowest in energy absorption peak in ZGNR(10) arises due to the high density of states originating from the flatness of the $1(c)$ band dispersion at $E = 0$.

As one can notice from Fig. 2.8 (e), the tube subband extrema take middle positions in energy between extrema of adjacent ribbons subbands. This leads to the tube’s and ribbon’s transition energies being very close as illustrated by a parallelogram in Fig. 2.8 (e). As a result, a correlation between the absorption peak positions arises. To understand the origin of this correlation we need to analyse the positions of the van Hove singularities, which can be derived from the analytical expression for the band structure. However, for a zigzag ribbon, such an expression cannot be obtained in a closed-form from Eq. (2.14), since the secular equation (2.19) does not allow expressing of its solution in such a form; though closed-form solutions for two specific cases, $k = 2\pi/3$ and π, have been reported for this type of equation [94, 139, 112]. On the other hand, since the armchair nanotube band structure has a closed-form given by Eq. (C.6), the positions of the van Hove singularities and, therefore, the absorptions peak positions can be easily obtained for them. Then, a simple analytical expression for ACNT$(w+1, w+1)$ peak positions,

$$\widetilde{\omega}_j = 2\gamma \sin[\pi j/(w+1)]\,, \tag{2.46}$$

can be used as an estimation of the absorption peak positions in ZGNR(w), when $5/6 > j/(w+1) > 1/6$. In Figure 2.8 (a) the vertical dashed lines denote the peak positions given by Eq. (2.46). As one can see, outside the light blue regions peak positions do not necessarily coincide; the ribbon spectra also have additional peaks outside these regions resulting from transitions involving $1(s)$ subbands and the selection rule $v \to c$ $\Delta J = 1, 3, \ldots$ etc. In contrast to this, within the regions $\gamma < \omega < 2\gamma$ the above-mentioned correlation takes place for all ribbons with

Table 2.1: The absorption peak positions of ZGNR(10) in the region $\omega > \gamma$ compared to the estimate $\widetilde{\omega}_j$ given by Eq. (2.46) and transition energies between the states $j(v) \to (j+1)(c)$ denoted by $\Box$'s and $\triangle$'s in Fig. 2.8 (e). The index i numbers the peaks in Fig. 2.8 (a). The last column presents the energy differences between the numbered subband extrema in Fig. 2.8 (a). All quantities are measured in the hopping integral γ.

i	j	ω_i	$\widetilde{\omega}_j$	$\Box_v \to \Box_c$	$\triangle_v \to \triangle_c$	$\Box_i - \triangle_{i+1}$
1	2	1.074	1.081	1.089	1.076	1.058
2	3	1.509	1.511	1.527	1.518	1.491
3	4	1.821	1.819	1.839	1.833	1.799
4	5	1.983	1.980	2.000	1.998	1.959

$w \geq 5$. To estimate the reliability of Eq. (2.46) in Table 2.1 we compared the numerically calculated peaks positions in the ZGNR(10) with those resulting from Eq. (2.46). We supplemented these results with numerically evaluated energies of $j(v) \to (j+1)(c)$, where $j = 2, 3, 4, 5$, transitions involving one band extremum state, i.e. those which occur between the states denoted by square ($\Box$) and triangle ($\triangle$) markers in Fig. 2.8 (e). As seen from Table 2.1, a deviation of $\widetilde{\omega}_j$ from ω_i does not exceed 1% of the hopping integral, i.e. 30 meV for $\gamma \approx 3$ eV. It also follows from the Table 2.1 that the above presented picture is a simplified one. In reality the absorption peaks are averages of all transitions taking place in between the two subband extrema shifted in the k-space so that peak positions ω_i and their estimates $\widetilde{\omega}_j$ are squeezed between the $j(v) \to (j+1)(c)$; $(\Box, \triangle)$ transition energies and the energy differences between the corresponding van Hove singularities, $\Box_i - \triangle_{i+1}$.

The panels (b)-(d) in Fig. 2.8 show that the aforementioned correlation may extend to the low-energy region $\omega < \gamma$. This region of a ribbon's spectrum is dominated by the transitions originating from the edge states. It is evident that the absorption peaks originating from these transitions cannot correlate with the peaks in armchair tubes. In fact, they can only hide this feature. In order to verify our assumption, in Fig. 2.9 we split the ZGNR(20) absorption spectrum into two parts: ‘part I’ containing only transitions involving the $1(s)$ subband, i.e. edge states, and ‘part II’ containing the rest of the transitions. As can be seen from Fig. 2.9, it is the latter that correlates with the tubes’ absorption spectrum. Only the first absorption peak in $\mathrm{ACNT}(21,21)$ does not have a counterpart in the ribbon spectrum. Thus, equation (2.46) has a broader applicability and with its help the hidden correlation could be verified even by absorption measurements in the optical range. Equation (2.46) describes zigzag ribbon peak positions when $j = 2 \ldots w/2$ (even w) or $(w-1)/2$ (odd w).

The revealed correlation of the absorption peak positions in armchair tubes and zigzag ribbons may be affected by excitonic effects. Excitons are known to be important in one dimensional systems due to the enhanced binding energy [166]. However, such effects rarely were a subject of investigation in the metallic families of graphene nanoribbons [167, 168] and carbon nanotubes [169, 170, 171]. Moreover, it seems that attention has never been paid to the high energy transitions, therefore this problem requires a thorough study. Yet, a general qualitative picture says that the positions of the presented peaks should be red-shifted by the amount of the binding energies. These energies can be linked to the system’s transverse size by an analytical phenomenological quasi-one dimensional exciton model, which has been successfully applied to semiconducting quantum wires [172, 173, 174] and carbon nanotubes [175]. Then, since the tubes and ribbons in question have comparable widths and diameters, the binding energies and, therefore, shifts are expected to be close for both structures (neglecting the different shapes of their cross-sections), thereby preserving the unveiled correlation in the absorption spectra. Some excitonic states may require a magnetic field for their brightening if they happen to be dark ones [176]. We should also mention that the correlation reported here can be additionally hidden by a landscape of absorption peaks originating from σ-orbitals.

2.4 Conclusions

In summary, we considered the optical properties of zigzag graphene nanoribbons within the orthogonal π-orbital tight-binding model and effective mass approxi-

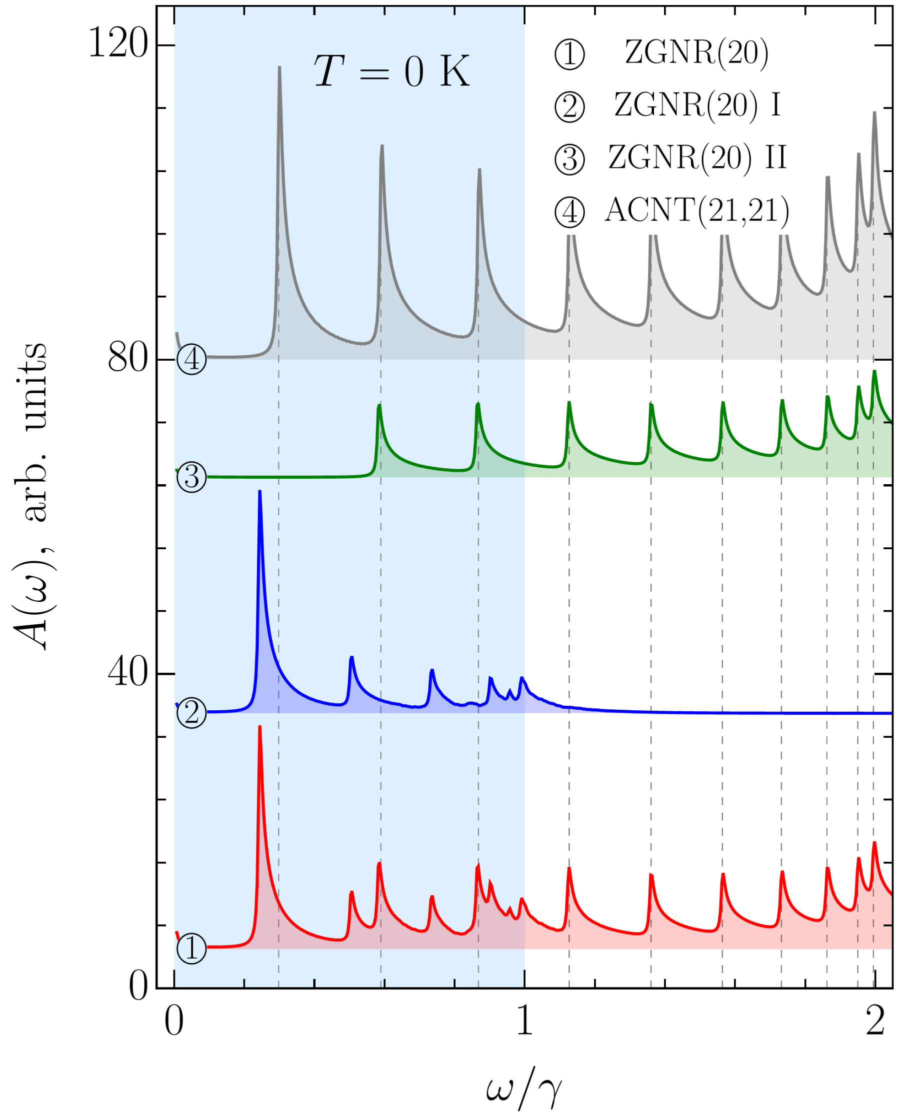

Figure 2.9: The low-energy absorption peak correlation in zigzag nanoribbons and armchair nanotubes. Absorption spectra are shifted vertically for clarity. The roman numbers (I) and (II) label spectra with only the edge states contribution and the part without it. The light blue region signifies the low-energy region where the correlation is hidden by the edge states transitions.

mation for polarization of the incident radiation parallel to the ribbon axis. It was analytically confirmed that the selection rules between valence and conduction subbands, $\Delta J = n - m$ is odd, and between conduction (valence) subbands only, $\Delta J = n - m$ is even, stem from the wave function parity factor, $(-1)^J$, where J is an integer numbering the energy bands. It was also shown that this parity factor originates from the ribbon's secular equation.

A comprehensive comparison of optical properties between carbon nanotubes and zigzag nanoribbons shows significant differences. Most importantly, the concept of cutting lines [177, 178], or even its generalization to 'cutting curves' [112, 179], being unable to explain selection rules fails with respect to optical properties of zigzag graphene nanoribbons, while it works well for armchair carbon nanotubes. Nevertheless, a proper comparison reveals the absorption spectra of a zigzag nanoribbon and an armchair carbon nanotube have a correlation between the positions of the peaks originating from the $v \to c$ transitions between the bulk states , if $N_t = 2N_r + 4$, where $N_{t,r}$ is the number of atoms in the tube's (ribbon's) unit cell, i.e. when the ribbon width is about half of the tube circumference. Putting it differently, for ZGNR(w) and ACNT($w + 1, w + 1$) if $w > 5$.

The analysis of the velocity operator matrix element dependencies on the electron wave vector shows that they have a smooth regular behaviour at least up to $w = 25$ in the whole Brillouin zone, including the Dirac ($k = \pm 2\pi/3$) and transition ($k = k_t$) points. However, the matrix element behaviour deviates significantly from the previous estimation $\sim \sin(k/2)$. For all types of transitions the magnitude of the velocity operator matrix elements attain a maximum value for $k \in \pm(\pi/2, \pi)$.

A close examination of the absorption spectra of zigzag ribbons shows they should have temperature and doping dependent absorption peaks originating from transitions between only conduction (valence) subbands, $\Delta J = 2, 4, \ldots$ etc., which could be tuned, for instance, by a gate voltage. In particular, narrow zigzag ribbons with $w = 6, 7$ should have such prominent temperature and doping dependent absorption peaks. Although beyond the single electron tight-binding model the energy bands of zigzag ribbons are known to be modified by electron-electron interaction [32] and the effect of the substrate, we believe that experimental observation of the tunable absorption should be possible as the latter effect, for instance, can be eliminated by system suspension.

Finally, we point out that the obtained velocity matrix elements of single electron transitions can be utilized in further study of excitonic effects via Elliot's formula for absorption [180, 181].

Chapter 3

Optical and THz transitions in narrow-gap carbon nanotubes and armchair nanoribbons

3.1 Introduction

Creating reliable, portable, tunable sources and detectors of terahertz radiation is one of the most challenging tasks of contemporary applied physics. One of the recent trends in bridging the so-called THz gap is the use of carbon-based nanostructures [46]. A number of schemes have been proposed so far [182, 43, 39, 183, 184, 45]. Several original schemes utilizing the unique electronic properties of graphene and non-simply connected nanostructures such as carbon nanotubes (CNTs) for THz application were brought forward by M. Portnoi group [185, 186, 187, 161, 188]. These schemes include THz generation by hot electrons in quasi-metallic CNTs, frequency multiplication in chiral-nanotube-based superlattices controlled by a transverse electric field, tunable THz radiation detection and optically-pumped emission in metallic CNTs in a strong magnetic field and using graphene *p*-*n* junctions for sub-wavelength polarization-sensitive THz detection. In this chapter we investigate possibility of utilizing direct interband dipole transitions in narrow-gap CNTs, graphene nanoribbons and gapped two-dimensional (2D) Dirac materials for THz devices.

3.2 Carbon nanotubes

Carbon nanotubes are cylindrical structures made from a single sheet of graphene rolled along a particular direction specified by the chiral vector, which for a two dimensional hexagonal lattice is described by two indices: n and m. Within the frame of a simple tight-binding model CNTs can either be metallic or semiconducting. If $n - m = 3p$, where p is an integer, then the tube is predicted to be metallic and have a linear energy dispersion with the conduction and valence bands touch at the point called the Dirac point. For zigag CNTs, which obey the condition $n = 3p$, $m = 0$, the Dirac point is positioned in the center of the Brillouin zone (BZ).

However, this simple model does not take into account the effect of curvature, which plays an important role for small diameter tubes ($1 - 2$ nm). It is now well established that curvature effects encompass three main contributions: the C-C bond contraction, π-orbital tilting and π- and σ-orbitals mixing [189]. All three contributions can be treated within the tight-binding model if one introduces corrections to the hopping integrals. With the exception of armchair nanotubes, these corrections result in a small band gap opening at the Dirac point of metallic CNTs. This means that these nanotubes are in fact quasimetallic and have band gaps of about 50 meV [67, 69]. These small band gaps do not have much of an affect on the nanotubes' transport properties at room temperature because real samples of CNTs are always spuriously doped by chemicals used in the sample's preparation. However, the situation changes drastically for the optical properties of quasimetallic tubes. Neglecting the effect of curvature, the probability rate of interband transitions between the closest valence and conduction subbands has a linear dependence on the electron wave vector measured form the Dirac point. This means that in the vicinity of the Dirac point interband transitions are suppressed. In contrast, if curvature effects are taken into account, interband transitions within a narrow region around the Dirac point become strongly allowed. As one can see from Fig. 3.1, there is a profound peak at the Dirac point for the magnitude of the velocity operator matrix element (VME), $v_{cv,T}$, as a function of the electron wave vector k. Hereafter, we consider only transition polarized along the structure axis. The peak has a characteristic height, which is independent of the tube's chirality and equal to the Fermi velocity of electrons in graphene ($v_F \approx 10^6$ m/s). The shape of the peak is described by the Lorentzian-like term in the expression:

$$v_{cv,T}(k) = v_F \left(\frac{a_0 \cos(3\theta)}{4} k - \frac{\Delta k}{\sqrt{\Delta k^2 + k^2}} \right) , \tag{3.1}$$

where $\Delta k = E_{\rm g}/(2\hbar v_F)$, with $E_{\rm g}$ being the band gap, $a_0 = 0.142$ nm is the distance between the nearest carbon atoms and θ is the chiral angle. The chiral angle $\theta = 0$ and $\pi/6$ for zigzag and armchair tubes, respectively.

In equation (3.1) Δk has meaning of the shift of a cutting line [177] passing through the **K** point in the reciprocal space of graphene with respect to the Dirac point. Such lines are obtained by quantization of the electron momentum in the circumference direction: $k_C = 2\pi\ell/C_h$, where C_h is the tube circumference, ℓ is an integer. Here we define the Dirac point as the point in which valence and conduction subbands touch, while **K** point is, as usual, a corner of the graphene first Brillouin zone. When intrinsic strain induced by curvature is taken into account, the Dirac and the **K** point no longer coincide and there is a shift between them. Such an interpretation with a reference to the graphene reciprocal space implies that Eq. (3.1) has a universal character in that sense that its second term describes the peak shape for any quasi-metallic tube. This interpretation also allows one to incorporate the effect of an external magnetic field. It has been shown that this field results in a similar peak at the Dirac point upon application of the external magnetic field along the tube axis [161, 162, 163]. Unlike the intrinsic stain, magnetic field shifts quantization line passing through the **K** point leaving the Dirac point in its primary position. This change can be treated in a similar fashion. In both instances, the quantity that matters is a shift of the cutting line with respect to the Dirac point. Thus, both effects can be incorporated as follows:

$$\Delta k = \Delta k_s + \Delta k_f \, . \tag{3.2}$$

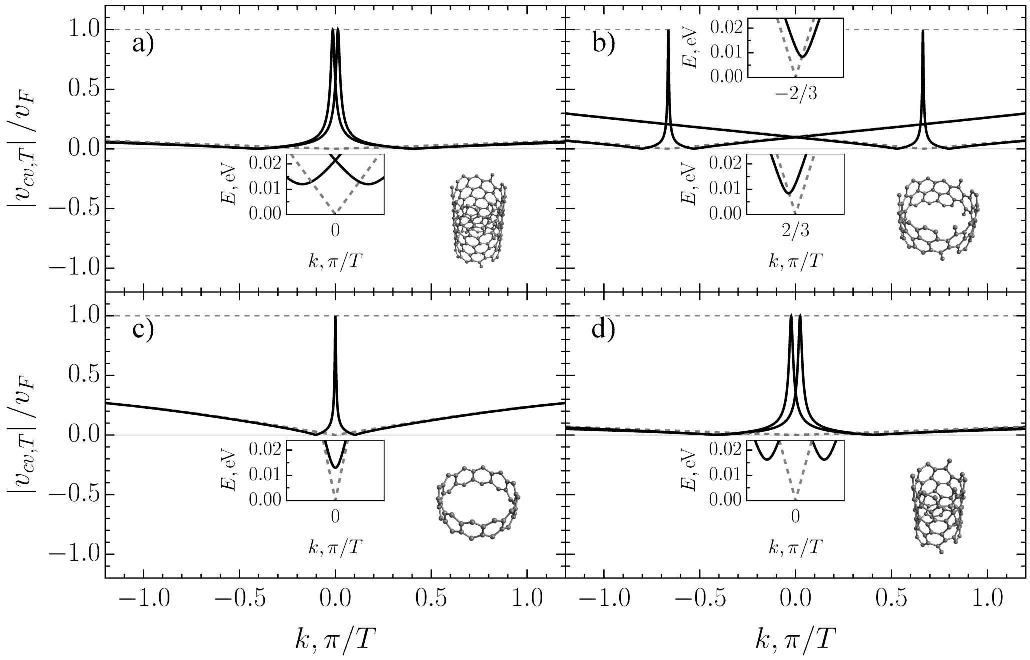

Figure 3.1: The absolute value of the velocity operator matrix element as a function of electron wave vector, k, with (solid black) and without (dashed grey) curvature effect for (a) CNT $(9,3)$; (b) CNT $(12,3)$; (c) CNT $(12,0)$ and (d) CNT $(6,3)$. The conduction band in the vicinity of the Dirac point with (solid black) and without (dashed grey) curvature effect taking into account is presented for each tube in the inserts along with the atomic structure of the CNT unit cells. In all the cases only curvature effect due to the change of C-C bond length was taken into account.

where Δk_s is the shift of the Dirac point from the $\mathbf{K}$ point due to the intrinsic strain, and Δk_f is the shift of the cutting line induced by the magnetic field applied along the tube axis. Contribution of the C-C bond length change into Δk_s can be written in terms of the hopping integrals for the nearest-neighbours t_i:

$$\Delta k_s = \frac{2\sin(\theta)\tau_2 - \left[\sqrt{3}\cos(\theta) - \sin(\theta)\right]\tau_3}{a(t_1 + t_2 + t_3)} \tag{3.3}$$

where $a = \sqrt{3}a_0$ is the graphene lattice translation constant; $\tau_2 = (t_1 - 2t_2 + t_3)$ and $\tau_3 = (t_1 + t_2 - 2t_3)$. Concurrently, the shift due to the applied magnetic field is written as follows:

$$\Delta k_f = \frac{2\pi}{C_h} f \,, \tag{3.4}$$

where C_h is the tube circumference and $f = \Phi/\Phi_0$, with Φ and Φ_0 being magnetic flux through the tube cross-section and magnetic flux quantum, respectively.

Equation (3.1) is an approximation because it was obtained from the velocity matrix element of graphene under the assumption that it preserves its topology in the vicinity of the Dirac point. Similar to the graphene band structure, the matrix element as a function of electron wave vector, can be presented by a surface above the 2D reciprocal space of graphene. At the Dirac point this surface has a non-trivial shape described by the following expression:

$$\frac{k_x}{\sqrt{k_x^2 + k_y^2}} \,, \tag{3.5}$$

where $k_{x,y}$ are the electron wave vector projections onto corresponding axes. Equation (3.5) is an example of the topological phase singularity located at the origin. This feature of the velocity matrix element at the Dirac point is inherited from the graphene wave functions [132]. The topological singularity in the graphene wavefunctions is also responsible for Berry's phase equal to π, suppression of the backscattering and other phenomena such as anisotropic momentum distribution of excited electrons [190]. The topological singularity in the matrix element survives under application of strain and magnetic field to graphene. In terms of this view the second term of the Eq. (3.1) is a cross section of the surface given by Eq. (3.5) which does not change much due to the intrinsic strain or magnetic field. This is illustrated in Fig. 3.2. We verified this assumption comparing approximate VME curve given by Eq. (3.1) with an exact one. According to our results the deviation of the approximate VME curve from the exact one does not exceed 10% for intrinsic strains introducing up to 20% change into the hopping integrals. Concurrently, Eq. (3.1) incredibly well describes the VME peak for all experimentally attainable magnetic fluxes, i.e. produced by up to 30 T magnetic fields, through the $1-2$ nm diameter tube; the deviation is $< 0.1\%$.

It is worth noting that Lorentzian has been proposed to describe modification of the momentum matrix element in silicene due to the spin-orbit interaction [191].

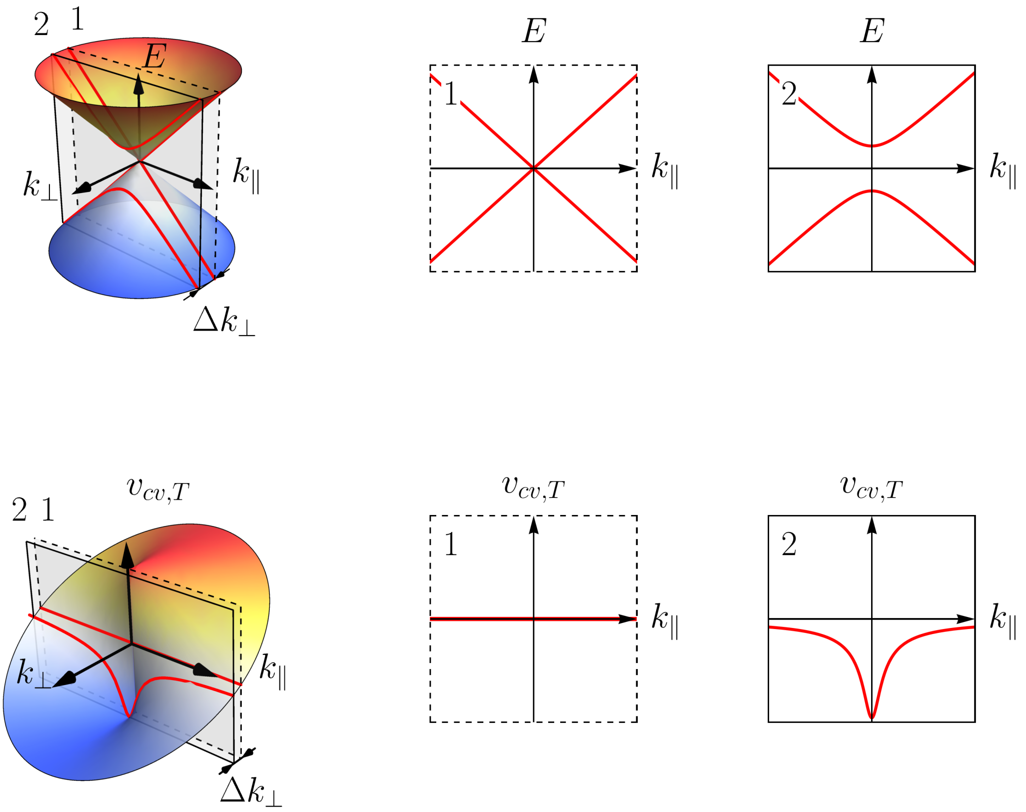

Figure 3.2: The relation of the velocity operator matrix element peak at the Dirac point in tubes to the topological singularity in the velocity operator matrix element in graphene. The top panel illustrates the application of the cutting lines concept to the band structure, while the bottom one to the velocity operator matrix elements. $k_\parallel$ and $k_\perp$ denote electron wave vectors parallel and perpendicular to axis of the tube's translation symmetry.

In equation (3.1), however, because of the presence of the square root in the second term, one deals with a peak shape that is not Lorentzian.

As can be seen from Eq. (3.1), in a CNT Brillouin zone there is a point where velocity matrix element is zero. Equating to zero right hand side of Eq. (3.1) , one can find that the energy of a corresponding forbidden transition is

$$E_{\not\updownarrow} = E_g \sqrt{\left(\frac{1}{4} + \left(\frac{8E_0}{E_g \cos\theta}\right)^2\right)^{1/2} - \frac{1}{2}}\,, \tag{3.6}$$

where $E_0 = \hbar v_F k_0$, with $k_0 = 1/a_0$. As $E_0 \approx 4.64$ eV, which is a huge quantity compared to a typical band gap opened by curvature effect in tubes (≈ 30 meV), without loosing generality exact Eq. (3.6) can be replace by the following approximate one:

$$E_{\not\updownarrow} = \sqrt{\frac{8E_0 E_g}{\cos\theta}}\,. \tag{3.7}$$

Using equation (3.7), it is easy to assess the energy of strictly forbidden transition. For instance, for a zigzag tube with $E_g = 30$ meV, Eq. (3.7) yields $E_{\not\updownarrow} \approx 1$ eV. In reality this energy should be less than the estimate because of the deviation of the electron dispersion from a linear pattern at higher energies.

3.3 Graphene nanoribbons

Graphene nanoribbons (GNRs) represents another type of quasi-one-dimensional carbon nanostructures, which can be imagined as narrow stripes cut from a single layer graphene sheet. The highest symmetry nanoribbons can be classified into the two types – zigzag and armchair. Within each of these classes a ribbon is uniquely specified by the number of carbon atom pairs w, or equivalently by the number of "zigzag lines" for zigzag or "dimer lines" for armchair nanoribbons (see Fig. 1.1). The most simple tight-binding model shows that all zigzag ribbons (ZGNR) are metallic, whereas only armchair ribbons (AGNRs) with $w = 3p + 2$, where p is an integer, are gapless. The low-energy dispersion of electrons in metallic AGNRs is linear and similar to that of metallic CNTs, while electron dispersion of ZGNRs is dominated by edge states. However, in actuality, both types of the metallic ribbons are quasimetallic. The electron dispersion of ZGNR edge states is strongly modified by electron-electron interaction, whereas for AGNR the energy dispersion is influenced by the change of C-C bonds at the edge of the ribbon compared to bonds in the ribbon interior. In both cases the outcome is a small band gap opening of up to 50 meV [103].

In what follows we consider only quasimetallic AGNRs, since as was shown in the Chapter 2 the edge symmetry of ZGNRs results in optical selection rules that do not allow interband transitions of parallel polarization between the highest valence and the lowest conduction subbands.

The band structure of AGNRs without edge effect can be obtained from that of graphene by a technique similar to that used for CNTs if periodic boundary condition applied to the tube, $\boldsymbol{k}_\perp \cdot \boldsymbol{C}_h = 2\pi\ell$, is replaced with so-called "hard wall" or "fixed ends" boundary condition, $\boldsymbol{k}_\perp \cdot \boldsymbol{W} = \pi\ell$, where W is the ribbons width and $\boldsymbol{k}_\perp$ is the transverse momentum. As one can notice these two types of boundary conditions match if $W = C_h/2$. It has been shown that such a situation takes place for AGNR(w) and zigzag CNT($w+1, 0$) [192]. For such specifically chosen structures electronic properties are almost identical. The band spectra of the tube is almost a replica of that for the ribbon, the only difference is that the tube bands are twice degenerate, while ribbon bands are not. It is worth noting that the equivalence is not that perfect for the higher energy bands. The spectrum of tubes contains some bands that are absent in the ribbon spectrum. In Fig. 3.3 (a), (c) we show that described equivalence of the electronic band spectra is held throughout the whole band structure upon accounting for the edge effect in the ribbons and curvature effect in the tubes. The edge effect in armchair ribbons can be incorporated into the tight-binding model as a corrections to the hopping integrals at the ribbon edges [193]. The major change in the band structure is, of course, the opening of a small band gap that is invisible in the main plots and, therefore, is clarified in the insets of Fig. 3.3 (a), (c).

In Fig. 3.3 (b), (d), we demonstrate that equivalence in electronic properties extends to optical transitions selection rules in presence of the curvature for zigzag CNTs and the edge effect for the AGNRs. In Fig. 3.3 (a), (c) some of the velocity operator matrix element curves have negative values. This is because in general matrix elements are complex numbers defined up to an arbitrary phase shift. This uncertainty in the VME phase does not cause any harm since only VME absolute value squared has physical meaning. Therefore, the separation onto negative and positive values is somewhat artificial and here it is used merely for the sake of more clear presentation of a bunch of VME curves. Similar to the situation with the energy bands, the majority of curves, plotted in Fig. 3.3 (d) for the VME of the CNT$(9, 0)$, are twice degenerate compared to the curves presented in Fig. 3.3 (d) for the AGNR(8). The VME plot for the CNT contains also some curves, which are absent in Fig. 3.3 (b) for the AGNR. These curves are related to transitions between higher energy bands that are present only in the spectrum of the tube and are absent in the energy spectrum of the ribbon. The most interesting feature of both plots, however, is depicted by a thick black curve, which corresponds to the VME for transitions between the lowest conduction and highest valence subbands. This curve has a prominent negative dip, which being converted to the absolute values, since only those have physical meaning, corresponds to the peak of the transition probability. As one can see this peak is very similar in both structures. For instance, the magnitudes are $\approx v_F$ and shapes are essentially the same. The only distinguishable difference between two peaks is their widths. For AGNR the peak is wider because the value of the hopping integral edge correction is larger than that for the tube due to the curvature effect. As in the case of Fig. 3.1 only the C-C bond shortening was taken into account in Fig. 3.3 (d). In general, upon increase of intrinsic strain, i.e. correction to the hopping integral, the shape of the peak evolves towards black dashed curves representing VME, which attains the greatest possible value in the structure $\approx 1.3v_F$, Fig. 3.3 (b), (d). However, for any finite intrinsic strain the peak absolute value is $\geq v_F$. Since the variation of the amount of the intrinsic strain results mainly in the peak broadening, one can conclude that transitions across the curvature induced in CNTs and edge effect induced in AGNRs band gaps should stay among the most probable ones in such structures under variety of ambient conditions, such as exposure to different types of the external strain: twisting, stretching etc.

It is worth emphasising that the equivalence of tubes and ribbons optical properties reported here is not at all trivial for although the curvature effect in the tube and the edge effect in the ribbon both represent an intrinsic strain, the former is a homogeneously distributed over the tube surface, while the latter is localised at the ribbon edges.

Finally, we would like to point out that the effect of band gap opening in metallic AGNRs can be explained not only by the hopping integral edge correction but also by the influence of the third order nearest neighbours (3NN) [192]. Using analytical model proposed for electronic properties of AGNRs by Gunlucke [194], we found that in quasimetallic AGNRs inclusion of the 3NN hoping integrals results in a similar to discussed above change of transition probability. However, for Gunlycke model the correspondence between quasimetallic AGNR and zigzag CNT VMEs preserves only for transitions between highest valence and the lowest conduction subbands. This implies that although the Gunlycke model seems to be more advanced for it comprises edge correction to the 1NN hoping integrals and the 3NN hoping integrals all together, it may have some inner flaw compared to the Zheng model [193]. The traces of the 3NN hopping integrals influence on the low-energy absorption in quasimetallic AGNRs can also be found in some numerical studies [127].

3.4 Discussion

In this section we discuss a possibility of experimental observation and practical applications of the transitions across the curvature induced in CNTs and edge effect induced in armchair GNRs band gaps.

The interband transition probability rate per unit volume is determined by the golden rule:

$$I \sim \frac{2\pi}{\hbar} |v_{cv}|^2 \rho \,, \tag{3.8}$$

where ρ is the joint density of states and v_{cv} is the velocity operator matrix element. Thus, we see that intensity of the emitted radiation or the power of absorption is proportional to the product of the VME extensively discussed in the previous sections and the joint density of states. With respect to the joint density of states, it is worth to emphasize the advantage of the band gap opening in 1D systems such as CNTs and GNRs in question compared to 2D systems, such as patterned graphene [195], bilayer [196, 197] and trilayer graphene [198]. The band gap opening

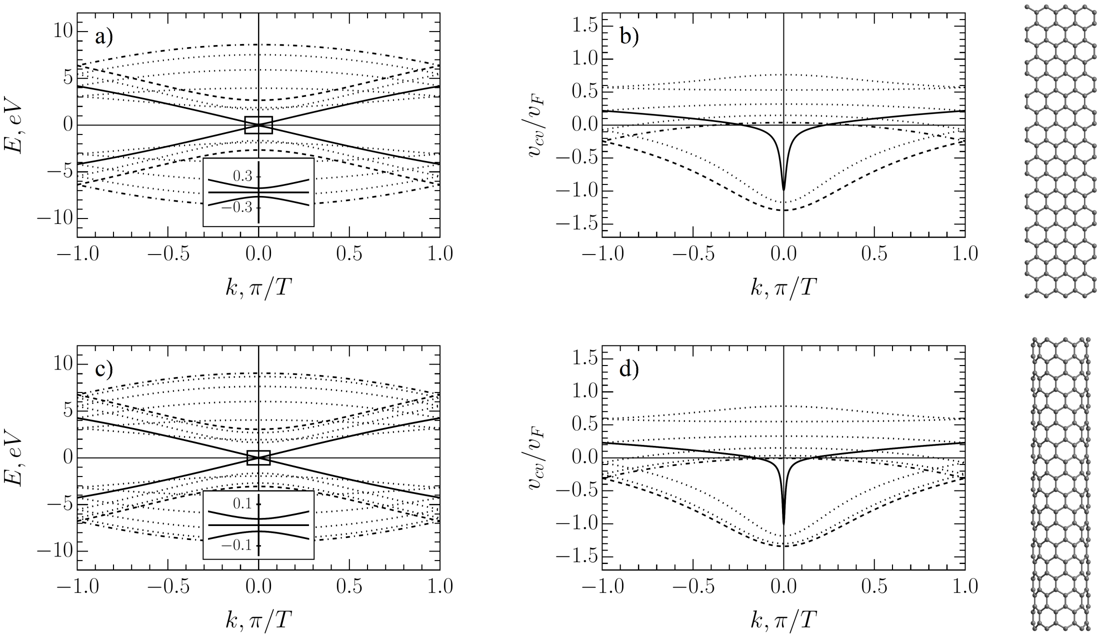

Figure 3.3: The velocity operator matrix elements normalized by v_F (a),(c) and the band structures (b),(d) of AGNR(8) and zigzag CNT$(9, 0)$, respectively. Transitions between the closest valence and conduction subbands (thick, black), the lowest and highest subbands (dashed dotted, light gray), and for the subbands, for which $|v_{cv}|$ attains the maximum possible value (dashed, gray), are highlighted with respect to other bands and matrix elements curves (gray, dotted). Insets zoom the region close to the Dirac point indicated by rectangle to show the band gap opening in both cases. On the right atomic structures are presented. In both cases hopping integral $t = 3$ eV, the edge correction for the ribbon is $0.1t$ and the curvature correction for the tube is $0.01t$.

transforms the linear electron dispersion to the parabolic one. In 2D systems the density of states for parabolic spectrum is a constant, while in 1D systems the density of states is $\sim 1/\sqrt{E - E_0}$. This divergence in density of states of 1D systems is usually referred to as the Van Hove singularity. Owing to this singularity 1D systems effectively behave like quantum dots, where $\rho \sim \delta(E - E_0)$, with δ being the Dirac δ-function, and therefore should benefit from their lower-dimensionality like quantum dot device [34]. Thus, the high probability of the discussed transitions $\sim v_F \approx 10^6$ m/s in conjunction with the Van Hove singularity inherent for 1D structures at band edges should allow an experimental detection of these transitions.

The two types of the experiments for the transitions detection can be proposed, i.e. absorption and emission measurements. The principal difficulty which is characteristic for both types of experiments is related to the fact that size of the band gap corresponds to THz frequencies. On one hand this makes these transitions difficult to detect, but on the other hand it allows us to propose them for THz applications.

Let us consider the absorption experiments first. In this type of measurements one usually faces two principal difficulties. Firstly, as has already been mentioned in Sec. 3.2 in real samples structures are always dopped. For instance, the bottom of the lowest conduction subband in CNTs can filled with electrons up to $\sim$ 120 meV [199], which means the low-energy transitions across the band gap should be suppressed by the Pauli blocking. Secondly, there is another competing and notoriously strong mechanism, whereby absorption occurs. This is absorption on the free carriers or plasmonic absorption. It has been demonstrated that the broad absorption peak in the region $\sim 1-2$ THz for CNTs [200] is of plasmonic origin [201, 202, 203]. Thus, we think it must be difficult to observe the interband transitions in interest by doing absorption measurements.

In the emission type of experiment the sample's response is measured after pumping by laser at optical frequency. In our view, such pumping, if properly adjusted, can be the tool for the transition detection. As schematically depicted in Fig. 3.4, a valence subband electron can be excited above the Fermi level into the conduction subband as schematically shown in Fig. 3.4 a). It is worth noting that such excitation should be possible due to the first term in the Eq. (3.1) describing the linear increase of the transition probability with increasing electron wave vector. The efficiency of excitation can be increased by using broad in frequency beams. After such an optical excitation electrons and holes created in the conduction and valence band, respectively, will quickly thermalise with the lattice due to the scattering on acoustic phonons ($\tau_{ph} \sim 3$ ps [204]). As a result of this process the hole will flow up to the top of the valence band, thereby creating the inversion of population. We track dynamic of the hole because the excited electron disappears below the Fermi level in a sea of indistinguishable particles. As the probability of transition is extremely high at the edge of the valence band, the final stage of the process is emission of photon with a frequency of band gap size, as sketched in the Fig. 3.4 (c).

The sample pumping should result in carrier excitation only between the lowest conduction and the highest valence subbands. The pumping with higher frequencies can result in cascade emissions which should make the sample response more difficult to analyse. The pumping frequency should be low enough to exclude the excitation of the semiconducting structures, for instance for semiconducting nanotubes $1 - 2$ nm in diameter < 0.6 eV, as such structure can be source of THz radiation due to the transient photocurrent [205]. Ideally samples should be enriched with quasimetallic structures, although the presence of the semiconducting structures should not cause much harm as they are transparent for THz radiation. However, the absorption on free carries cannot be avoided, therefore the emitted THz photon before striking detector has a high probability to be absorbed in the sample. This probability can be minimized by proper choice of the structures lengths since the plasmonic resonance is a geometrical one and, therefore, it depends strongly on the structure longitudinal size [201, 202].

In view of possible applications, it is worth mentioning that the band gap of the tubes and ribbons can be manipulated by external fields, thus providing tunability of the emission frequency. For tubes magnetic field can be applied along the tube axis, while for ribbons electric field can be applied in-plane geometry [91, 14]. Such tunability of the transition frequency may be employed as a criteria for distinguishing of the THz radiation generated by interband transitions from that resulting from the photocurrent in semiconducting structures.

Even though in the aforementioned scheme the sample is implied to be composite material consisting of the polymer matrix and filler that is a mixture of the quasimetallic and semiconducting tubes or ribbons, it is worth noting that the syn-

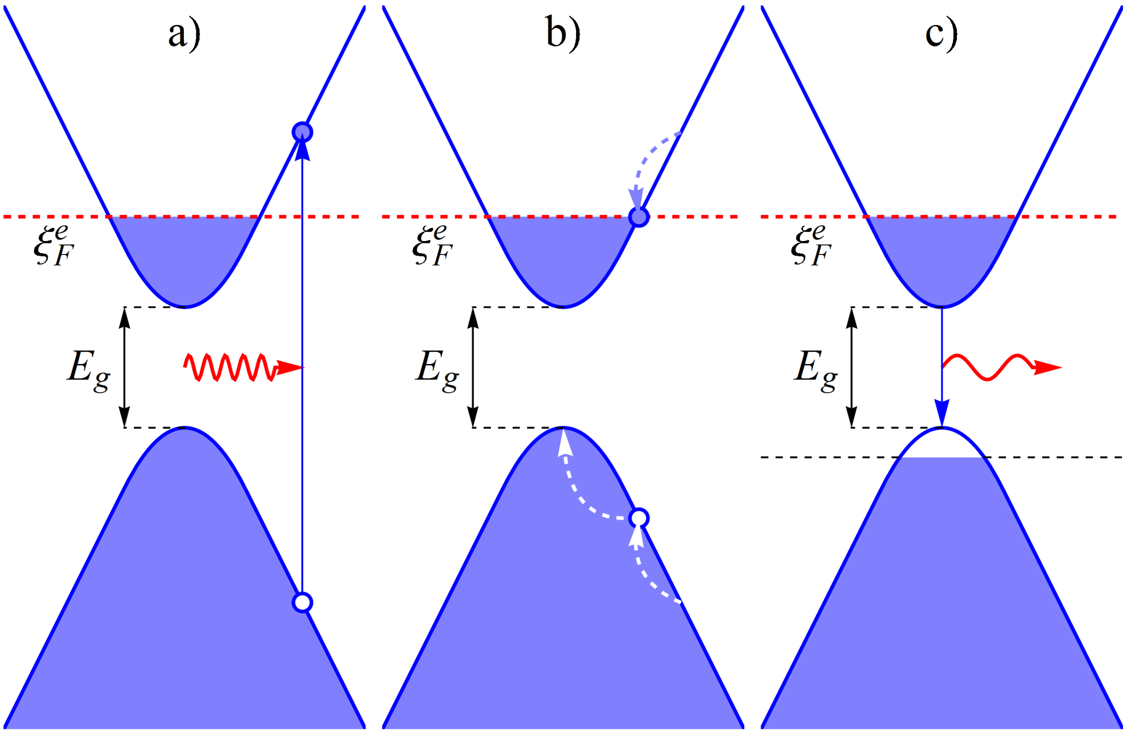

Figure 3.4: A schematic illustration of (a) the high frequency optical excitation (b) non-radiative electron relaxation due to the electron-phonon scattering and (c) the inversion of population in n-doped quasimetallic CNT or GNR after many iterations of the processes depicted in (a) and (b).

thesis techniques for these structures are developing fast. One of the achievements in this field that deserves particular highlight is the recent synthesis of AGNRs of the metallic family with atomically smooth edges [24].

The results presented in Sec. 3.2, 3.3 are based on a single electron picture. In this respect it is make sense to comment on the validity of this picture. Although excitonic effects are known to dominate the optical properties of semiconducting structures [206], the are of less importance in quasimetallic CNTs and ANGRs where the exciton binding energy is proportional to the bandgap [171] and dark excitonic states become irrelevant.

Finally, we may speculate that the same strong transitions may be found in a chemically functionalized graphene sheet with a periodic pattern of hydrogen, oxygen or fluorine adatoms and narrow stripes of graphene intact. The electronic properties of the resulting graphene stripes are known to be similar to those of GNRs [207]. The edge-like effects in the stripes arise from distortions caused by sp^3 hybridization of carbon atoms, which form chemical bonds with adatoms. The low-energy electronic properties are still determined by π-orbitals; therefore, the theoretical treatment of optical properties should be essentially the same as for nanoribbons. An additional tunability of the absorption frequencies of different stripes can be achieved by stretching the whole graphene sheet [208].

3.5 Spin-orbit coupling

In contrast to the two cases considered above where effectively a small perturbation due to the rolling up or cutting of the graphene single layer open up a narrow-band gap, one may have thought of a similar effect in a 2D system due to the spin-orbit coupling. In graphene, however, the band gap due to such a coupling was estimated to be of about 10^{-3} meV [209] and as such it is negligibly small. However, this is different for other honeycomb-like two-dimensional structures made of silicon, germanium or tin. Such materials termed, by analogy to graphene, as silicene and germanene has been synthesised: silicene [3, 4, 5] in 2012, germanene [6] in 2015. Unlike graphene, where sp^2 hybridization of carbon atom orbitals ensures flat geometry, in silicene and germanene the silicon and germanium atoms have sp^3 hybridization of the orbitals resulting in so-called low-buckled geometry of these structures. Nevertheless, the low-energy band structure of these materials is still dominated by π-orbitals and tight-binding model is still applicable for their description [1]. It has been shown that the band structures preserve the Dirac-like dispersion, but in contrast to graphene in the low-buckled structures the spin-orbit interaction is not negligibly small and it opens up a narrow-band gap of about several meV [9]. This interaction can be treated within the tight-binding model as an on-diagonal term in the Hamiltonian. In what follows we shall see how this additional term influences the optical properties of the above-mentioned 2D Dirac materials. In particular we shall calculate optical matrix elements.

Let us start the calculation from the finding the proper energies and eigenvectors of the Hamiltonian of the following form:

$$H = \begin{pmatrix} \lambda_{\text{SO}} & f \\ f^* & -\lambda_{\text{SO}} \end{pmatrix}, \tag{3.9}$$

where λ_{SO} is the spin-orbit coupling constant, $f = \sum_i t_i \exp\left(i\boldsymbol{k}\boldsymbol{R}_i\right)$. The secular equation for this Hamiltonian has the following form:

$$-(\lambda_{SO} - E)(\lambda_{SO} + E) - |f|^2 = 0 \tag{3.10}$$

with the two following solutions:

$$E_{1,2} = \pm\sqrt{\lambda_{SO}^2 + |f|^2}, \tag{3.11}$$

where 1 and 2 corresponds to plus and minus sign, respectively. Thus, the eigenvectors can be found to be

$$\Psi_{1,2} = C_{1,2} \begin{pmatrix} -\frac{f}{\lambda_{SO} - E_{1,2}} \\ 1 \end{pmatrix} \tag{3.12}$$

where C is a normalization constant. The normalization procedure, $\sqrt{\Psi_{1,2}^* \Psi_{1,2}} = 1$, yields

$$|C_{1,2}| = \frac{|\lambda_{SO} - E_{1,2}|}{\sqrt{|f|^2 + \left(\lambda_{SO} - E_{1,2}\right)^2}}. \tag{3.13}$$

Using the gradient approximation one can find velocity operator matrix as follows:

$$\boldsymbol{V} = \frac{\partial H}{\partial \boldsymbol{k}} = \nabla_{\boldsymbol{k}} \begin{pmatrix} \lambda_{\text{SO}} & f \\ f^* & -\lambda_{\text{SO}} \end{pmatrix} = \begin{pmatrix} 0 & \nabla_{\boldsymbol{k}} f \\ \nabla_{\boldsymbol{k}} f^* & 0 \end{pmatrix}. \tag{3.14}$$

Then with the help of Eqs. (3.11), (3.12) and (3.14), one obtains

$$\begin{aligned} v_{12} &= \langle \Psi_1 | \boldsymbol{V} | \Psi_2 \rangle \\ &= \frac{\sqrt{\lambda_{SO}^2 + |f|^2}\left(f^* \nabla_{\boldsymbol{k}} f - f \nabla_{\boldsymbol{k}} f^*\right)}{|f|^2} + \frac{\lambda_{SO}\left(f^* \nabla_{\boldsymbol{k}} f + f \nabla_{\boldsymbol{k}} f^*\right)}{|f|^2}. \end{aligned} \tag{3.15}$$

In the above equation the normalization constants should be restored. Taking into account that

$$C_1 C_2 = \frac{|f|}{2\sqrt{\lambda_{SO}^2 + |f|^2}}, \tag{3.16}$$

for the velocity matrix elements we end up with

$$V_{cv}=C_1C_2v_{12}=\frac{f^*\nabla_{\boldsymbol{k}}f-f\nabla_{\boldsymbol{k}}f^*}{2|f|}+\frac{f^*\nabla_{\boldsymbol{k}}f+f\nabla_{\boldsymbol{k}}f^*}{2|f|}\frac{\lambda_{SO}}{\sqrt{\lambda_{SO}^2+|f|^2}}. \tag{3.17}$$

As one can see in the case of small λ_{SO}, Eq. (3.17) restores the result for graphene, see Appendix D. Thus, the effect of the spin-orbit coupling is contained in the second term of Eq. (3.17). Let us next analyse the same problem in the limit when $f \to 0$.

3.6 Spin-orbit coupling in the low-energy limit

In this section we shall revise the results obtained in the previous section with respect to the the low-energy limit. This time we shall pay particular attention to the phenomenon of momentum alignment for linear polarization and to the optical selection rules for circular polarization of the incident radiation. In what follows, we restrict consideration to the vicinity of the Dirac points in the first Brillouin zone.

The low-energy expansion of the Hamiltonian given by Eq. (3.9) in the vicinity of the two non-equivalent Dirac points has the following form:

$$H=\hbar v_F\begin{pmatrix}\Delta & \kappa_x+i(-1)^v\kappa_y\\ \kappa_x-i(-1)^v\kappa_y & -\Delta\end{pmatrix}, \tag{3.18}$$

where $\Delta=\lambda_{SO}/\hbar v_F$ is again the parameter describing the spin-orbit coupling, v is a valley parameter specifying the point where expansion was carried out, e.g. $v=1(v=2)$ stands for the $\mathbf{K}(\mathbf{K}')$ point, $\kappa_{x,y}$ are the components of the electron wave vector measured from the Dirac point, i.e $\mathbf{K}$ or $\mathbf{K}'$ point. The Hamiltonian (3.18) has the following eigenvalues:

$$\varepsilon_{1,2}=\pm\sqrt{\Delta^2+\kappa^2} \tag{3.19}$$

where indices '1' and '2' correspond to plus and minus sign, respectively, $\kappa^2=\kappa_x^2+\kappa_y^2$. Then, the normalized eigenvectors of the Hamiltonian (3.18) are

$$\chi_{1,2}=\begin{pmatrix}\dfrac{\kappa}{\sqrt{\kappa^2+(\Delta-\varepsilon_{1,2})^2}}\\ -\dfrac{\Delta-\varepsilon_{1,2}}{\sqrt{\kappa^2+(\Delta-\varepsilon_{1,2})^2}}e^{-i(-1)^v\varphi_\kappa}\end{pmatrix} \tag{3.20}$$

where for convenience of the further treatment we have introduced the notation $e^{-i(-1)^v\varphi_\kappa} = (\kappa_x - (-1)^v i\kappa_y)/\kappa$. Substituting Eq. (3.19) into Eq. (3.20) yields

$$\chi_{1,2} = \frac{1}{\sqrt{2}} \begin{pmatrix} \dfrac{\kappa}{\left(\sqrt{\kappa^2+\Delta^2}\right)^{1/2}\left[\sqrt{\kappa^2+\Delta^2}\mp\Delta\right]^{1/2}} \\ \pm\dfrac{\left[\sqrt{\kappa^2+\Delta^2}\mp\Delta\right]^{1/2}}{\left(\sqrt{\kappa^2+\Delta^2}\right)^{1/2}} e^{-i(-1)^v\varphi_\kappa} \end{pmatrix} \tag{3.21}$$

where the upper (lower) sign must be taken for index '1' ('2') corresponding to the conduction (valence) band.

Let us now consider perturbation introduced into the Hamiltonian by an incident electromagnetic wave. The wave can be described by the vector potential as follows:

$$\boldsymbol{A} = \frac{cE}{2\omega}\left(a_x \boldsymbol{e}_x + a_y \boldsymbol{e}_y\right) e^{i\omega t} \tag{3.22}$$

where c is the speed of light, ω is the wave frequency, E is a magnitude of the electric field strength. The parameters a_x and a_y can be defined as

$$a_x = \cos\phi\,; \qquad\qquad a_y = \sin\phi \tag{3.23}$$

for the linear polarization and

$$a_x = 1\,; \qquad\qquad a_y = \mp i\,, \tag{3.24}$$

for the circular polarization. The angle ϕ in Eq. (3.23) is the angle between the vector of the electron quasi-momentum and the plane of the polarization, since we fix x-axis along the quasi-momentum. In Eq. (3.24) the circularly polarized wave is considered as a sum of two waves with x- and y-polarizations and a phase shift of $\pi/2$, signs '+' and '−' are taken for the left- and right-handed circular polarizations, respectively. Having defined the vector potential we can find perturbation via the minimal coupling $\boldsymbol{\kappa} \to \boldsymbol{\kappa} + e\boldsymbol{A}/\hbar c$, which sometimes is also referred to as Peierl's substitution. As was mentioned in Section 2.2.2, this is equivalent to the gradient approximation. The substitution applied to the Hamiltonian (3.18) results in the following perturbations:

$$V_{\text{lin.}} = \frac{v_F eE}{2\omega}\begin{pmatrix} 0 & e^{i(-1)^v\phi} \\ e^{-i(-1)^v\phi} & 0 \end{pmatrix}, \tag{3.25}$$

for linear polarization and similarly for the circular polarization

$$V_{\text{cir.}} = \frac{v_F eE}{2\omega} \begin{pmatrix} 0 & 1-(-1)^{v+p} \\ 1+(-1)^{v+p} & 0 \end{pmatrix} \tag{3.26}$$

where parameter $p = 1 (p = 2)$ defines right-(left-)handedness of the incident radiation.

Using eigenvectors (3.21) one can calculate matrix elements for both perturbations given by Eqs. (3.25) and (3.26). Let us start with the linear polarization. Such a calculation yields

$$\langle \chi_1 | V_{\text{lin.}} | \chi_2 \rangle = \frac{v_F eE}{2\omega} \left\{ i \sin\left[(-1)^v \theta\right] - \frac{\Delta}{\sqrt{k^2 + \Delta^2}} \cos\theta \right\} \tag{3.27}$$

where we have introduced $\theta = \varphi_\kappa - \phi$ as the angle between momentum of the excited electron and the polarization of an incident light. The absolute value squared of the matrix element above can be re-cast in the standard form with the alignment parameter α:

$$F = |V_{\text{lin.12}}|^2 = \left(\frac{v_F eE}{2\omega}\right)^2 \left[\sin^2\theta + \frac{\Delta^2}{\kappa^2 + \Delta^2}\cos^2\theta\right] = F_0(1 - \alpha\cos 2\theta) \tag{3.28}$$

where

$$\alpha = \frac{\kappa^2}{\kappa^2 + 2\Delta^2}\,, \tag{3.29}$$

$$F_0 = \left(\frac{v_F eE}{2\omega}\right)^2 \frac{\kappa^2 + 2\Delta^2}{2(\kappa^2 + \Delta^2)}\,. \tag{3.30}$$

The quantity F presented in Eq. (3.28) can be referred to as photoexcited carriers distribution function [210] since it contains all the information about them. Such characteristics as the number of excited carriers or the angle distribution of their momentums can be obtained from this single function by means of integration. It follows from Eq. (3.29) that for $\kappa \ll \Delta$ there is no momentum alignment of the photoexcited carriers in the gapped 2D Dirac systems and the optical matrix element has a universal value independent of the gap and proportional to the Fermi velocity. As one can see for a linear polarization the valley parameter does not have much of an effect on physics for it is eliminated in the derivation. This, however, will be different for the circular polarization which we are to consider next.

The evaluation of matrix elements for perturbation given by Eq. (3.26) results in rather cumbersome expression depending on valley index v. The general expression can be divided into two part for analysis. Consider first only **K** point for which $v = 1$, then for the right- and left-handed polarization we have

$$\langle \chi_1 \left| V_{\text{cir.r.}} \right| \chi_2 \rangle = \frac{v_F e E}{2\omega} \left(1 - \frac{\Delta}{\sqrt{\kappa^2 + \Delta^2}} \right) e^{-i\varphi_\kappa} \,, \tag{3.31}$$

$$\langle \chi_1 \left| V_{\text{cir.l.}} \right| \chi_2 \rangle = -\frac{v_F e E}{2\omega} \left(1 + \frac{\Delta}{\sqrt{\kappa^2 + \Delta^2}} \right) e^{i\varphi_\kappa} \,. \tag{3.32}$$

It is easy to see from the Eq. (3.31) that for $\kappa \to 0$ the perturbation matrix element vanishes while in Eq. (3.32) it does not. Thus, in the **K** valley only left-handed polarization can excite interband transitions. By contrast, for the $\mathbf{K}'$ valley, i.e. for $v = 2$, we obtain

$$\langle \chi_1 \left| V_{\text{cir.r.}} \right| \chi_2 \rangle = -\frac{v_F e E}{2\omega} \left(1 + \frac{\Delta}{\sqrt{\kappa^2 + \Delta^2}} \right) e^{-i\varphi_\kappa} \,, \tag{3.33}$$

$$\langle \chi_1 \left| V_{\text{cir.l.}} \right| \chi_2 \rangle = \frac{v_F e E}{2\omega} \left(1 - \frac{\Delta}{\sqrt{\kappa^2 + \Delta^2}} \right) e^{i\varphi_\kappa} \,, \tag{3.34}$$

whence by considering the same limit of small κ once can see that in the $\mathbf{K}'$ valley only transitions due to the right-handed polarization are allowed. These are valley and polarization dependent optical selection rules for gapped honeycomb lattices such as in low-buckled silicene, germanene and tinene. It is also worth noting that the obtained selection rules are very much like those for a monolayer of a transitional metal dichalcogenide such as MoS_2 [211]. In general the band gap parameter Δ can be of other origin than the spin-orbit interaction. For instance, it can model the different on-site energies for A and B atoms in graphene on a substrate [212] such as boron nitride [213] or SiC [214, 215].

Finally, we would like to notice that similar to the treatment of carbon nanotubes and graphene nanoribbons in the case of gapped Dirac materials we obtained universal value of the matrix element for linear polarization equal to the Fermi velocity of electron in the structures. However, as follows from Eqs. (3.32) and (3.33) and (3.27), this value of the matrix element at the $\mathbf{K}(\mathbf{K}')$ point for circular polarization is double of that for the linear polarization. For linear polarization, however, the matrix element is the same in both valleys therefore the resulting absorption is the same, but valleys are populated differently by photoexcited carriers. It is also seen from Eqs. (3.32) and (3.33) that for circular polarization the absorption decreases with increasing frequency of excitation and attains a half of its value at gap edge for high enough frequencies corresponding to the linear part of the spectrum.

3.7 Conclusions

In summary, we found strong low-energy interband transitions, which are typically in the THz range, in the quasi-one dimensional narrow-gap carbon nanostructures: carbon nanotubes and armchair graphene nanoribbons. The obtained transition velocity matrix element as function of the electron momentum comprises two parts: the first depends linearly on the electron momentum, while the second has a sharp spiky dependence with a universal value of the peak height equal to the Fermi velocity of electrons in graphene and the peak being positioned at the Dirac point. The non-trivial sharp dependence of the velocity matrix element on the electron wave vector originates form the topological singularity in the graphene's wave functions. The combination of the two parts suggests narrow-gap tubes and ribbons could be used in design of a laser-type device. The high probability rate of the transitions provided by the spiky part of the matrix element together with the van Hove singularity at the band gap edge of the considered quasi-one-dimensional systems makes them promising candidates for active elements in coherent THz radiation emitters. We proposed to verify this feature in the emission rather than absorption type of experiment.

The rolling up of the graphene sheet into tube or cutting it onto ribbons to produce a small perturbation in a form of intrinsic strain which opens up a narrow band gap is not required in 2D Dirac materials with a gap originating, for instance, from the effect of the spin-orbit interaction. Having considered such materials within the tight-binding model we demonstrated that the probability rate of the interband transitions for linear polarization of incident radiation has also a universal value at the Dirac point and it is equal to the Fermi velocity of electrons in the structure. Additionally to the peculiar valley dependent selection rules such that each valley is responsive only to the specific handedness of the circular polarized incident radiation, we obtained that the velocity matrix elements of the transitions induced by the circular polarization at the Dirac point are double of those for higher energies where the electronic spectrum is linear.

Part II

Energy spectra and electro-optical properties of flat nanostructures

Chapter 4

Electro-absorption of silicene and bilayer graphene quantum dots

4.1 Introduction

Non-planar graphene-derivative materials have attracted considerable attention [216, 217, 218, 219, 220, 221, 222, 223] because of their tunable electronic properties, different from those of the single-layer graphene. Application of the electric field, E, across the bilayer (multilayer) graphene system opens a gap between the conduction and valence bands [224, 196, 225, 198]. The same also happens with silicene because of the buckling of its honeycomb lattice [217, 218, 219, 221]. The atoms of the type A and B of the lattice are displaced alternatively in the vertical direction and are subjected to a different, electric field producing, potential gradient. The possibility of controlling the gap offers a wealth of new routes for the next generation of field effect transistors and optoelectronic devices [216, 217, 226]. However, the on-chip nano-scale realization of such devices requires finite-size components like nanoribbons and quantum dots (QDs) [227]. Therefore, a deeper understanding of their individual electronic properties, which can be substantially different from those in infinite systems because of the finite-size electronic confinement [228], is needed.

The electronic properties of various graphene nanoribbon structures and the influence of the applied voltage is being studied both for the out-of-plane [229, 230, 231] and for the in-plane [232, 91, 12, 14] field directions. The optical and magnetic properties of the single and multilayer graphene QDs of various shapes have also been studied at zero field [233, 234, 235, 236, 237, 238, 239, 240, 241, 242, 243, 244]. The distinctive property of these QDs is the opening of a finite-size energy gap due to the electron confinement, that is different from the above mentioned field-induced gap since it exists also at $E = 0$. In addition, the novel electronic states localized at the sample boundary are formed [233, 234, 236]. In the energy spectrum these states are located inside the gap in the vicinity of the zero energy. This corresponds to the Dirac point, when size of the system tends to infinity, therefore they are usually referred to as zero energy states (ZES). Unlike the ZES in single layer graphene QDs, the ZES in silicene and bilayer graphene QDs can be easily manipulated by an electric field applied normally to the graphene or silicene layers [245, 246, 247, 248].

In this chapter we explore this functionality for the design of the QD-based optoelectronic devices. We discuss the effect of an electric field on the optical absorption cross section in silicene and bilayer graphene QDs and how the applied field can control the number and intensities of absorption peaks.

In what follows we introduce structure classification and provide details of our tight-binding calculations. We shall present and discuss optical absorption spectra in electric field for a range of QD types and, finally, summarise obtained results.

4.2 Structures and calculation model

Let us use a classification similar to that proposed for single layer graphene QDs [243]. The structures are classified based on their shape and edge type. As can be seen from Fig. 4.1, four types of QD can be distinguished. Depending on their edge geometry, QDs can be classified as the zigzag or armchair QDs that are presented in Fig. 4.1 (a), (b) and (c), (d), correspondingly. A quantum dot of each of these types can have triangular (TRI) or hexagonal (HEX) shape. The number of atoms in the nanocluster varies depending on its shape and size. Table 4.1 summarizes how different size characteristics are connected with the total number of atoms in

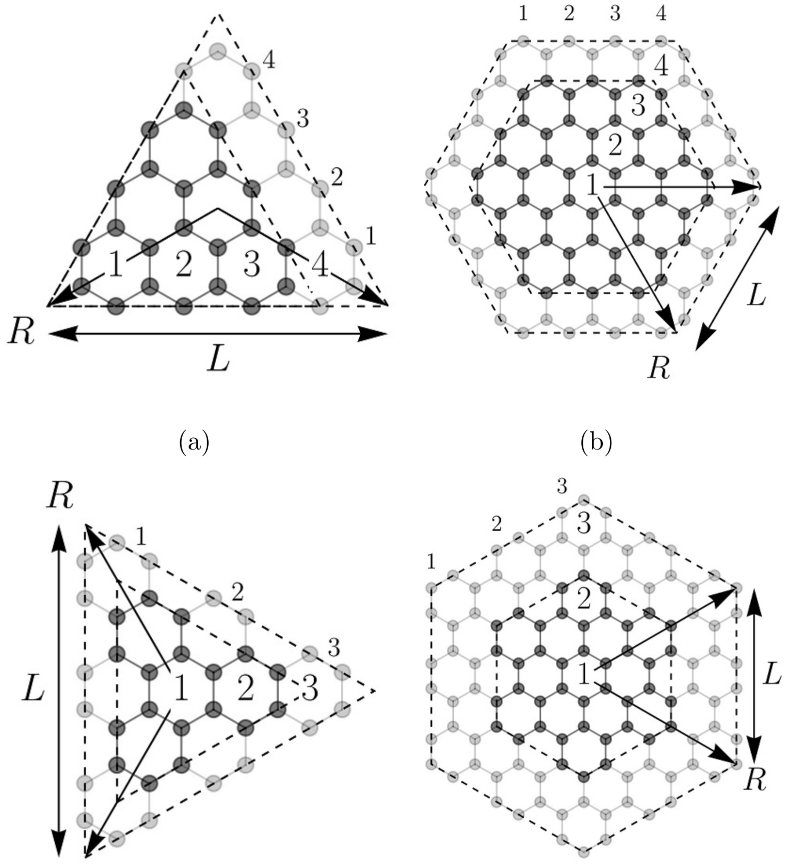

(a) (b)

(c) (d)

Figure 4.1: The four main types of QD, based on the 2D hexagonal lattice: (a) zigzag triangular, (b) zigzag hexagonal, (c) armchair triangular , (d) armchair hexagonal, where R and L are the circumscribed circle radius and edge length, respectively. Quantum dot indexing is presented by larger and smaller font numbering.

the single layer structure, N, by means of the number of characteristic hexagonal elements and the lattice parameter a_0. The choice of a characteristic element for the structure indexing is a matter of convention. As shown in Fig. 4.1 by larger and smaller font numbering, one can count hexagons or, equivalently, edge atoms. In the case of a QD with zigzag edges, shown in Fig. 4.1 (a), (b), edge atoms on a single edge are counted, whereas for QDs with armchair edges, presented in Fig. 4.1 (c), (d), edge atom pairs are counted [249]. The lattice parameter a_0 is the distance between the nearest atoms, or their projections onto a horizontal plane as depicted in Fig. 4.2 (d) and (b) for a flat and low-buckled structure, respectively. Obviously, to obtain the total number of atoms in a bilayer (multilayer) structure the number of atoms in the Table 4.1 should be multiplied by the number of layers.

Table 4.1: Relations between the number of atoms per layer, N, and quantum dot size characteristics: circumscribed circle radius R, edge length L, and the number of edge atoms N_z (or edge atom pairs N_a). The parameter a_0 is the distance between the nearest atoms in 2D hexagonal lattice or their projection onto a horizontal plane in case of the buckled structure (≈ 1.42 Å for graphene and ≈ 2.21 Å for silicene [1]).

	Quantum dot type			
	Zigzag		Armchair	
	triangular	hexagonal	triangular	hexagonal
R	$(N_z+1)\,a_0$	$\sqrt{3}\,(N_z-1/3)\ a_0$	$\sqrt{3}N_a a_0$	$(3N_a-2)\,a_0$
L	$\sqrt{3}\,(N_z+1)\,a_0$ [a]	$\sqrt{3}\,(N_z-1/3)\ a_0$ [a]	$3N_a a_0$	$(3N_a-2)\,a_0$
N	$N_z^2+4N_z+1$ [b]	$6N_z^2$	$3N_a\,(N_a+1)$ [b]	$6\,(3N_a^2-3N_a+1)$
$N_{z,a}$	$\sqrt{N+3}-2$	$\sqrt{\frac{N}{6}}$	$\frac{\sqrt{12N+9}-3}{6}$	$\frac{\sqrt{2N-3}+3}{6}$

[a] Ref. [243]

[b] Ref. [249]

The electronic properties of presented nanoclusters in a transverse electric field

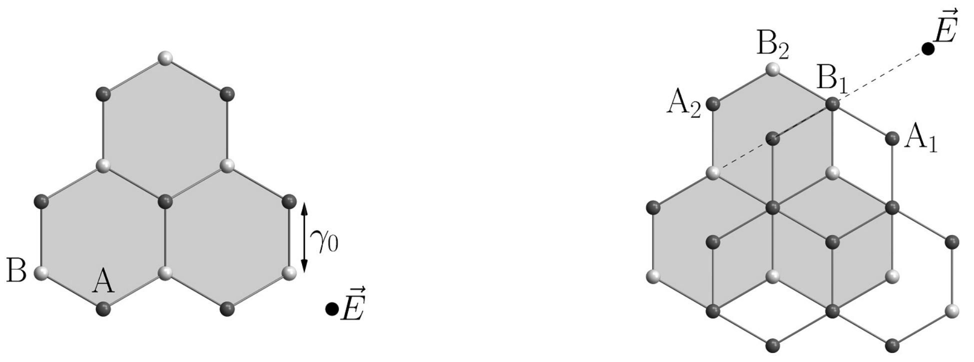

(a) Top view

(b) Top view

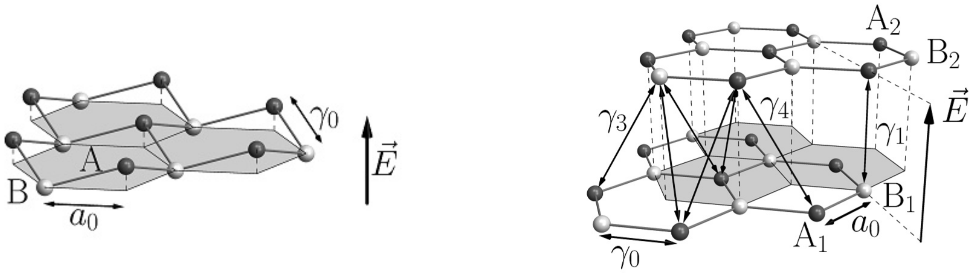

(c) Side view

(d) Side view

Figure 4.2: The structure and tight-binding hopping parameters for silicene (a), (c) and bilayer graphene (b), (d). In each case a black vertical arrow shows the direction of the applied electric field.

can be calculated using the tight-binding Hamiltonian [224, 9, 250],

$$H = \sum_{\langle ij \rangle} t_{ij} c_i^\dagger c_j + \sum_i V_i \left(E \right) c_i^\dagger c_i, \tag{4.1}$$

where $c_i^\dagger$ and c_i are the electron creation and annihilation operators, t_{ij} are the inter-site hopping parameters and V_i is the on-site electron potential that depends both on the local atomic environment and on the applied electric field. The hopping parameters t_{ij} can be written in terms of the nearest-neighbor (NN) coupling constants γ_i, as illustrated in Fig. 4.2. In the case of silicene we use the simplified version appropriate for the low-energy states [250, 9]. According to this approximation there is only one *in-plane* coupling parameter between sites A and

B, $\gamma_0 \simeq 1.6$ eV, that corresponds to the nearest-neighbor hopping between sites A and B.

For graphene this parameter is $\gamma_0 \simeq 3$ eV. The on-site potential, $V_i(E)$ is different for A and B sites and can be presented as $V_i = \xi_i\Delta - \xi_i lE$ where $\xi_i = \pm 1$ for the B and A type of atoms, $\Delta \simeq 3.9$ meV is the effective buckling-gap parameter and lE is the field-induced electrostatic interaction, related to the up/down shift of B and A atoms on $l \simeq 0.22\,\mathring{A}$ with respect to the average plane.

For the bilayer graphene structure, along with the *in-plane* coupling $\gamma_0 \simeq$ 3.16 eV, the *inter-layer* parameters $\gamma_1 \simeq 0.38$ eV, $\gamma_3 \simeq 0.38$eV and $\gamma_4 \simeq -0.14$ eV (see Fig. 4.2 (b)) should be also taken into account. The field-dependent on-site potential can be written [224] as $V_i = \eta_i\Delta - \varsigma_i lE$ where $\eta_i = 0$ for A1 and B2 atoms, $\eta_i = 1$ for A2 and B1 atoms and $\varsigma_i = \pm 1$ for the atoms located in the upper (A2, B2) and lower (A1, B1) layers correspondingly (See Fig. 4.2). The on-site potential due to the different local atomic environments is taken as $\Delta \simeq$ 22meV and the inter-layer distance as $2l \simeq 3.5\,\mathring{A}$.

By numerically diagonalizing the Hamiltonian given by Eq. (4.1) one finds the single-electron wave functions $|\Psi_i\rangle$ and their corresponding energy levels ε_i, which can then be used to evaluate the optical absorption cross section given by the following expression:

$$\sigma(\varepsilon) \sim \sum_{i,f} S(\varepsilon_{i,f})\delta(\varepsilon - \varepsilon_{i,f})\,, \tag{4.2}$$

where $S(\varepsilon_{i,f})$ is the oscillator strength, and $\delta(\varepsilon - \varepsilon_{i,f})$ is the Dirac delta function. The oscillator strength characterizing the rate of transitions between the initial, $|\Psi_i\rangle$, and the final, $|\Psi_f\rangle$, states is defined as [251]

$$S(\varepsilon_{i,f}) \sim \varepsilon_{i,f}\left|\langle\Psi_f\left|\widehat{\boldsymbol{r}}\right|\Psi_i\rangle\right|^2 . \tag{4.3}$$

In Eq. (4.3) $\widehat{\boldsymbol{r}}$ is the position operator and $\varepsilon_{i,f} = \varepsilon_f - \varepsilon_i$ is the energy of a single-electron transition between the states with energies ε_i and ε_f. The summation in Eq. (4.2) is carried out over all possible transitions between the valence and conduction states.

To mimic thermal level broadening, finite single electron excitation lifetimes, nanocluster size inhomogeneity, etc., single electron absorption peaks in Eq. (4.2) are broadened by a Gaussian function with linewidth, α,

$$\sigma(\varepsilon) \sim \sum_{i,f} S(\varepsilon_{i,f}) \exp\left(-\frac{(\varepsilon - \varepsilon_{i,f})^2}{\alpha^2}\right) , \tag{4.4}$$

As follows from Eqs.(4.2) and (4.3), calculation of the absorption spectrum is reduced to a calculation of the matrix elements of the position operator, i.e., $\langle \Psi_f |\hat{\boldsymbol{r}}| \Psi_i \rangle$. Within the tight-binding model in its most general form this physical quantity is given by [252, 253, 254]

$$\begin{aligned} \langle \Psi_i |\hat{\boldsymbol{r}}| \Psi_j \rangle = \sum_{m,\gamma,\gamma'} C^*_{i,m,\gamma} C_{j,m,\gamma'} \boldsymbol{r}_m \delta_{\gamma,\gamma'} \\ + \sum_{m,\gamma,\gamma'} C^*_{i,m,\gamma} C_{j,m,\gamma'} \langle \phi_{m,\gamma} |\hat{\boldsymbol{r}} - \boldsymbol{r}_m| \phi_{m,\gamma'} \rangle , \end{aligned} \tag{4.5}$$

where $\boldsymbol{r}_m$ is the position of the m-th atom in the QD, $\phi_{m,\gamma}$ is the atomic orbital γ of the m-th atom, $C_{i,m,\gamma}$ are the coefficients of the expansion of the electron wavefunction in terms of the atomic orbitals. The first sum in Eq. (4.5) is the dipole moment associated with the positions of the atoms of the QD. Due to the orthogonality of the electron wave functions of any two different states the value of this sum does not depend upon the choice of the origin of the coordinate system. Hence, only the relative atomic positions with respect to each other contribute to this term and, therefore, it is usually referred to as the inter-atomic dipole moment. The second sum of Eq. (4.5) represents the dipole moment of transitions between orbitals γ and γ' located on the same atomic site and it is usually referred to as intra-atomic dipole moment. The intra-atomic dipole moment restores the result for an isolated atom in the limit of non-interacting atoms of the QD. In contrast to this, ZES arise due to the interaction between the atoms. Therefore, the contribution of intra-atomic dipole moments to the resulting dipole moment of transitions between low-energy states is assumed to be small. Taking into account the fact that the low-energy electronic structure of silicene and bilayer graphene QDs is formed by π-atomic orbitals, one can reduce Eq. (4.5) to the following form:

$$\langle \Psi_i |\hat{\boldsymbol{r}}| \Psi_j \rangle = \sum_m C^*_{i,m} C_{j,m} \boldsymbol{r}_m , \tag{4.6}$$

where $C_{i,m}$ are the coefficients of expansion of the electron wavefunction Ψ_i in the basis of the π-orbitals ϕ_m,

$$\Psi_i = \sum_m C_{i,m}\phi_m(\boldsymbol{r} - \boldsymbol{r}_m)\,. \tag{4.7}$$

The unknown coefficients of Eq. (4.7), $C_{i,m}$, are the components of eigenvectors of the Hamiltonian given by Eq. (4.1).

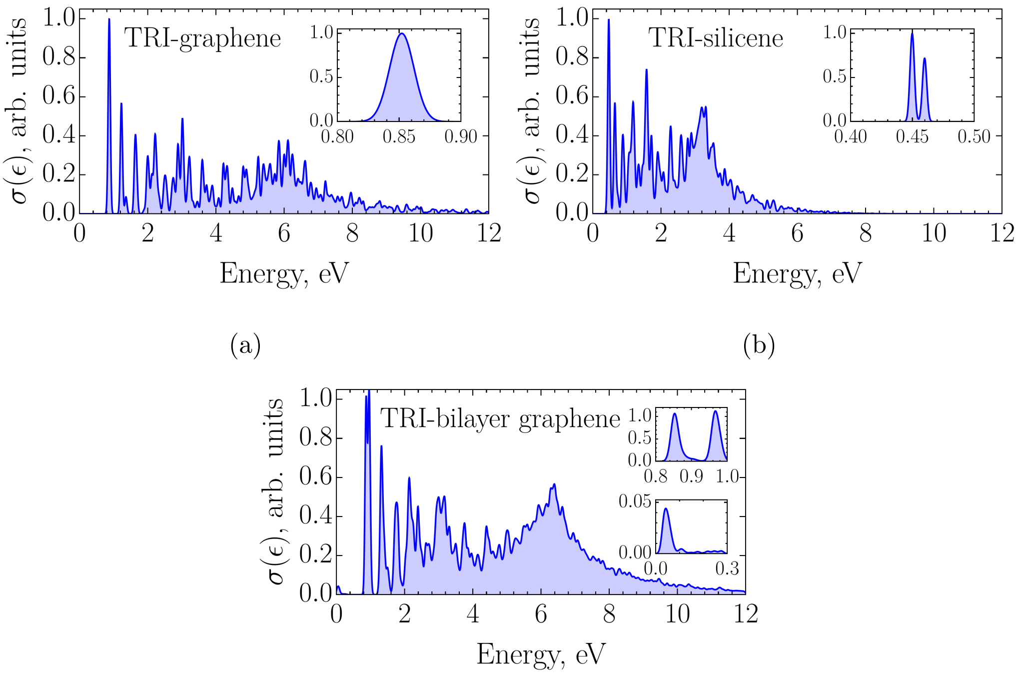

(a)

(b)

(c)

Figure 4.3: Optical absorption cross sections of triangular (TRI) quantum dots with zigzag edges based on (a) graphene, (b) silicene and (c) bilayer graphene. Insets show zoomed in regions of interest. Each nanocluster has 438 atoms per layer.

4.3 Optical absorption of triangular quantum dots

Optical absorption cross sections per atom, $\sigma(\varepsilon)/N$, where N is the total number of atoms, were obtained in arbitrary units for graphene, silicene, and bilayer graphene nanoclusters with 438 atoms per layer ($L \approx 77$ Å for silicene and $L \approx 49$ Å for single layer and bilayer graphene) by the procedure described in Section 4.2. The results are depicted in Fig. 4.3. The number of ZES in the selected triangular nanoclusters is equal to 18 for graphene and silicene QDs, and to 36 in the bilayer graphene QDs. This number can be expressed in terms of the size parameter N_z, specified in Table 4.1, as $N_z - 1$ and it should be multiplied by the number of layers for bilayer quantum dots. In the present calculations and thereafter the optical absorption cross section is a result of transitions from states below to states above the Fermi level. The linewidth for the main panels in Fig. 4.3 was selected to be equal to $\alpha = 45$ meV whereas, for the study of low-energy features (insets in Fig. 4.3), parameter α was selected to be equal to 14 meV for graphene and bilayer graphene, 2.5 meV for silicene QDs.

We consider first transitions at zero electric field. The dependence of the optical absorption cross section for graphene quantum dots on the transition energy is shown in Fig. 4.3 (a). The results are in good agreement with those of Yamamoto et al. [249]. Figure 4.3 (b) presents the corresponding $\sigma(\varepsilon)/N$ for silicene QDs. The low-energy zoom at the inset to this figure reveals the shift of the 0.85 eV graphene peak towards 0.45 eV in silicene as a result of the decrease in the hopping energy. The more important difference, however, is the splitting of this peak in two peaks. This effect is caused by the fact that ZES in silicene are no longer localized at $\varepsilon = 0$ [246] and, therefore, the transition energy from the valence states to the ZES is different from the transition energy from the ZES to the conduction states.

The situation with the low-energy peak changes even more for the case of the triangular bilayer graphene QD where the ZES are smeared into the narrow energy band by the inter-layer electron hopping [246]. This smearing creates the dispersion of the optical absorption peaks in the region $0 - 1.0$ eV as shown in the inset of Fig. 4.3 (c). These peaks correspond to the possible transitions from the dispersed ZES and valance states to the dispersed ZES in the conduction band. Such a feature exists neither in graphene nor in silicene single layers where all the ZES are degenerate.

4.4 Electric field effect and optical absorption

In this section we focus on the influence of the external electric field applied to silicenen and bilayer graphene quantum dots of various shapes and edge terminations. Absorption spectra presented below were obtained with a broadening $\alpha = 20$ meV and zero temperature.

4.4.1 Silicene quantum dots with zigzag edges

Figure 4.4 illustrates the effect of the electric field, E, on the optical absorption (a), (c), (e) and on the energy levels spectrum (b), (d), (f) of triangular silicene QDs. As can be seen from Fig. 4.4 (a), there is only one absorption peak below the energy $\varepsilon = 0.5$ eV when $E = 0$. This peak includes two types of transitions: from the highest occupied energy level (HOEL) to the ZES and from the ZES to the lowest unoccupied energy level (LUEL). In graphene these two types of transitions have the same transition energy but in silicene they are not identical and the energy difference between them, which is zero at $E = 0$, can be tuned by the electric field.

With increasing electric field two remarkable effects occur. Firstly, the two indicated transitions become non-identical, which results in splitting the corresponding peak in two peaks. The first peak lies below $\varepsilon \simeq 0.5$ eV at $E = 1$ V/Å, the first peak in Fig. 4.4 (c), while the second peak is positioned at $\varepsilon \simeq 0.7$ eV. Secondly, ZES become closer to the valence band states. Therefore transitions from some of the valence band states to ZES appear at the energies $\varepsilon < 0.5$ eV. These transitions are represented by the second peak in Fig. 4.4 (c). In the higher field, $E = 2$ V/Å, the energy difference between ZES and valence band states becomes even smaller which results in the appearance of the third peak below $\varepsilon = 0.5$ eV in Fig. 4.4 (c). For an opposite direction of the electric field the behaviour is similar but one should note that the absorption peaks at $\varepsilon \simeq 0.5$ eV are now a result of transitions from ZES to the conduction band states.

Hexagonal silicene QDs have no ZES. Therefore, the effect of the electric field is just in the opening of a tunable energy gap [246]. This is clearly seen in the optical

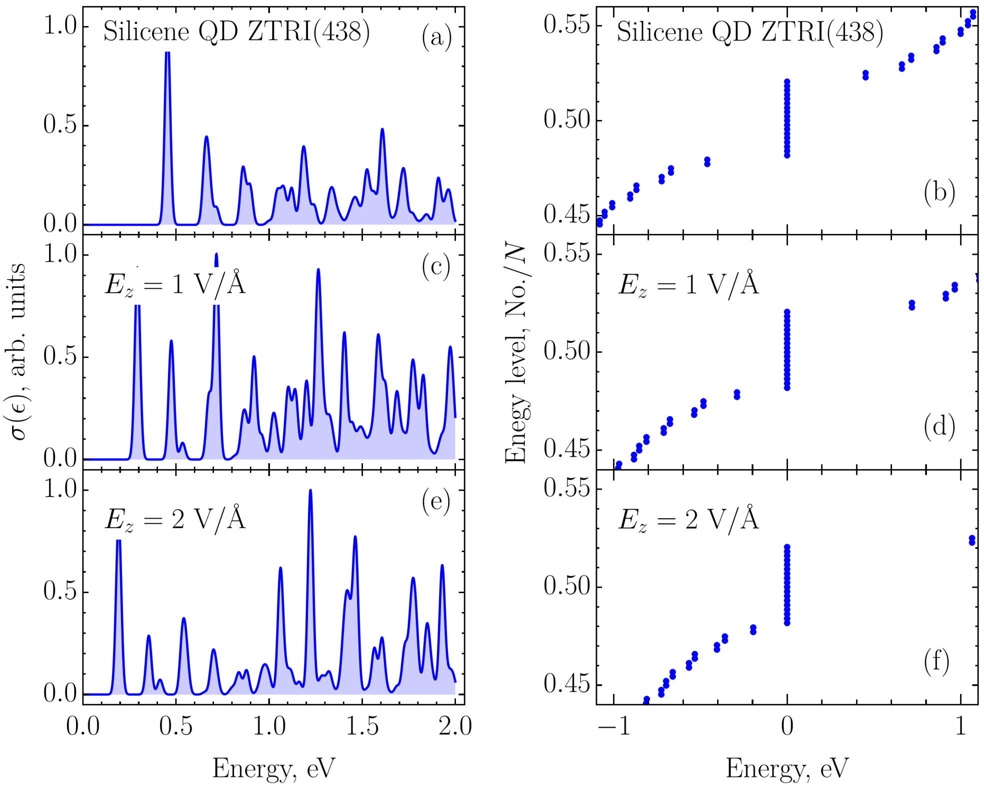

Figure 4.4: Optical absorption cross sections (a), (c), (e) and corresponding energy levels (b), (d), (f) for a triangular zigzag silicene QD consisting of 438 atoms ($L \approx 77$ Å) at different electric fields.

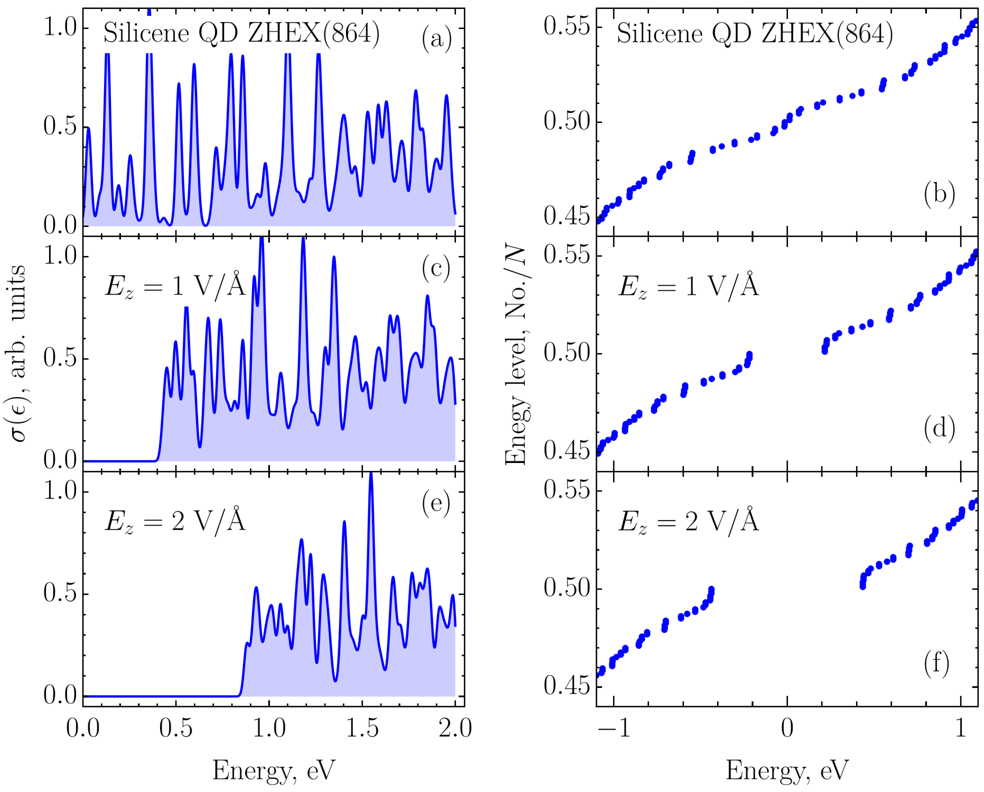

Figure 4.5: The same as Fig. 4.4, but for a hexagonal (HEX) silicene QD containing 864 atoms ($L \approx 45$ Å) at different electric fields.

absorption spectra as a shift of the edge of the absorption in Fig. 4.5 (a), (c), (e). Without the electric field the absorption peaks are distributed almost uniformly in the region of $0-1$ eV. However, application of the field results in their shifting to the higher energies and in the emergence of an energy region with zero absorption. Thus, one can distinguish two regions with zero and non-zero absorption. Note also that the intensity of the peak near the absorption edge depends on the field. The increase of the electric field from 1 to 2 V/Å results in a gentle decrease of the peak.

4.4.2 Silicene quantum dots with armchair edges

In order to present the effect of edge termination on the electronic and optical properties of the silicene we extend our calculations to account for silicene quantum dots with armchair edges. The optical absorption cross sections of triangular and hexagonal silicene QDs with armchair edges are shown in Fig. 4.6. The total numbers of atoms are: $N = 468$ and $N = 762$ atoms ($L \approx 80$ Å and $L \approx 42$ Å) for triangular and hexagonal dots, respectively. At zero electric field, see Fig. 4.6 (a), the absorption spectrum for triangular armchair looks similar to the spectrum of triangular zigzag, see Fig. 4.4 (a), with one absorption peak around $\varepsilon = 0.5$ eV. However, applying an electric field to triangular armchair quantum dots does not shift the absorption edge to the lower energy as in zigzag quantum dots. It is clearly seen in Fig. 4.6 (a), (c), and (e) that the absorption edge blue shifts with the application of an electric field. The reason for such a behaviour is the absence of ZES in armchair silicene quantum dots. The shifting of the ZES in zigzag quantum dots closer to the conduction band or to the valance band decreases the energy gap. Unlike zigzag hexagonal QDs, armchair hexagonal quantum dots at $E = 0$ have a significant energy gap of about 0.3 eV. As indicated by Fig. 4.6 (b), (d), and (f), in an electric field this gap increases similar to that opened by the field in the zigzag quantum dots.

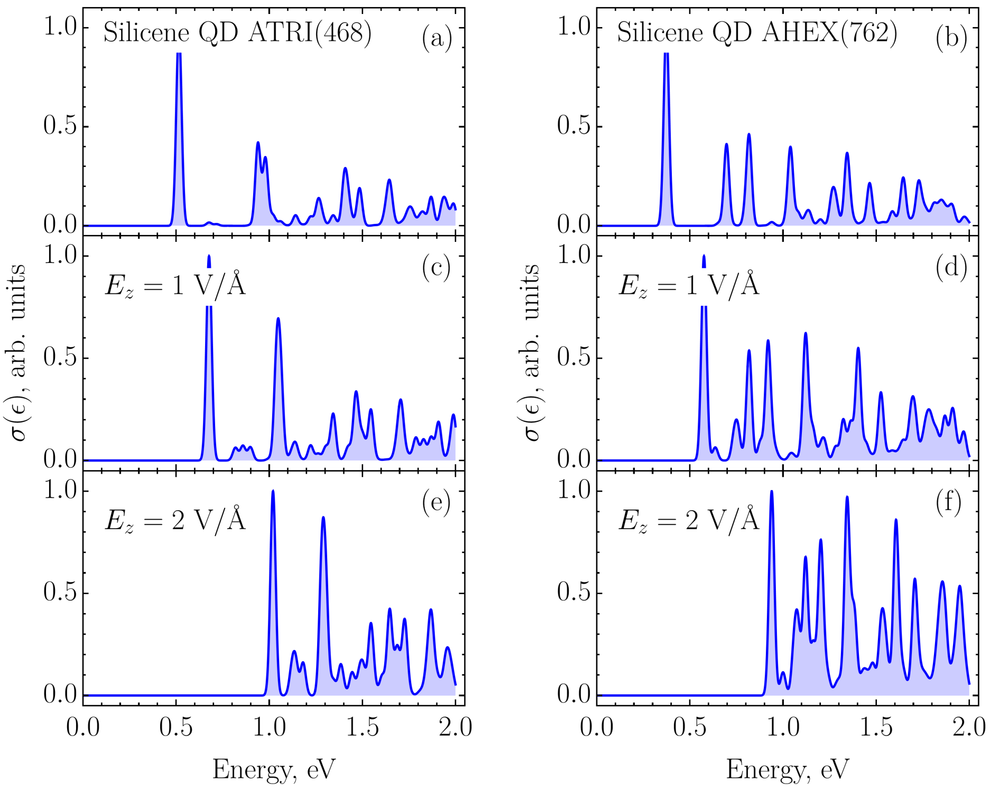

Figure 4.6: Optical absorption spectra for armchair silicene QDs of triangular (a), (c), (e) and hexagonal (b), (d), (f) shapes, consisting of 468 and 762 atoms and having edge length $L \approx 80$ Å and $L \approx 42$ Å, respectively.

4.4.3 Bilayer graphene quantum dots with zigzag edges

In this section we shall consider the quantum dots of triangular and hexagonal shapes based on bilayer graphene with number of atoms per layer $N = 222$ and $N = 216$, respectively. Let us begin with the optical properties of the triangular bilayer graphene QDs, whose energy levels are presented in Fig. 4.7 (b). At zero field, ZES can be divided into two groups. The first group represents ZES located below the Fermi level, $\varepsilon_F = 0$ eV in Fig. 4.7 (b), at $\varepsilon \simeq -0.1$ eV. The second group represents ZES located above the Fermi level at $\varepsilon \simeq 0.1$ eV. Consider next the optical absorption peaks resulting from the transitions between these two groups under the effect of electric field. In general, the smearing of ZES and the application of an electric field affects all optical transitions from and to ZES but we focus here only on the transitions between the two previously discussed groups of ZES. These

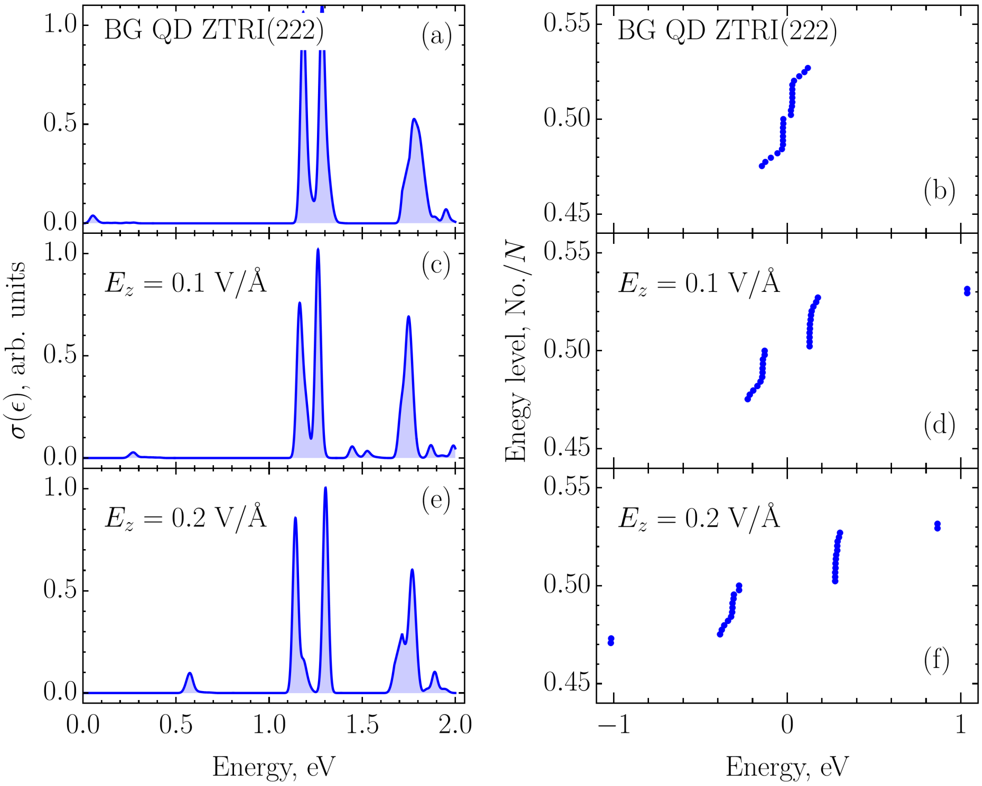

Figure 4.7: Optical absorption spectra (a), (c), (e) and energy levels (b), (d), (f) of a triangular bilayer graphene QD made of 222 atoms per layer ($L \approx 34$ Å) at different electric fields.

transitions can be seen in Fig. 4.7 (a) in the energy range from 0 to 0.3 eV. Thus, we can identify one group of optical transitions within the ZES. Figure 4.7 (a) shows a series of absorption peaks in the energy range from 0 to 0.3 eV. These small intensity peaks represent the above mentioned group of transitions. The application of the electric field increases the tiny energy gap between the two groups of the ZES and gathers the ZES groups into narrower energy ranges. This leads to the up-shift of the set of the low-energy absorption peaks to $\varepsilon \simeq 0.3 - 0.45$ eV for $E = 0.1$ V/Å with the gathering of the small intensity peaks and increase in the peak intensity as can be seen in Fig. 4.7 (c). Increasing the electric field to $E = 0.2$ V/Å results in a further increase in the energy gap which in turn increases the intensity and the up-shift of the absorption peak to $\varepsilon \simeq 0.6$ eV as can be seen in Fig. 4.7 (e).

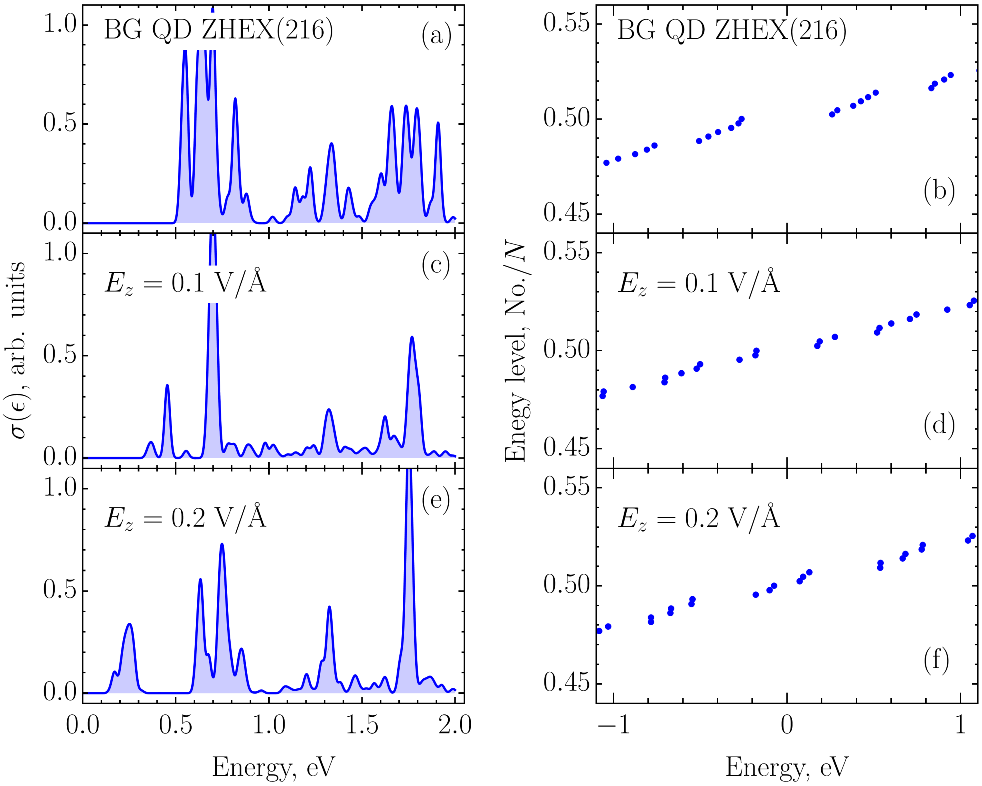

Figure 4.8: The same as Fig. 4.7, but for a hexagonal bilayer graphene QD containing 216 atoms per layer ($L \approx 14$ Å) at different electric fields.

The optical absorption cross section and energy levels for a hexagonal bilayer graphene QD at different values of the electric field are shown in Fig. 4.8 (a), (c), (e) and Fig. 4.8 (b), (d), (f), respectively. In deep contrast to triangular bilayer graphene QDs, the energy gap in hexagonal bilayer graphene between the HOEL and LUEL, which is presented in Fig. 4.8 (b) at $E = 0$ V/Å, decreases with increasing electric field. This results in emergence of the group of the low-energy absorption peaks positioned at $\varepsilon \simeq 0.4$ and 0.2 eV in Fig. 4.8 (c) and (e), respectively. Thus, in small bilayer graphene quantum dots the low-energy absorption peaks exhibit blue/red shift for triangular/hexagonal dot's shape.

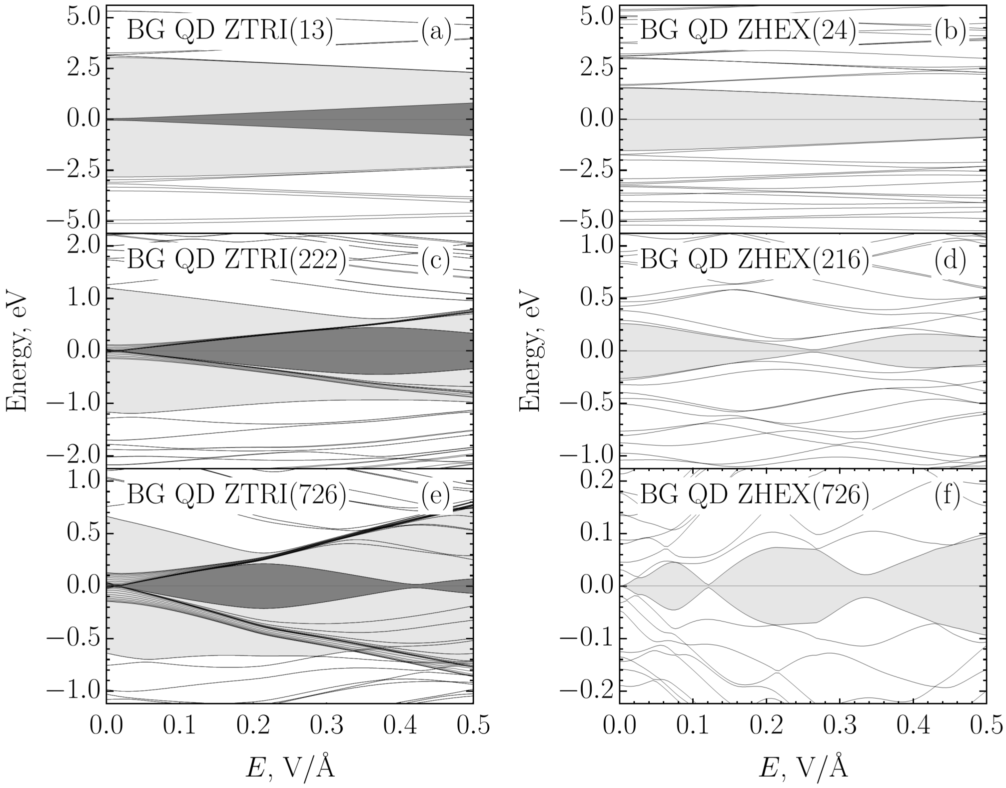

Figure 4.9: the energy level dependence on the applied electric field in triangular (a) $L \approx 7.4$ Å, (c) $L \approx 34$ Å, (e) $L \approx 64$ Å and hexagonal (b) $L \approx 4.1$ Å, (d) $L \approx 14$ Å, (f) $L \approx 26$ Å bilayer graphene QDs.

In order to test this feature for different sizes of triangular and hexagonal bilayer graphene QDs we plotted Fig. 4.9, which shows the dependence of the energy levels on the electric field in quantum dots of different sizes. It can be seen from Fig. 4.9 (b), (d), (f) that the energy gap (light gray) in hexagonal dots decreases with the application of electric field for small dots and starts to increase with the field for a dot size, where the total number of atoms is $N = 726$ per layer. The energy gap for triangular quantum dots increases with the field for all the selected sizes as seen from Fig. 4.9 (a), (c), (e). We can differentiate two energy gaps. The first one is the size-energy gap shown in Fig. 4.9 (a), (c), (e) in light gray and the second is the stacking induced energy gap which occurs between ZES, ZES-energy gap, highlighted in gray. Due to the coupling parameters γ_4 and the on-site potential Δ in bilayer graphene, the ZES states split into two groups giving rise to the ZES-energy gap which is directly proportional to the applied electric field. At the same time the size-energy gap, highlighted in light gray in Fig. 4.9 (a), (c), (e), decreases for an increasing electric field. Similar behaviour is observed for HEX bilayer small QDs in Fig. 4.9 (b), (d). Also, one can notice that for high enough fields the opposite trends can be achieved in all the cases. The critical field value, which such a switch of the trend occurs at, decreases with the increase of the quantum dot size.

4.4.4 Bilayer graphene quantum dots with armchair edges

As discussed above for zigzag bilayer quantum dots, the increase (decrease) in the absorption gap can be obtained by applying an electric field to triangular (hexagonal) bilayer graphene QDs. Bilayer graphene QDs with armchair termination do not support edge states, thus it is expected that armchair triangular and hexagonal bilayer QDs will follow a similar trend to that obtained in hexagonal zigzag QDs. Figure 4.10 illustrates the optical absorption cross section of triangular [Fig. 4.10 (a), (c), (e)] and hexagonal [Fig. 4.10 (b), (d), (f)] bilayer graphene QDs at different values of electric field. We notice that for triangular and hexagonal quantum dots the application of an electric field leads to increase in the number of absorption peak in the energy range $\varepsilon < 1$ eV and a red-shift of the absorption edge.

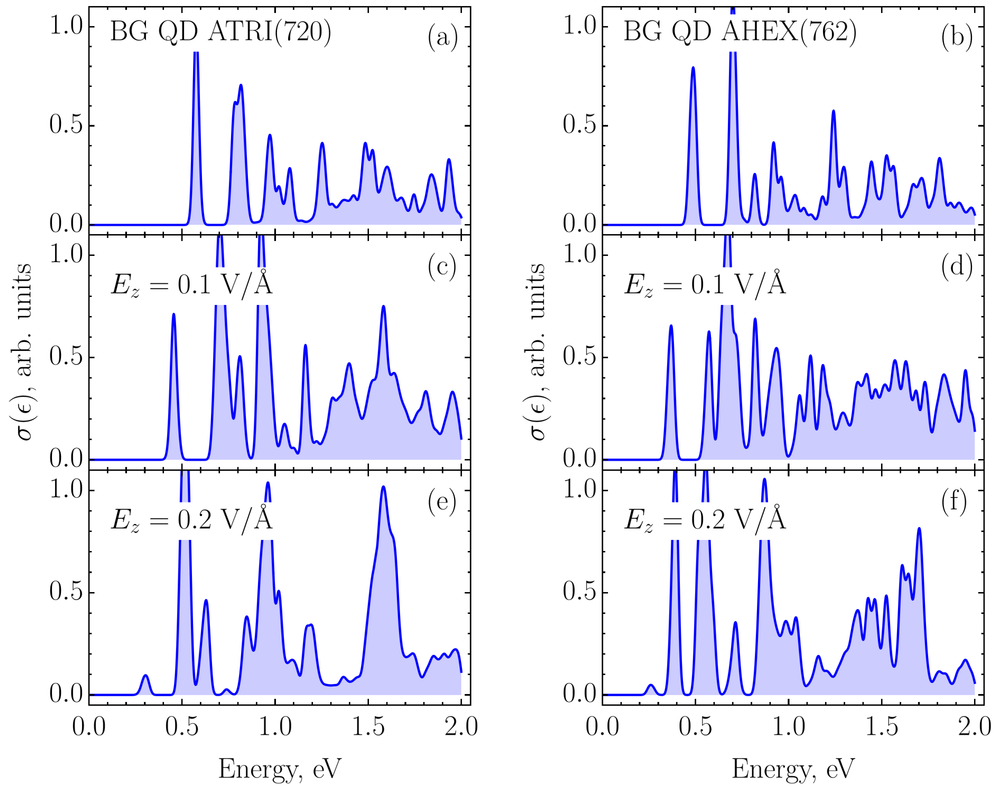

Figure 4.10: Optical absorption spectra for armchair bilayer graphene QDs of triangular (a), (c), (e) and hexagonal (b), (d), (f) shapes with 720 ($L \approx 64$ Å) and 762 ($L \approx 27$ Å) atoms per layer, respectively.

4.5 First principles calculations

Let us briefly compare semi-empirical tight-binding calculations with the first principles ones performed by *Quantum-Espresso* package within the screened hybrid density functional HSE06 for the triangular silicene quantum dot with $N = 33$. These first principles calculations were carried out by Prof. Olivia Pulci on the structures provided by the author of this thesis. The collaborative work took place at the Institute for Nuclear Problems of the Belarusian State University in Minsk (Belarus) within the frame of the EU H2020 RISE project CoExAN (Grant No. H2020-644076). As one can see from Fig. 4.11 (a), in both cases the energy levels follow the same pattern so that the difference between the tight-binding and the density-functional theory (DFT) calculations is only quantitative: the tight-binding energy levels are systematically shifted away from $\varepsilon_F = 0$ eV as compared to the DFT energy levels. The same systematic shift is observed for the absorption spectra in Fig. 4.11 (b). The more important difference, however, is that taking into account the many-body effects results in a splitting of otherwise degenerate zero-energy states leading to emergence of the low-energy absorption peaks and splitting of the high energy ones.

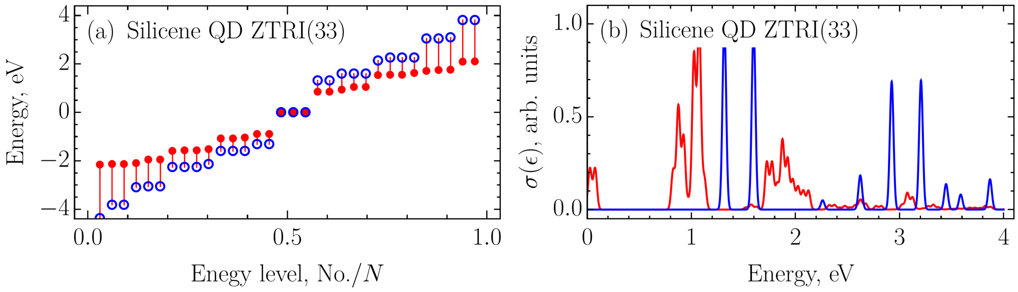

Figure 4.11: The energy levels (a) and optical absorption cross-sections (b) obtained by the DFT (red) and tight-binding (blue) calculations for the triangular silicene quantum dot with zigzag edges and 33 atoms in the structure.

4.6 Conclusions

The optical absorption spectra of silicene and bilayer graphene QDs have been investigated for triangular and hexagonal shapes and compared to the corresponding quantum dots of monolayer graphene. In contrast to triangular graphene quantum dots zero energy states in corresponding silicene dots are positioned slightly asymmetrically with respect to the valence and conduction band states which results in the doubling of the number of the low-energy absorption peaks. Without the electric field, triangular bilayer graphene quantum dots have optical transitions between zero-energy states due to the smearing and splitting of their zero-energy states. These transitions do not exist in graphene or silicene QDs.

The introduction of an electric field into silicene triangular QDs displaces the zero-energy states in the energy gap farther or closer to the conduction band states depending on the direction of the normally applied field. This displacement increases with increasing electric field, thereby increasing the number of absorption peaks in the low-energy region of the optical absorption spectrum. By contrast, hexagonal silicene QDs show a reduction in the number of optical absorption peaks in the low-energy region with increasing electric field in either direction. In triangular bilayer graphene QDs the small energy gap between the zero-energy states increases with increasing electric field. As a result of these field-dependent energy gaps, the edge of absorption due to transitions between zero-energy states undergoes blue shift in response to the applied field. For small quantum dots of hexagonal bilayer graphene, the edge of absorption has a red shift with increasing electric field.

Armchair quantum dots of silicene and bilayer graphene exhibit a significant dependence of their optical properties with electric field. The blue (red) shift of the absorption edge takes place for silicene (bilayer graphene) quantum dots for both hexagonal and triangular shapes. The absence of zero-energy states in armchair quantum dots removes the ability to switch the trend of energy gap dependence on the electric field by changing the shape between triangular and hexagonal. Therefore zero-energy states provide an advantage in silicene and bilayer graphene QDs with zigzag edges over those with armchair edges in controlling the electronic and optical properties using different shapes.

The results of the presented in this chapter should be supplemented in the future by more sophisticated models which take into account electron-electron interaction. For instance, the low-energy absorption of the bilayer quantum dots in conjunction with the magnetic phase transition [245], depending on the value of the applied electric field, is worth special attention since in this case electron-electron interaction may results in emergence of additional low-energy transitions. However, our preliminary checks based on first principles calculations show that the revealed general trends should not change.

The results obtained and discussed in this chapter suggest that optical spectroscopy in an external electric field may be, in principle, a tool for determining the shape and size of the quantum dots of silicene and bilayer graphene. In addition, these results provide the basis for using small silicene and bilayer graphene quantum dots as active elements of mid-infrared optoelectronic devices tunable by an external electric field.

Chapter 5

Electro-optical properties of phosphorene quantum dots

5.1 Introduction

Phosphorene is a single layer of black phosphorous that has been recently isolated [255]. Unlike its predecessor – graphene [2] – it has a significant band gap of about 2 eV. Such a large band gap, in conjuntion with the carrier mobility up to 1000 cm^2 V^{-1} s^{-1}, is anticipated to be more practical, compared to graphene, for digital electronics [256, 257]. However, any new material [258, 259] which is put forward as a candidate to replace current silicon technology will have to catch up with it. In other words, it has to start from the end of Moore's law, to which current technology is rapidly approaching. The critical size limit is predicted to be 5 nm; at this space scale quantum effects such as tunneling and carrier confinement affect device performance [260]. In this view, the effects due to the device's shape and size gain essential importance, thereby making their study in systems with edges such as ribbons and quantum dots a paramount priority. With respect to the optical properties spatial carrier confinement brings not only new challenges but also great advantages such as the decrease of the pumping threshold current in quantum dot lasers [34].

Despite impressive recent achievements in the synthesis of nanostructures, such as the rise of self-assembling molecular engineering [33, 23, 28] and scanning tunneling microscope nanolithography [31, 261], the main problem with low dimensional structures is a precise control of their geometry. Concurrently, techniques with the best outcomes are not easily transferable between materials. Therefore, properties and effects that are robust against disorder are of great importance for practical applications. Here we present the results of our search for universal features in the variety of phosphorene quantum dots.

The first attempts to synthesise phosphorene nanostructures have been undertaken [262, 24, 263] and some theoretical results for regular shapes have been reported [79, 264, 80]. However, the effects of the electric field applied normally to the structure plane and edge disorder have not been investigated yet.

In this chapter we present a systematic comparative study of the electronic and optical properties of phosphorene quantum dots with and without electric field applied in the out-of-plane geometry. We report on the formation of so-called quasi-zero energy states that are highly tunable and optically active. Unlike the previously known zero energy states [233, 237, 243, 239, 241, 250, 246] in silicene and graphene quantum dots they are, to a great extent, insensitive to the dot morphology and edge roughness. The nature of this robustness is in the puckered honeycomb structure of phosphorene, that leads to phosphorous atoms being effectively distributed in two layers but, in contrast to systems such as bilayer graphene, being more strongly bound with a counterpart atom in the opposite layer rather than with neighbouring atoms within the layer. If a phosphorene quantum dot has unpaired atoms in either of the layers then it has edge states positioned in the energy spectrum close to the zero energy. This simple rule also holds true in other phosphorene structures with edges [77, 265] and as such specify the route to the design of the dielectric phosphorene nanoclusters.

In what follows, we introduce structures in Sec. 5.2, provide theoretical details of calculations in Sec. 5.3, discuss the results in Sec. 5.4 and summarize discussion in Sec. 5.5.

5.2 Classification of structures

Phosphorene quantum dots (PQDs) are small crystal clusters of phosphorene. A single dot can be imagined as a piece of phosphorene sheet enclosed within a closed simple, i.e. without self-intersections, polygonal line. In the plane such a line can be a boundary of a variety of polygons. This general approach is useful for many structures, for instance, it can be used to define a unit cell of a superlattice based on any two-dimensional material [12, 14, 13]. In crystals, however, boundaries tend to be formed along directions specific to the crystal structure, therefore not all polygons are suitable for the role of the small cluster boundary. The phosphorene sheet has a puckered honeycomb lattice whose structure restricts the variety of simple bounding polygons to triangles and hexagons. As shown in Fig. 5.1 each of the bounding polygons used as a cutting mask admits isolation of clusters with two different edge geometries. These two species correspond to graphene quantum dots with zigzag and armchair edges [243], therefore, by analogy we refer to them as zigzag and armchair ones. Thus, throughout this chapter we use the following labeling convention for phosphorene quantum dots: ⟨edge type⟩ ⟨shape⟩, where ⟨edge type⟩ is to be either "Z" or "A", meaning zigzag or armchair edge geometry, while ⟨shape⟩ – TRI or HEX means triangular or hexagonal shape.

Table 5.1 summarizes the information on the bounding polygon vertexes in terms of primitive translations of the phosphorene lattice projected onto the plane:

$$\boldsymbol{a}_1 = a(\cos\phi, \sin\phi)\,, \qquad\qquad \boldsymbol{a}_2 = a(\cos\phi, -\sin\phi)\,, \tag{5.1}$$

where $a = |\boldsymbol{a}_1| = |\boldsymbol{a}_2| = 2.537$ Å and $\phi = 40.11^\circ$ is the angle between either of the primitive vectors and Ox-axis. The vertex position $\boldsymbol{v}_i$ can be conveniently expressed as $\boldsymbol{v}_i = s\boldsymbol{\ell}_i$ in terms of the size factor s and the vertex elementary vectors $\boldsymbol{\ell}_i$ given in Table 5.1. Note that to keep a precise correspondence with the graphene quantum dots in the case of the ZTRI quantum dots the three phosphorene atoms closest to the vertexes must be removed from the structure.

The synthesis of such structures by nanolithography or plasma etching inevitably faces a problem of edge roughness, therefore in general the polygon edges

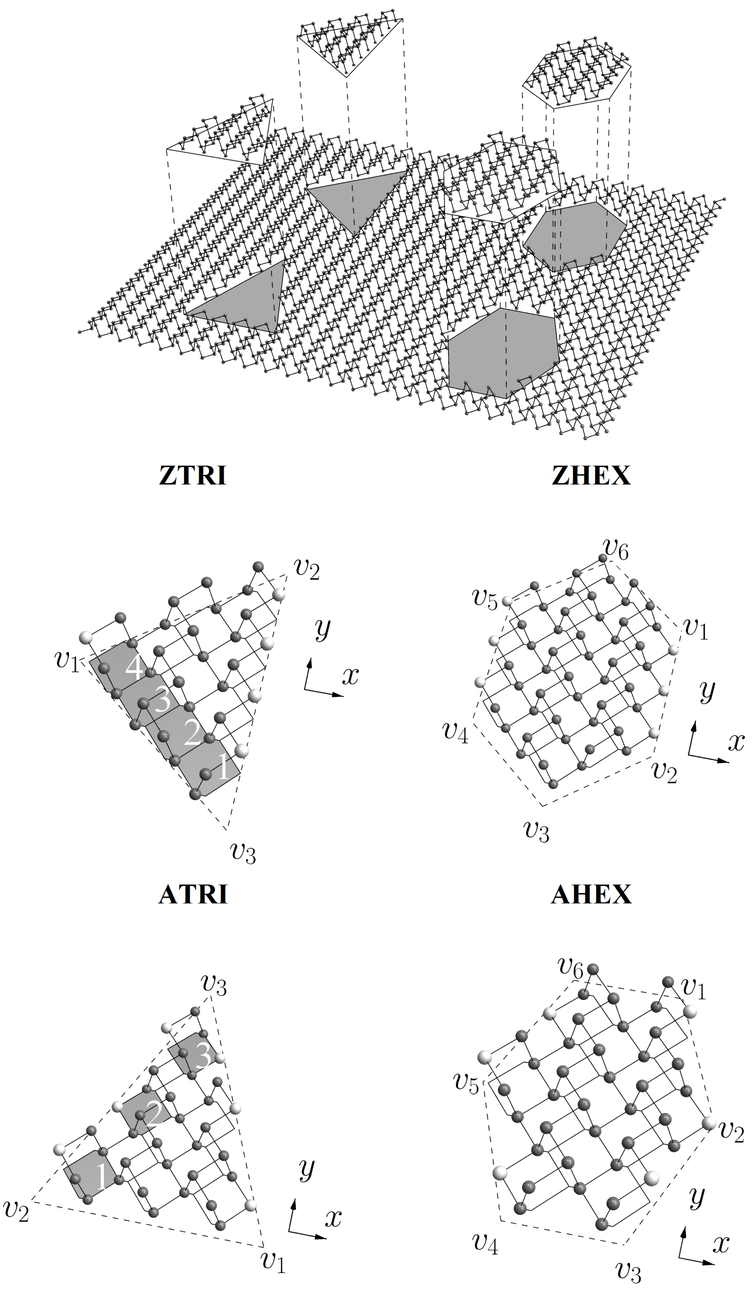

Figure 5.1: Classification of phosphorene quantum dots. Shaded and numbered hexagonal elements are used for unique dot size identification. The phosphorous atoms without "a pair" in the opposite layer are highlighted by a brighter color.

Table 5.1: The vertex elementary vectors $\boldsymbol{\ell}_i = (n, m) = n\boldsymbol{a}_1 + m\boldsymbol{a}_2$ in the basis of the primitive translations $\boldsymbol{a}_1$ and $\boldsymbol{a}_2$ and size factors s for various phosphorene quantum dots.

	Quantum dot type			
$\boldsymbol{\ell}_i$	ZTRI	ZHEX	ATRI	AHEX
1	$(0, 0)$	$(1, 0)$	$(0, 1)$	$(2, -1)$
2	$(1, 0)$	$(0, 1)$	$(-1, 0)$	$(1, 1)$
3	$(0, 1)$	$(-1, 1)$	$(1, -1)$	$(-1, 2)$
4	–	$(-1, 0)$	–	$(-2, 1)$
5	–	$(0, -1)$	–	$(-1, -1)$
6	–	$(1, -1)$	–	$(1, -2)$
s	$N_h + 1$	N_h	$N_h + 1/2$	$N_h - 1/2$

are not regular and possess some degree of disorder. To model this edge roughness we adopt a fractal based approach that in comparison to some other approaches [239, 240] preserves the initial triangular or hexagonal morphology of the dot. Each polygon edge was replaced by a Koch curve [266] generated after 5 iterations with random parameters [267]. The Koch curve is a fractal structure that can be obtained by replacing the central one third of the initial line with a triangular notch and repeating this operation with each newly obtained edge. Thus, the edge roughness is modeled by replacing the bounding polygon with the bounding fractal line as shown in Fig. 5.2.

5.3 Theoretical model

In general the matrix form of the Hamiltonian is obtained by expanding electron wave functions in an orthogonal basis set and calculating the matrix elements of the Hamiltonian operator between the basis functions. The Hamiltonian, then, is

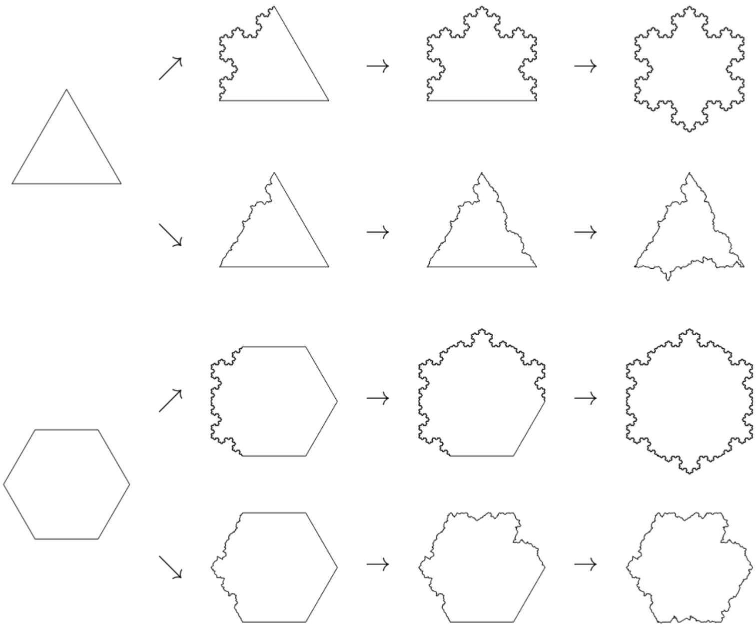

Figure 5.2: The replacement of a polygon edge with the ideal and random Koch curve shown for the regular triangle and hexagon.

an $N \times N$ matrix

$$H = \begin{pmatrix} h_1 & h_{12} & h_{13} & h_{14} & \cdots & h_{1N} \\ h_{21} & h_2 & h_{23} & h_{24} & \cdots & h_{2N} \\ h_{31} & h_{32} & h_3 & h_{43} & \cdots & h_{3N} \\ h_{41} & h_{42} & h_{43} & h_4 & \cdots & h_{4N} \\ \vdots & & & & & \vdots \\ h_{N1} & \cdots & \cdots & \cdots & \cdots & h_N \end{pmatrix}, \tag{5.2}$$

where n is the number of functions in the basis set. Within the single orbital tight-binding model the basis functions are atomic p-orbitals. Thus, the matrix element $h_{ij} = \int_V \psi_i \widehat{H} \psi_j d^3\boldsymbol{r}$, with basis functions ψ_i, is referred to as the hopping integral between the i-th and j-th atomic sites. The hoping integral $h_{ii} = h_i$ is usually referred to as the on-site energy. It has been shown that for correct description of the low-energy electronic properties of phosphorene within the tight-binding model it is sufficient to account for only a few nearest-neighbour hopping integrals and to neglect the overlap integrals [10]. If the distance between the i-th and j-th atoms is one of d_i presented in Table 5.2 then h_{ij} in matrix (5.2) is taken to be equal to the corresponding coupling parameter t_i presented in the first column of Table 5.2 and depicted in Fig. 5.3. If the distance between the corresponding atoms does not match any of d_i then we set $h_{ij} = 0$. The on-site energies are taken to be zero; $h_i = 0$.

Table 5.2: The tight-binding, t_i, and structural, d_i, parameters used for phosphorene based quantum dots.

No.	t_i [a], eV	d_i [b], Å
1	-1.220	2.164
2	3.665	2.207
3	-0.205	2.956
4	-0.105	3.322
5	-0.055	3.985

[a] Ref. [10]

[b] Obtained from Ref. [255]

Applying a static electric field to the considered system adds the following potential to the on-site energy:

$$U = e\boldsymbol{E} \cdot \boldsymbol{r}\,, \tag{5.3}$$

where $\boldsymbol{E}$ is the electric field strength and $\boldsymbol{r}$ is the radius-vector of the given atomic site. For the electric field applied perpendicular to the flat structure parallel to the xOy plane the on-site energy is defined as

$$h_j = \int_V \psi_i \widehat{U} \psi_i d^3\boldsymbol{r} = eEz_j\,. \tag{5.4}$$

For the phosphorene quantum dots in question $z_j = d_2 \cos(\varphi - \pi/2)$, where $\varphi = 103.69°$, for atoms in the upper plane and it is zero for atoms in the lower plane.

The study of optical properties of a finite system requires evaluating of the matrix elements of dipole moment or position operator. These matrix elements are conventionally referred to as optical matrix elements. To calculate optical

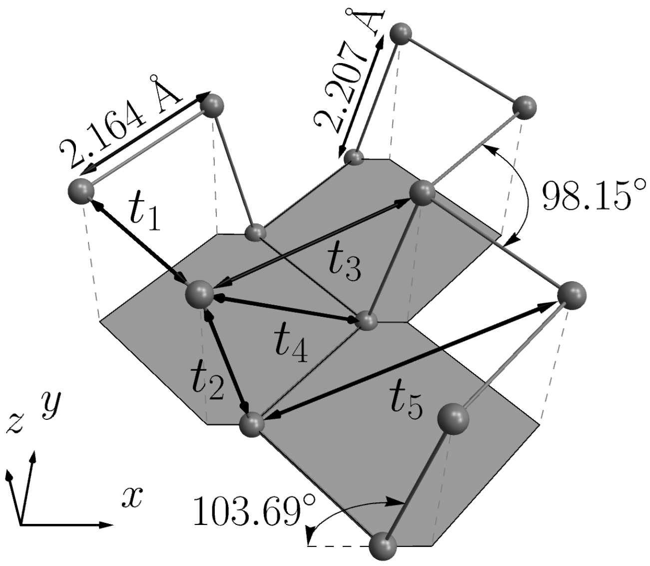

Figure 5.3: The tight-binding and structural parameters of the phosphorene lattice.

matrix elements we present the electric field of the incident electromagnetic wave as $\boldsymbol{E} = E\,\boldsymbol{e}_p$, where E is the magnitude of the electric field and $\boldsymbol{e}_p$ is a unit vector specifying the polarization of the incident wave. In what follows we consider a linearly polarized optical excitation propagating normally to the xOy plane, but our results can be easily generalized for an arbitrary incident angle and polarization. Then $\boldsymbol{e}_p$ is a constant vector and without losing generality it can be chosen to be along the Ox-axis, i.e. $\boldsymbol{e}_p = (1, 0)$. In this way the position operator $\boldsymbol{r}$ is reduced to its projection onto the plane wave polarization vector, which for the given case is just the x coordinate.

Next we have to convert the x coordinate matrix element,

$$x_{lm} = \int_V \Psi_l^*\, x\, \Psi_m\, d^3\boldsymbol{r}\,, \tag{5.5}$$

to that of the tight-binding model. For this purpose we expand the electron wave function Ψ_i over a set of functions $\{\psi_j\}_{j=1\ldots N}$ forming a complete orthonormal basis:

$$\Psi_i = \sum_{j=1}^{N} c_{ij}\,\psi_j\,. \tag{5.6}$$

Substituting this expansion into Eq. (5.5) yields

$$x_{lm} = \sum_{i,j} c_{lj}^{*} c_{mi} \int_V \psi_j^{*}\, x\, \psi_i\, d^3\boldsymbol{r}\,. \tag{5.7}$$

Within the orthogonal nearest-neighbor tight-binding approximation

$$\int_V \psi_j^{*}\, x\, \psi_i\, d^3\boldsymbol{r} = x_i \delta_{ij} = X_{ij} \tag{5.8}$$

or equivalently the matrix form of the x coordinate operator in the tight-binding model is

$$X = \begin{pmatrix} x_1 & 0 & 0 & 0 & \cdots & 0 \\ 0 & x_2 & 0 & 0 & \cdots & 0 \\ 0 & 0 & x_3 & 0 & \cdots & 0 \\ 0 & 0 & 0 & x_4 & \cdots & 0 \\ \vdots & & & & & \vdots \\ 0 & \cdots & \cdots & \cdots & \cdots & x_N \end{pmatrix}, \tag{5.9}$$

where x_i are the x-coordinates of the atomic positions in the structure. In fact, the coefficients, c_{mi}, introduced in Eq. (5.6) are the components of the eigenvectors $\widetilde{C}_m$ of the matrix Hamiltonian given by Eq. (5.2). Thus, the matrix form of Eq. (5.7) is

$$x_{lm} = \widetilde{C}_l^{\dagger} X \widetilde{C}_m = \sum_{j=1}^{N} c_{lj}^{*} c_{mj} x_j\,, \tag{5.10}$$

where "†" denotes the Hermitian conjugate.

Utilizing the matrix elements given by Eq. (5.10), we calculate the oscillator strength of a dipole oscillator [268] as

$$S_x(\varepsilon_{i,f}) = \frac{2m}{\hbar^2} \left| x_{if} \right|^2 \varepsilon_{i,f}\,, \tag{5.11}$$

where m is the free electron mass, $\varepsilon_{i,f} = \varepsilon_f - \varepsilon_i$ is the energy of a single-electron transition between the initial and final states with energies ε_i and ε_f, respectively. The knowledge of the oscillator strength allows one to calculate the optical absorption cross-section [251, 249]:

$$\sigma_x(\varepsilon) \sim \sum_{i,f} S_x(\varepsilon_{i,f}) \delta(\varepsilon - \varepsilon_{i,f})\,, \tag{5.12}$$

where summation is carried out over all possible transitions between the valence and conduction states; $\delta(\varepsilon - \varepsilon_{i,f})$ is the Dirac delta-function. The losses due to scattering on phonons, inhomogenuities etc. can be taken into account phenomenologically by replacing the Dirac delta-function by a Gaussian with a broadening parameter α:

$$\sigma_x(\varepsilon) \sim \sum_{i,f} S(\varepsilon_{i,f}) \exp\left[-\frac{(\varepsilon - \varepsilon_{i,f})^2}{\alpha^2}\right] . \tag{5.13}$$

5.4 Results and discussion

The calculations are carried out for zigzag triangular (ZTRI), zigzag hexagonal (ZHEX), armchair triangular (ATRI), and armchair hexagonal (AHEX) quantum dots (QDs). For the model study we choose ZTRI, ZHEX, ATRI and AHEX phosphorene QDs with N = 222, 384, 216 and 366, characterized by the edge length $L = |\boldsymbol{v}_2 - \boldsymbol{v}_1| \approx 35.5$ Å, 26.2 Å, 33 Å and 23.7 Å, respectively.

5.4.1 Energy spectra

We start with the comparison of the phosphorene quantum dots' (PQDs) energy levels with those of graphene quantum dots (GQDs) as presented in Fig. 5.4. A peculiar group of energy states is observed in the low-energy (close to $\varepsilon = 0$ eV) part of the spectrum in all the selected nanocluster shapes. These states do not exist in most of their counterparts – graphene quantum dots. As one can see, they completely modify the electronic properties of PQDs compared to GQDs. For instance, the group of states in ATRI phosphorene QDs totally fills the energy gap, providing conducting armchair phosphorene QDs (Fig. 5.4 (c)) in contrast to ATRI graphene QDs, where the energy gap ensures the semiconducting behaviour. The states dispersed near the Fermi level of an undoped dot, i.e. $\varepsilon_F = 0$ eV, are localized at the structure edges. In what follows we refer to these edge states in PQDs as quasi-zero energy states (QZES) and denote the number of such states by N_{QZES}. From Figure 5.4 (a) we see that there are 12 ZES in GQD with $n = 222$ and there are 14 edge states smeared asymmetrically around the Fermi level in the

PQD.

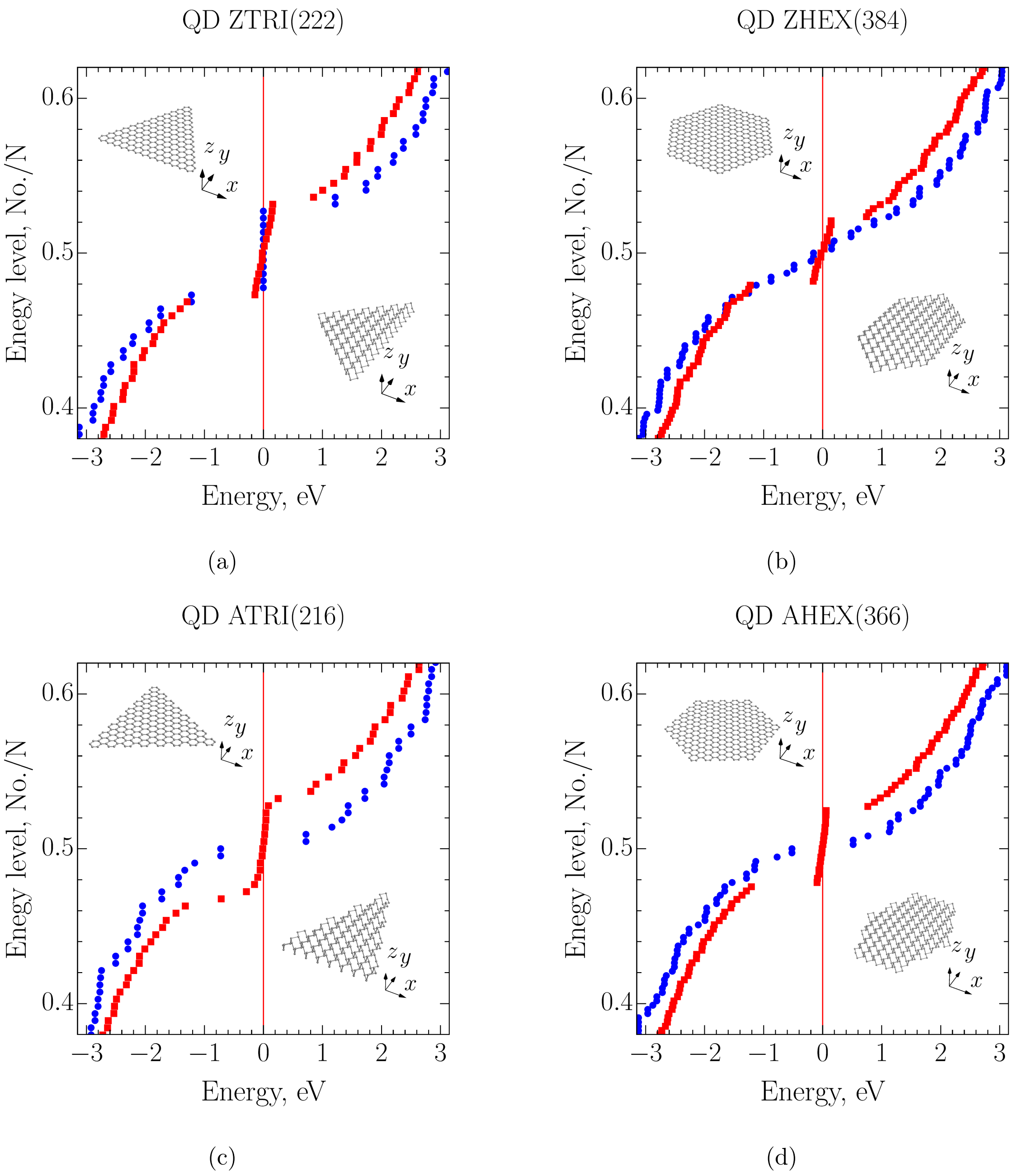

(a) (b) (c) (d)

Figure 5.4: Energy levels of phosphorene QDs (red squares) versus graphene QDs (blue filled circles) for triangular and hexagonal shapes with both zigzag and armchair termination.

The origin of the QZES in ZTRI PQDs can be found by setting the coupling parameters $t_3 = t_4 = t_5 = 0$ and varying t_2 with respect to t_1 [269, 270, 77]. Obviously, when $t_1 = t_2$, the total number of edge states (ZES and QZES) is equal for graphene and phosphorene ZTRI QDs. At $t_1 = -1.22$ eV and $t_2 = 2$ eV, the number of ZES is still the same as in graphene but the conduction and valance states in PQD move towards the ZES. With the continuous increase of t_2, the two energy states, one from the valence band and the other from conduction band, become well separated from their bands and move towards ZES which decreases the energy gaps between ZES and valence and conduction bands. As t_2 increases to 3.665 eV [10] the number of edge states increases to 14 states symmetrically separated from conduction and valence by $\varepsilon_g \simeq 1.5$ eV. We found that independently of the quantum dot size it is always two state that split-off from the bulk states. Adding t_3 and t_5 decreases the energy gap between the edge states and bulk states from 1.5 eV to 1.2 eV with no change to the distribution of the QZES.

In Figure 5.4 (b), the energy levels of the hexagonal graphene QD with zigzag termination and $N = 384$ are compared with those of the corresponding phosphorene QD. We note that for this small size ($N = 384$) the ZHEX graphene QD has no edge states, whereas for the same size ZHEX phosphorene QD there are 16 edge states smeared around the Fermi energy. To investigate the origin of QZES in hexagonal zigzag phosphorene we apply the same strategy as used in triangular phosphorene quantum dots. At $t_1 = t_2$ it has the same energy spectrum as for hexagonal graphene quantum dots. However, at $t_2 = 2$ eV a new set of energy states (16 energy levels for $N = 384$ atoms) fills the energy gap. Increasing t_2 to 3.665 eV leads to gathering of the 16 states with a very small dispersion forming edge states isolated from the bulk bands by $\varepsilon \simeq 1.4$ eV. The effect of t_3 and t_5 is the same as in triangular quantum dots, i.e. the decreasing of the energy gap between edge states and bulk states. Introducing $t_4 = -0.105$ eV generates the antisymmetric displacement of the edge states with respect to the bulk states and a small increase in their dispersion. The number of new edge states, N_{QZES}, in ZHEX-phosphorene dots increases with the dot size. It is given by $N_{\text{QZES}} = 2N_h$, where N_h is the number of hexagons at the edge.

Figure 5.4 (c) shows a comparison between the energy levels of armchair triangular quantum dots of graphene and phosphorene with $N = 216$. In the ATRI graphene QD there is a noticeable energy gap $\varepsilon_g \simeq 1.3$ eV due to the size effect, while in the ATRI phosphorene QD the energy gap disappears. QZES in triangular armchair phosphorene QDs are dispersed inside the energy gap (Fig. 5.4 (c) red squares) giving rise to a quantum dot with zero energy gap. The total number of edge states is $2N_h$, similar to the case of ZHEX phosphorene QDs. Figure 5.4 (d) compares the QZES in hexagonal armchair phosphorene QDs to hexagonal graphene QDs with $N = 366$. The total number of QZES in an AHEX phosphorene quantum dot is $N_{\text{QZES}} = 2(2N_h - 1)$. Thus, we conclude that the origin of QZES is the distribution of the phosphorene atoms in two layers and $t_2 > t_1$. Table 5.3 summarizes the relations between the number of QZES, N_{QZES}, and the structure size for various types of phosphorene QDs. A general rule valid for all

Table 5.3: The number of quasi-zero energy states as a function of the quantum dot size for various dot shapes. $N_{\text{QZES}} = |N_2 - N_1|$, where $N_{1,2}$ are the total number of atoms in the top and bottom layers of the phosphorene dot, respectively. N_h is the number of hexagonal elements at the edge as shown in Fig. 5.1.

	Quantum dot type			
	ZTRI	ZHEX	ATRI	AHEX
N_{QZES}	$N_h + 1$	$2N_h$	$2N_h$	$2(2N_h - 1)$
N_h	$\sqrt{N+3} - 2$	$\sqrt{\frac{N}{6}}$	$\frac{\sqrt{12N+9} - 3}{6}$	$\frac{\sqrt{2N-3} + 3}{6}$

PQD types can be formulated as follows: the number of QZES is equal to the total number of atoms, which are not connected to nearest neighbour atoms by t_2.

5.4.2 Electric field effect

Let us discuss the effect of an electric field applied normally to the structure plane on optical absorption of triangular and hexagonal phosphorene QDs with zigzag and armchair terminations. As in Section 5.4.1, we choose the electric field strength used in Ref. [265], $E = 0.4$ V/Å, as the upper limit and supplement the obtained results with calculations for $E = 0.2$ V/Å. Throughout this chapter the quantum dot orientation with respect to the coordinate system is fixed to be as presented in Fig. 5.1, Gaussian broadening $\alpha = 0.02$ eV, and temperature $T = 0$ K. In the case of graphene it was found that σ_x and σ_y are almost the same, whereas $\sigma_z = 0$ [249]. In contrast, the absorption cross-sections due to x- and y-polarizations are considerably different in phosphorene QDs. Optical absorption due to a z-polarized incident wave is very small compared to that of x- or y-polarizations; thus, it is neglected in the discussion.

Zigzag edges

Optical absorption cross-sections of ZTRI phosphorene QDs for different values of the electric field are shown in Fig. 5.5. It is seen from Fig. 5.5 (b), (d) that the electric field increases the QZES dispersion and shifts QZES and conduction band states towards each other. As can be seen from Fig. 5.5 (f), at $E > 0.2$ V/Å only one QZES moves towards the valance band while the rest of them shifts towards conduction bands. In order to discuss the effect of shifting QZES and conduction band states towards each other on the optical transitions, let us consider the three intense peaks around $\varepsilon = 1$ eV, at $E = 0$ V/Å in Fig. 5.5 (a). These peaks are due to transitions from the HOEL to the group of QZES above the Fermi level (peak at $\varepsilon \approx 1.2$ eV) and from the QZES below the Fermi level to the LUEL (peaks at $\varepsilon \approx 0.8$ eV and $\varepsilon \approx 1$ eV). At $E = 0.4$ V/Å the optical transition at $\varepsilon \approx 1.2$ eV disappears from the low energy absorption and shifts towards higher energies, the positions of the other two peaks at $\varepsilon \approx 0.8$ eV and 1 eV stay almost the same as shown in Fig 5.5 (e). Such a behaviour suggests that the transitions occur from the bottom of the QZES band so that the increase of the QZES dispersion eliminates the effect of the approaching of the conduction bands states towards the QZES as a group.

It can be seen from Fig. 5.5 (a), (c), and (e) that with increasing field there is a noticeable decrease in the intensities of absorption peaks at $\varepsilon > 0.8$ eV compared to the prominent low-energy y-polarized peak. This can be attributed to the decrease of transition matrix elements because the positions of the peaks stay nearly the

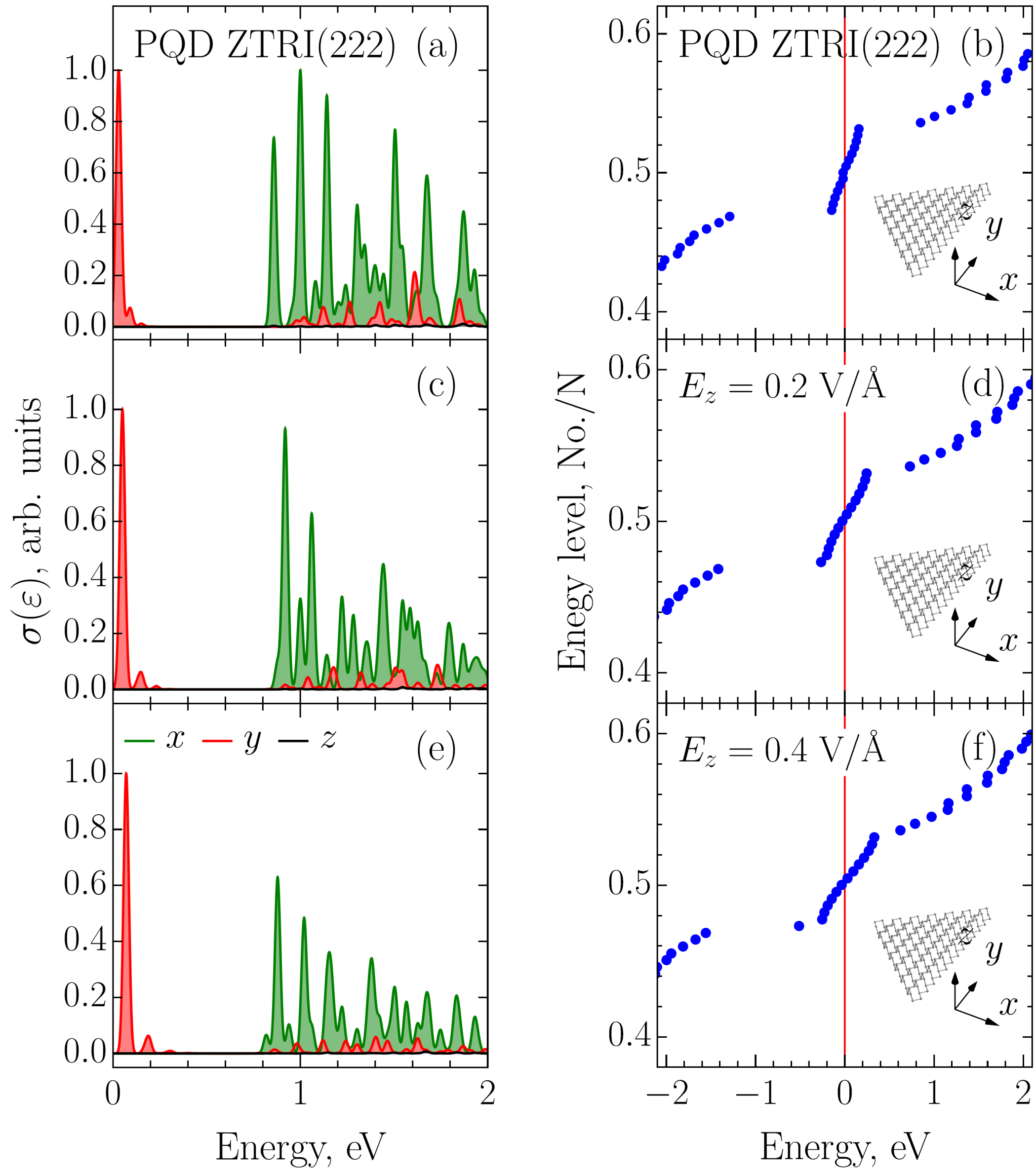

Figure 5.5: The effect of a perpendicular electric field on the optical absorption cross-section (a), (c), (e) and the corresponding energy levels (b), (d), (f) of zigzag triangular phosphorene QDs.

same. It is aslo worth noting that the red absorption peak for an incident y-polarized electromagnetic wave at $\varepsilon \simeq 0.05$ eV, (Fig. 5.6 (a)), experiences a blue shift with increasing electric field which can be attributed to the increased smearing of the QZES as a function of the applied field.

The absorption cross-section of hexagonal zigzag phosphorene QDs in Fig. 5.6 shows a totally different behavior under the influence of electric field. The strong absorption peak, see Fig 5.6 (a), around $\varepsilon = 0.9$ eV occurs due to transitions from the group of edge states to the LUEL. At $E = 0.2$ V/Å the intensity of this peak decreases and vanishes at $E = 0.4$ V/Å, as can be seen in Fig. 5.6 (c) and 5.6 (e). The red absorption peak at $\varepsilon \approx 0.05$ eV, corresponding to an upper edge of the highly topical terahertz frequency range, shown in Fig. 5.6 (a) experiences a decrease in intensity at $E = 0.2$ V/Å and disappears at $E = 0.4$ V/Å. This effect results from the energy gap opening between QZES shown in Fig. 5.6 (f).

Armchair edges

Let us next consider the energy levels and absorption cross-sections of triangular (Fig. 5.7) and hexagonal (Fig. 5.8) phosphorene quantum dots with armchair edges under the effect of an electric field applied perpendicular to the structure plane: $N = 216$ for the triangular and $N = 366$ for the hexagonal case.

Figure 5.7 (b), (d), and (f) shows that the ATRI edge states split into two groups with an energy gap between them that increases with increasing the applied electric field. The result of this new energy gap is a blue shift in the edge of the optical absorption cross-section, as shown in Fig. 5.7 (a), (c), and (e). Moreover, the absorption peaks due to transitions between edge states with a photon energies ε ranging from 0 to 0.5 eV shown in Fig. 5.7 (a), have a comparable intensity with the peaks corresponding to the transitions from edge states to conduction (valance) band states. These transitions between edge states are very weak in bilayer graphene QDs [92]. By increasing the electric field these transitions shift to a higher energy due to the opening of energy gap, Fig. 5.7 (d), (f), and the number of transition peaks decreases as a result of the reduction in smearing of the edge

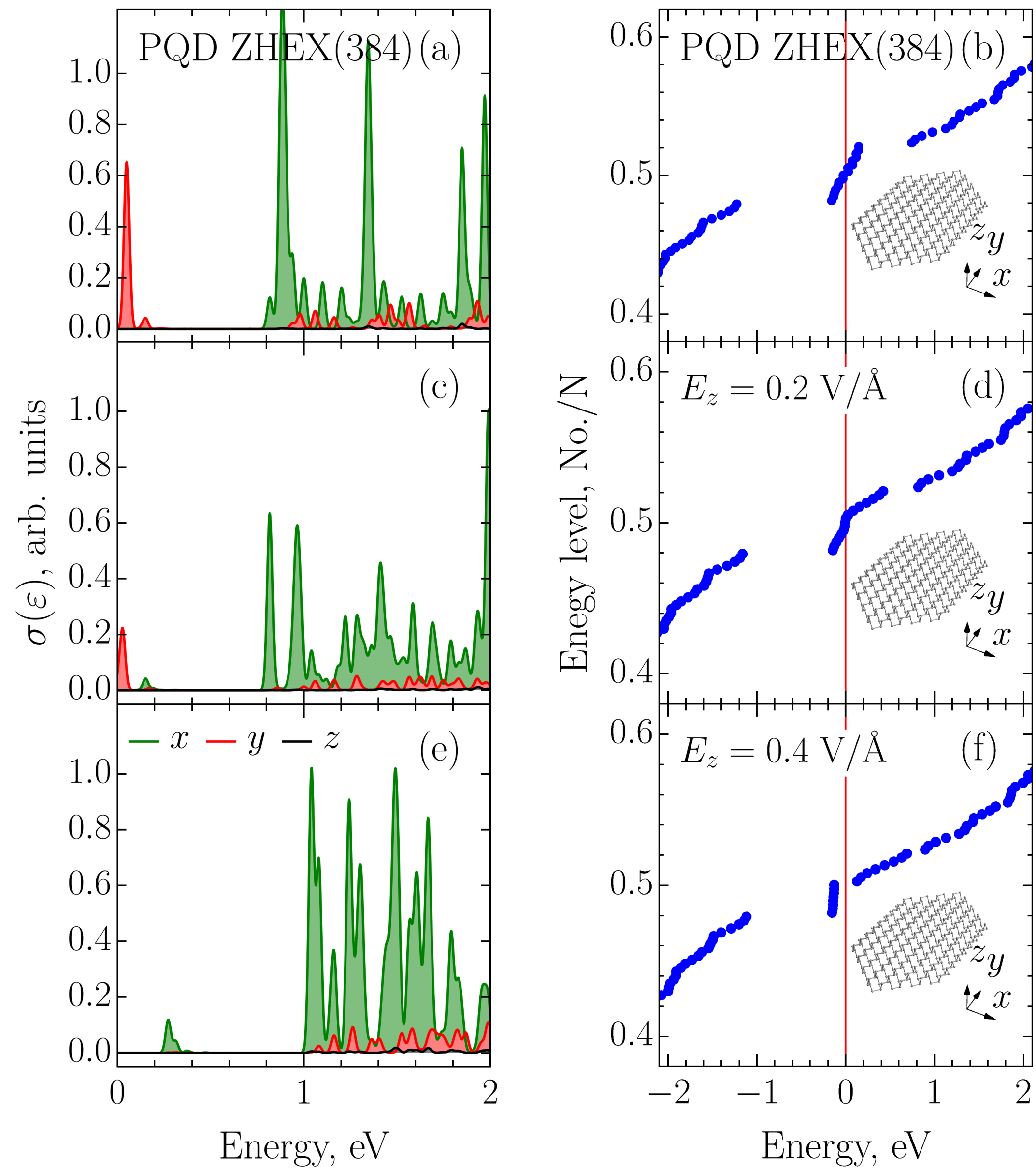

Figure 5.6: The optical absorption cross-section (a), (c), (e) and energy levels (b), (d), (f) of zigzag hexagonal phosphorene QDs at different values of electric field.

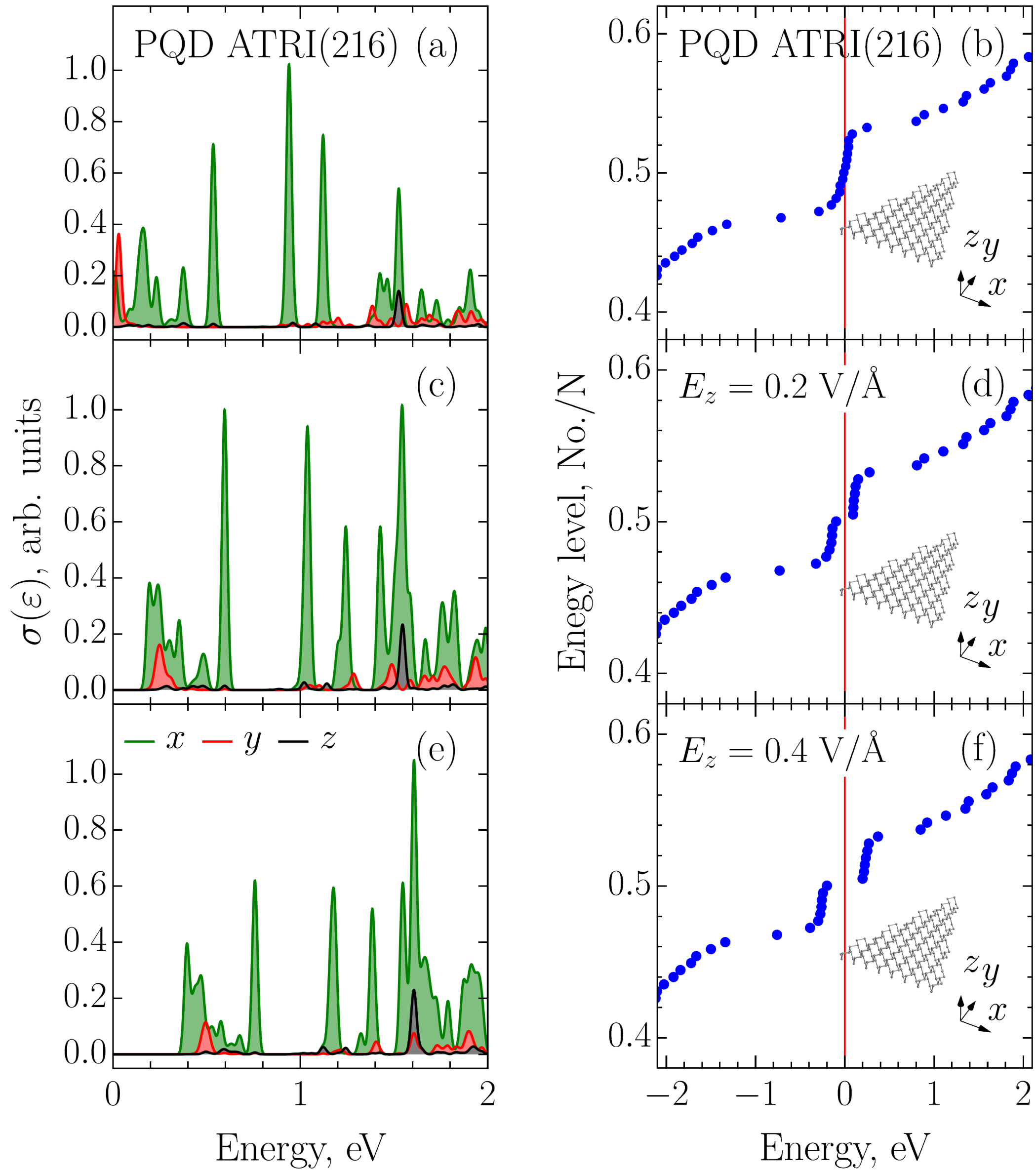

Figure 5.7: The optical absorption cross-section (a), (c), (e) and the corresponding energy levels (b), (d), (f) of triangular armchair phosphorene QDs under the effect of an electric field.

states (see Fig. 5.7 (f)).

Figure 5.8 shows the electronic states and optical absorption cross-sections of hexagonal phosphorene QDs with armchair termination. In this case, the smearing of the edge states is small, Fig. 5.8 (b), (d), and (f), and the transitions between them are given by two strong absorption peaks (shown in red and green) at $\varepsilon \approx 0.05$ eV. By varying the electric field we can control the position of these two peaks in the absorption spectrum. For instance, at $E = 0.2$ V/Å they are situated at $\varepsilon \approx 0.25$ eV, therefore it is possible to tune efficiently optical transitions within the energy gap of the hexagonal phosphorene QDs with armchair terminations. Moreover, it can be seen that at $E = 0$ V/Å, Fig. 5.8 (a), the red absorption peak for incident y-polarized electromagnetic wave has a higher intensity than the green peak for x-polarized incident wave. However, by increasing the electric field the situation is inverted: the green peak becomes more intense than the red peak. At zero field the energy gap is almost zero, see Fig. 5.8 (b), which promotes a strong y-absorption peak. At high values of the electric field the energy gap increases leading to decrease in the intensity of the y-absorption peak (red peak in Fig. 5.8 (e)) and increase in the x-absorption (green peak at $\varepsilon \approx 0.5$ eV in Fig. 5.8 (e)). Therefore, we conclude that the intensity of the x-absorption peak is directly proportional to the opening of the energy gap between QZES and y-absorption peak intensity is inversely proportional to the energy gap.

5.4.3 Edge roughness

In this section, we study the effect of edge disorder on the electronic and optical spectra of phosphorene QDs. The edge disorder was modeled as described at the end of Section 5.2 for all types of quantum dots considered in Section 5.4.2; this means that the edges of the initial bounding polygons were replaced with random Koch curves. We consider replacement for AHEX, ATRI, ZHEX and ZTRI types of phosphorene dots with the number of atoms $N = 366, 216, 384$, and 222, respectively. For random structures we keep the same notations as for the original regular structure with '(r)' appended at the end, e.g. AHEX is changed to AHEX(r). We

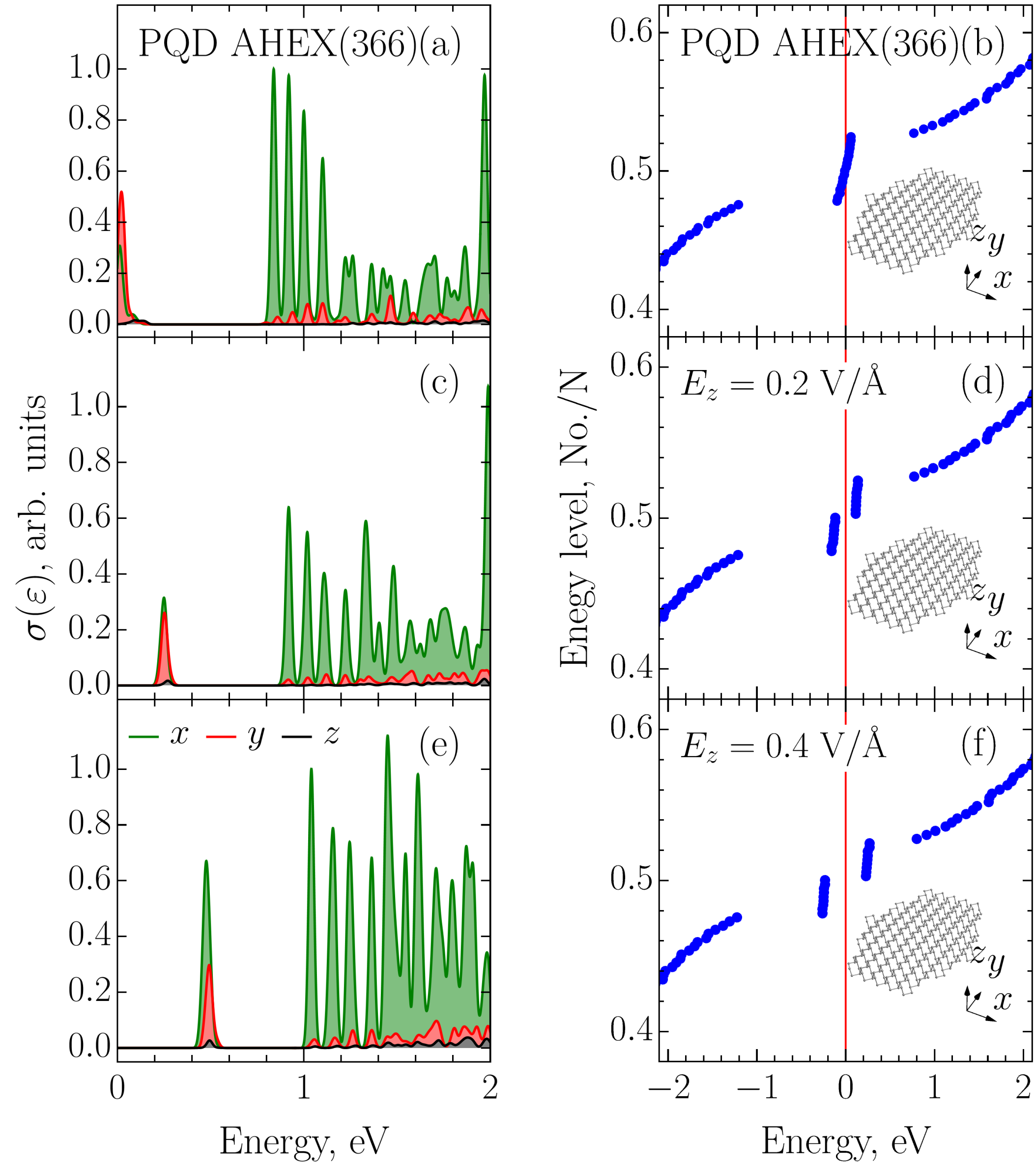

Figure 5.8: The effect of a perpendicular electric field on the optical absorption cross-section (a), (c), (e) and corresponding energy levels (b), (d), (f) of hexagonal armchair phosphorene QDs.

also clearly indicate for each structure the new number of atoms N. The random structures have edges of neither armchair nor zigzag type but their initial shape and crystallographic orientation are preserved.

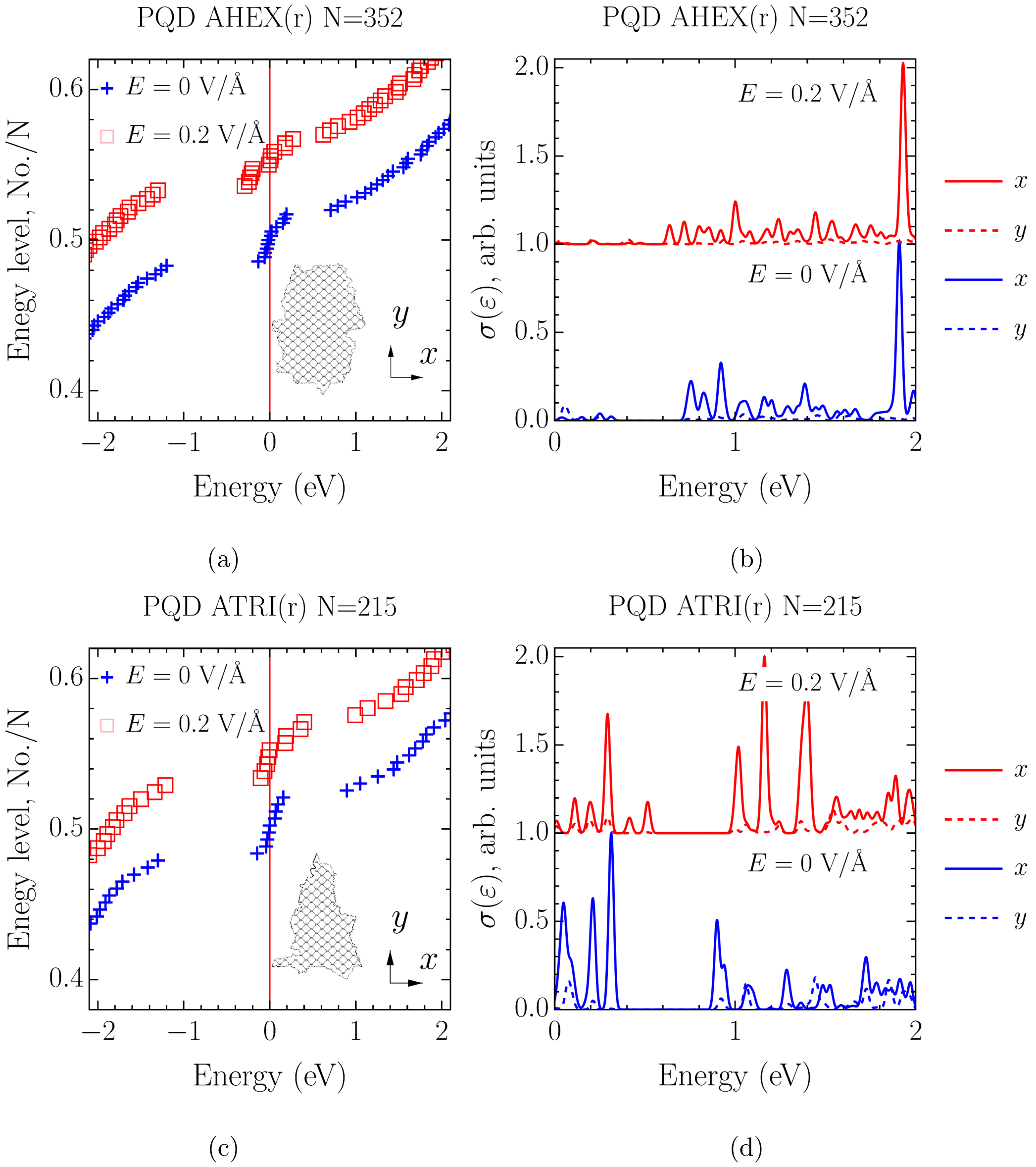

Figure 5.9: The effect of the electric field on the energy levels and optical absorption of disordered PQDs based on those with armchair edges. (a), (c) The energy levels and (b), (d) normalized absorption cross-sections of hexagonal and triangular quantum dots, respectively.

In Figure 5.9 we present the energy levels and absorption spectra with and without a normal electric field for quantum dots with rough edges based on those with armchair edges – AHEX(r) with $N = 352$ and ATRI(r) with $N = 215$. For clarity, in this picture, the energy levels for $E = 0.2$ V/Å are vertically shifted by 0.05 with respect to those at $E = 0$ V/Å. A vertical shift of 1 is used for corresponding normalized absorption spectra of both x- and y-polarization. The similar plots for irregular phosphorene dots based on QDs with zigzag edges are shown in Fig. 5.10.

In all cases the quasi-zero energy states within the bulk gap, i.e. between conduction and valence band states, survive but become more dispersed forming wider energy band around the Fermi level. The number of QZES in random structures is changed compared to the regular ones but it correlates with the number of unpaired phosphorous atoms highlighted in Fig. 5.1 as discussed for regular QDs. The deviation from the rule was found in the cases when two atoms without a t_2 hopping were linked by t_1 hopping. We did not obtain dielectric structures, e.g. without QZES, in 10 random seeds for each type of the irregular PQDs but we checked that the QZES disappear if all phosphorous atoms are paired, by t_2 hopping, by purposely engineering such a PQD with a round shape and $N = 412$ (see Appendix F). The effect of the electric field is further broadening of the zero energy band. Unlike the case of regular ATRI and AHEX PQDs the splitting is not that clear for the corresponding QDs with irregular edges and the two groups of the QZES are less distinctive.

One can also see from Figs. 5.9 and 5.10 that edge disorder can suppress QZES-associated transitions in the case of hexagonal structures, whereas transitions between the QZES or from QZES to HOEL and LUEL usually stay strong for triangular shapes of the dots.

5.5 Conclusions

In summary, we investigated the electronic and optical properties of phosphorene quantum dots of triangular and hexagonal shapes with regular and irregular edges and with armchair and zigzag crystallographic orientations. All studied types of PQDs are metallic due to a new, in comparison to majority of graphene dots, set

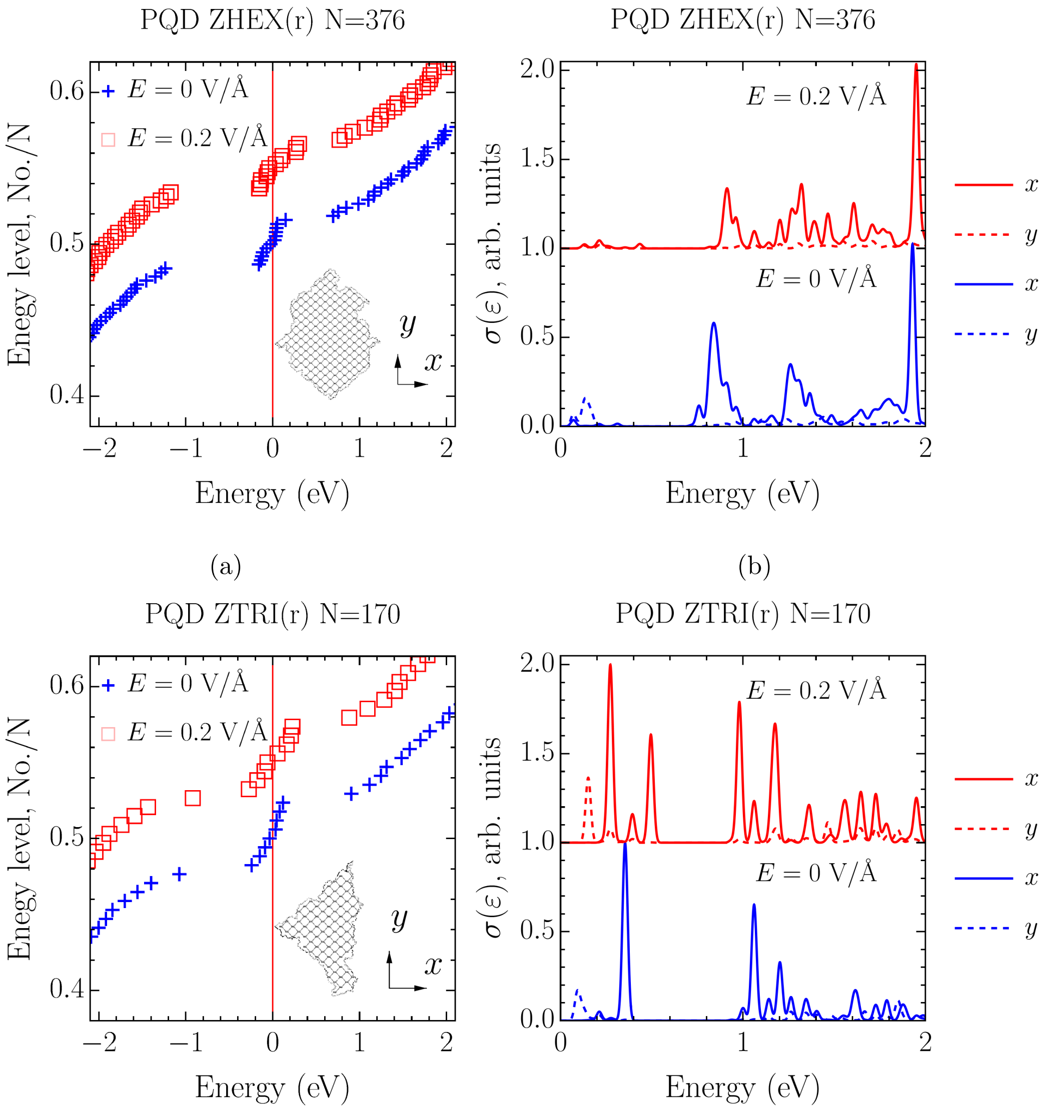

(a) (b) (c) (d)

Figure 5.10: The same as Fig. 5.9 but for disordered PQDs based on those with zigzag edges. (a), (c) Energy levels and (b), (d) absorption cross-section of hexagonal and triangular quantum dots, respectively.

of electronic energy states formed around the Fermi level. These states emerge because of the puckering structure of phosphorene effectively presented by phosphorous atoms distributed between the two layers. Similar states exist only in triangular graphene and silicene counterparts with zigzag edges [246, 92]. We found that for each type of phosphorene dot with regular edges the number of these peculiar states is related to the dot size indexed by the number of hexagonal elements at one edge, see Table 5.3. A more general rule, which also works for structures with disordered edges, is that the number of these states is equal to the number of phosphorous atoms which do not have a counterpart atom in the opposite layer. At the same time, unpaired atoms connected by the t_1 hopping parameter do not contribute into the number of new states. Thus, the engineering of dielectric phosphorene quantum dots should be a more technologically challenging problem compared to that of the metallic dots.

The absorption spectra due to the in-plane x- and y-polarizations of the incident light are very different in phosphorene QDs, whereas such two spectra have similar shapes in the graphene dots. The y-polarization mostly contributes to the transitions within the new set of quasi-zero energy states. These new states play a decisive role in optical properties of PQDs, increasing the number of absorption peaks in the low-energy region (< 2 eV) of phosphorene quantum dots compared to graphene ones.

Applying an external electric field to the structure in the out-of-plane geometry greatly influences these absorption peaks by blue-shifting and splitting them, thereby modifying absorption gaps. Due to the quasi-zero energy states robustness against edge disorder and due to their optical activity in the infrared range of the electromagnetic spectrum, nanoclusters of phosphorene may be used as a filler material for producing composites for electromagnetic shielding. A strong linear dichroism makes small phosphorene quantum dots a promising material for infrared polarizers and tunable polarization-sensitive detectors. In particular, hexagonal dots with armchair edges demonstrate the most appealing behaviour having an extremely strong, well-isolated absorption peak tunable in a wide frequency range.

A natural extension of our calculations is to use the first principles methods [271], since many-body effects are known to cause a redistribution of energy levels shifting the positions of some absorption peaks. Taking into account deeper σ-orbitals should result in additional peaks. However, this should not affect the main conclusions of our work.

Chapter 6

Conclusions and future work

In this thesis the optical properties of various low-dimensional nanostructures based on 2D materials have been systematically investigated. The particular focus of this study was on interband transitions in THz and infrared regions of the electromagnetic spectrum where novel types of emitters and absorbers are in great demand. In particular we have considered main types of graphene nanoribbons, carbon nanotubes, silicene and phosphorene quantum dots. The effect of intrinsic strain has been considered for tubes and ribbons, while the tunability by means of an external electric field has been a focus for quantum dot investigation. For phosphorene quantum dots the model of the edge disorder has been proposed and applied. In all the cases the research was based on the tight-binding model though with varying degree of complexity making it sensitive enough for catching essential physics of the structures. This study has delivered a number of interesting results disclosing new possible directions of the future research.

In the Part I of this thesis the equivalence of optical properties between single-walled carbon nanotubes and monolayer graphene nanoribbons was revealed and examined in detail. These results, however, were obtained for the regular and highly symmetric structures of zigzag and armchair type, therefore the question if this equivalence maintains for less symmetric chiral tubes and ribbons should be a subject of the future research. In the present study the primary focus has been on the linear polarization of the incident light parallel to the axis of the translation symmetry in the tubes and ribbons. The next logical step would be the consideration of the incident light polarized perpendicular to the translation symmetry axis. Such a calculation can be done by considering matrix elements of the position operator in a unit cell of the structure. An alternative approach to the problem is to consider both polarizations for the tubes and ribbons within the tight-binding model cluster approximation. In this approximation the infinitely long tube or ribbon should be replaced with a long enough but finite structure (tube or ribbon). Then the dipole transitions probabilities for both polarizations can be calculated as described in Chapters 4 and 5. However, it should be noticed that convergence of the cluster approach to the results based on just one unit cell is slow. The cluster based method also requires solving eigenproblem for a larger matrix Hamiltonian. This is partially explains our choice of the model with a periodic boundary condition in the direction of the structure translation invariance. The aforementioned slow convergence might be faster for some fist principles methods functionals. This should be definitely the subject of the later research.

Another interesting and important question which, however, in contrast to the aforementioned one is not that demanding to the computational power is the influence of the higher order nearest-neighbours. It would be interesting to check if the ribbon-tube equivalence holds true upon accounting for hoppings between the higher order nearest-neighbours. If this is true then the found equivalence may have even broader significance. Since the tight-binding model employed in Chapter 2 differ from that in Chapter 5 essentially by the number of nearest neighbours, the correlation of absorption spectra can take place for phosphornene nanoribbons and nanotubes too. Similar to graphene, phosphorene is stable under the ambient conditions without a substrate [8] and it can also form tubular structures. The stability of amrchair phosphorene nanotubes up to $T = 600$ K has been recently reported [272, 273]. It is also worth pointing out that boron nitride nanotubes [274] are analogous to carbon nanotubes, therefore the above drawn conclusion may be also applicable to the tubes and ribbons made of this material.

One of the main achievements of Chapter 2 is the derivation of the analytic expressions for the velocity matrix elements. These expressions allowed us to investigate the matrix element dependence on the electron wave vector in the whole Brillouin zone. The found smooth behaviour at the Dirac point ($k = 2\pi/3$) implies the absence of the relation to the topological singularity in graphene [132] in contrasts to the armchair ribbons or all quasi-metallic narrow-gap carbon nanotubes considered in Chapter 3. However, in the present work rather narrow ribbons were considered with the width up to 25 zigzag chains. This was done on purpose to scrutinize the velocity matrix element dependence on the electron wave vector for various type of the allowed transitions. Since now this dependence has been examined in detail, wider zigzag ribbons can be inspected next paying particular attention to the velocity matrix element relation in zigzag ribbons to the topological singularity in the velocity matrix element in graphene (see, Fig. 3.2 in Chapter 3).

The investigation of the zigzag ribbon matrix elements in Chapter 2 has been carried out with the future device application in mind very much like it is done in Chapter 3. However, the electron-electron interaction resulting in a small band gap in zigzag ribbons has been neglected to proceed with the analytical treatment of the problem. In the tight-binding description the band gap due to the electron-electron interaction can be modeled by the non-zero on-site energy term in the matrix Hamiltonian. The same modeling is applicable for the effect of the in-plane electric field. Therefore, the next step could be to extend the treatment presented in Chapter 2 to include the external field. This would allow not only to investigate the effect of the band gap opening but also to investigate tunability so desirable for the device applications. Similar to the quantum dots zero-energy edge states considered in Chapter 4 the zigzag ribbon edge states are tunable in the external electric field applied in-plane [91, 15, 14]. This geometry of the field, of course, requires fabrication of the side gates instead of the back ones. The current technological challenges for side gates fabrication may be resolved in the future therefore this gate geometry should not be ruled out from consideration.

Another direction of future research in relations to the problem considered in Chapter 2 is to study the role of excitonic effects. Indeed, these effects have been a rare subject of the study in armchair carbon nanotubes and zigzag ribbons. Although some theoretical [275, 167] and experimental [276] works can be found in the literature for both tubes and ribbons, they are all dealing with the transitions in the optical frequency range for narrow tubes and ribbons. For instance, in Ref. [276] the absorption spectrum of $(21, 21)$ armchair single-walled nanotube was measured. This tube is the one for which correlation of absorption peaks with the corresponding zigzag ribbon is presented in Fig. 2.9. However, only the first absorption peak, which does not have a counterpart in the corresponding zigzag ribbon, is investigated in the aforementioned research. Another theoretical study has reported that the exciton binding energies for the third and fourth energy transitions (above 3 eV) in $(10, 10)$ armchair nanotube are about 50 meV [275]. This implies that the role of the excitonic effect decreases for higher energy transitions in metallic tubes. At the same time, to the best of our knowledge the excitonic effects for transitions above 3 eV have not been considered in zigzag ribbons. The consideration of the excitonic effects for larger diameter armchair tubes and wider zigzag ribbons is needed to reveal how they affect the discovered correlation of absorption peaks.

In Chapters 2 and 3, the resutls using periodic (tubes) and hard wall (ribbons) boundary conditions have been matched. It is quite natural to imagine that similar matching could be investigated between Mobius boundary condition and the two above-mentioned ones. The Mobius rings made of graphene nanoribbons have already been a subject of an intensive theoretical study in the tight-binding model [277, 278], the density functional theory [279, 280], the hybrid density functional tight-binding model [281]. An experimental realization of the molecular Mobius strips was reported in 1982 [282], but Mobius graphene nanorings are yet to be demonstrated.

In Chapter 3 of this thesis the high probability rate of transitions across the curvature induced band gap in tubes and edge-effect induced band gap in armchair ribbons has been discovered and investigated. The high probability rate of the transitions can be a basis for the novel types of THz radiation sources. In Chapter 3, we propose a lasing scheme for generating THz radiation. This scheme takes into account the position of the Fermi level, whereas it neglects the effect of temperature. Our preliminary estimate shows the finite temperatures should decrease the efficiency of generation. The proposed scheme also neglects non-radiative processes such as impact recombination of the electrons and holes. The impact recombination which is also referred to as Auger recombination is famous for preventing efficient THz lasing in conventional semiconductor nanocrystals [283, 284, 285, 286]. Wang et al. report that for semiconducting single-walled carbon nanotubes the role of the Auger recombination increases with the increasing exciton binding energy [287]. Also, it is known that the exciton binding energy scales with the band gap and cannot exceed it [288, 289]. Similar behaviour is reported theoretically for narrow-gap nanotubes [171], which suggests the Auger processes may be of less importance in these structures. However, it is evident that more research is needed to be carried out in this direction. Thence, a careful consideration of the Auger effects in conjunction with the proposed generation scheme is required to reveal if a practical device application is achievable. Nevertheless, it should be stressed that the reported giant enhancement of the interband transitions across the band gaps induced by intrinsic strain in tubes and ribbons is universal. In other words, this probability is independent of the curvature effect strength in the tube or edge-effect strength in the ribbon.

Another way to extend the study presented in Chapter 3 is to consider an array of tubes or ribbons. For an array, the resulting emission is proportional to the N^2, where N is the number of coherent emitters in the array. This effect is often referred to as Dicke effect [290]. Concurrently, to enhance photolumenescence, the array structure of tubes or ribbons can be embedded into a microcavity [291, 292, 293]. The strong coupling regime for some semiconducting nannotubes has been recently investigated experimentally [294].

As for the optical properties of the gapped graphene systems, one should note that the analytic expressions for the optical transition matrix elements are derived for linear and circular polarizations. The next step could be the synthesis of these expressions in a single one allowing application to the elliptic polarization.

In Chapter 4 of this thesis the comparative analysis of silicene and bilayer graphene quantum dots has been carried out. The hexagonal and triangular shapes of these dots were considered for both zigzag and armchair edge geometries. According to the obtained results, only quantum dots with triangular shape and zigzag edge geometry support the peculiar group of degenerate edge states dubbed zero-energy states. This group of states is tunable by the external electric field applied in the out-of-plane geometry, e.g. via the back gate. The tight-binding model employed for the investigation does not take into account many-body and excitonic effects. The preliminary check by means of first principles calculations shows that the degenerary of zero-energy states can be lifted up and additional low-energy transitions can arise in the systems. A more thorough study of this subject is necessary in the future. Also, the structures studied in Chapter 4 have an ideal geometry. The relaxation of the chemical bond at the edges of the structure was omitted for the sake of simplicity. This effect can be included into the tight-binding model by parameterization of the hopping integrals with the chemical bond length.

In Chapter 5 phosphorene quantum dots of triangular and hexagonal shapes with zigzag and armchair crystallographic orientation of the edges have been studied. If follows form the obtained results that in terms of tunability the most promising quantum dots are those with hexagonal shape and armchair edges. However, the edge irregularity smears the two distinctive groups of quasi-zero-energy states in such dots suppressing transitions between them. The consideration of the irregular edges of the phosphorene quantum dots revealed a simple empirical rule for determining the number of quasi-zero-energy states in all the major types of phosprorene quantum dots. This rule provides a recipe for designing phosphorene quantum dots with dielectric properties. An example of such a dot is given in Appednix F.

The fractal-based methodology of modeling the edge roughness in phosphorene quantum dots described in Chapter 5 is intended to imitate the result of various uncontrolled fluctuations in the conditions of quantum dot synthesis. To reveal the pure effect of the edge roughness, we neglected the structure relaxation at the edges and assumed that all the atoms has the same coordinates as they would have within the 2D phosphorene. The next natural step is to supplement this model with the edge relaxation via geometry optimization procedure, as has been done for graphene quantum dots [295, 296]. The random fractal-based modeling of the edge roughness proposed in Chapter 5 results in an inhomogeneous distribution of the hopping integrals at the edges of the structure. We note that this type of disorder is different from previously studied, for instance, for graphene quantum dots, where the on-site energies were varied either throughout the whole structure or its edges [297], or in 2D phosphorene [298], where vacancies and impurity atoms were distributed randomly throughout the whole structure. Unlike the theoretical studies, in real systems all types of the edge disorder are hardly separable, therefore the next step could be combining these types together to find out which of them is a leading one.

In Chapters 4 and 5 optical properties of individual quantum dots have been considered. Although the absorption spectra of such objects can be, in principle, tested by the spatial-modulation spectroscopy [299, 300], the future research could switch the focus to the modeling the composite materials where these dots are used as a filler material.

Appendix A

Wave function parity factor

In order to clarify the origin of the wave function parity factor, we present in detail the simplification of the eigenvector component (2.23).

Equation (2.23) can be further simplified if one expresses $2\cos(k/2)$ in terms of the quantized momentum θ from the quantization condition (2.19) as

$$2\cos\frac{k}{2} = \frac{\sin w\theta}{\sin\left[(w+1)\theta\right]} \tag{A.1}$$

and then substitutes the result into the square brackets of Eq. (2.23):

$$\sin p\theta - 2\cos\frac{k}{2}\sin\left[(p+1)\theta\right] = \frac{\sin\theta\sin\left[(p-w)\theta\right]}{\sin\left[(w+1)\theta\right]} \,. \tag{A.2}$$

Note that the proper energy E entering Eq. (2.23) can also be re-casted only in terms of θ by substituting (A.1) into Eq. (2.14):

$$E(\theta) = \pm\frac{\gamma|\sin\theta|}{|\sin\left[(w+1)\theta\right]|} \,. \tag{A.3}$$

Now making use of Eqs. (A.2) and (A.3), one readily obtains that

$$c_{2p+1} = \pm(-1)^{p+1}\frac{\sin\theta}{|\sin\theta|}\frac{|\sin\left[(w+1)\theta\right]|}{\sin\left[(w+1)\theta\right]}\sin\left[(p-w)\theta\right] \,, \tag{A.4}$$

where the upper (lower) sign is applied for the conduction (valence) band state. The first ratio in the expression above is a trivial one, $\frac{\sin\theta}{|\sin\theta|} = 1$ for $\theta \in (0,\pi)$. However, the second ratio deserves special attention because, as we will see next, it is a clue to the optical properties of zigzag ribbons.

The magnitude of the second ratio is, of course, unity, but its sign depends upon θ. To determine the sign of the ratio $\frac{|\sin[(w+1)\theta]|}{\sin[(w+1)\theta]}$ one needs to analyse it along with the quantization condition (2.19). Since absolute value is always positive the sign of the ratio is determined by the sign of its denominator defined by the secular equation solutions.

Let us investigate how secular equation solutions, θ_j, are spread in the range $(0, \pi)$. For this purpose one can continuously change the parameter q from 0 to ∞ similar to what is presented in Fig. 2.2. Varying q between the above mentioned limits, one finds that the two values of q determine the left and right ends of the intervals in each of which one θ_j is confined. By putting the parameter $q = 0$ into Eq. (2.19) we get $\sin w\theta_j = 0$ with $\theta_{j,\min} = \pi(j-1)/w$ being solutions, while $q = \infty$ yields $\sin[(w+1)\theta] = 0$ with $\theta_{j,\max} = \pi j/(w+1)$ as solutions; in both cases $j = 1 \ldots w$ enumerates solutions. It is worth noting that although the upper value of $q = 2\cos(k/2)$ is limited to 2, we can take a greater value for an estimation because an increase of q above 2 shifts the initial interval right boundaries so that the original intervals are contained within the new θ-intervals depicted in Fig. 2.2. The left boundaries of the intervals can also be pushed further left to put all the new intervals within even wider ones:

$$\pi(j-1)/(w+1) < \theta_j < \pi j/(w+1)\,. \tag{A.5}$$

With inequalities (A.5) at hand it is easy to analyse the argument of $\sin[(w+1)\theta_j]$ for it is evident that for all θ_j satisfying inequalities (A.5) the sine function argument $(w+1)\theta_j$ is squeezed between $\pi(j-1)$ and πj. This leads to positive and negative signs of $\sin[(w+1)\theta_j]$ for odd and even j, respectively. Therefore, the second ratio in Eq. (A.4) can be written as

$$\frac{|\sin[(w+1)\theta_j]|}{\sin[(w+1)\theta_j]} = (-1)^{j-1}\,, \tag{A.6}$$

where j is an integer being interpreted as the band number.

Appendix B

Edge and bulk state eigenvectors at the transition point

Let us obtain the wave functions of the edge states in the explicit form and show how it reduces at the transition point k_t defined as a solution of the equation $2\cos(k/2) = w/(w+1)$. As has been mentioned above, to do this one needs to use substitution $\theta \to i\beta$, which upon application to (2.30) yields

$$\begin{pmatrix} \widetilde{c}^{(j)}_{2p-1} \\ \widetilde{c}^{(j)}_{2p} \end{pmatrix} = \begin{pmatrix} \pm i \sinh\left[(w+1-p)\beta_j\right] \\ i \sinh p\beta_j \end{pmatrix} , \tag{B.1}$$

with $p = 1 \ldots w$. Note that $j = 1$ for bands containing edge states, therefore the parity factor has been ruled out and $\mp$ in (2.30) has been replaced with $\pm$ in (B.1). The same substitution applied to the normalization constant (2.31) leads to

$$N_j = \frac{1}{\sqrt{w - \cosh\left[(w+1)\beta_j\right] \dfrac{\sinh w\beta_j}{\sinh \beta_j}}} . \tag{B.2}$$

As one can notice, the expression under the square root of (B.2) is negative, therefore the imaginary unit resulting form it must cancel with that in (B.1). Hence, for normalized eigenvector components it can be written

$$\begin{pmatrix} \widetilde{c}^{(j)}_{2p-1} \\ \widetilde{c}^{(j)}_{2p} \end{pmatrix} = N_j \begin{pmatrix} \pm \sinh\left[(w+1-p)\beta_j\right] \\ \sinh p\beta_j \end{pmatrix} , \tag{B.3}$$

where $p = 1 \ldots w$ and

$$N_j = \frac{1}{\sqrt{\cosh\left[(w+1)\beta_j\right] \dfrac{\sinh w\beta_j}{\sinh \beta_j} - w}} . \tag{B.4}$$

Note that the eigenvector (B.3) does not contain $(-1)^J$ factor like Eq. 34 in work [112]. Even for inverse band enumeration this factor would be $(-1)^w$ not $(-1)^J$. At the transition point $\beta_j \to 0$, which results in divergence in (B.4) if all hyperbolic functions are expanded to the first order. However, using the original definition of the constant:

$$N_j = \frac{1}{\sqrt{2\sum_{p=1}^{w} \sinh^2 p\beta_j}} , \tag{B.5}$$

where the factor of 2 is due to the fact that $\sum_{p=1}^{w} \sinh p\beta_j = \sum_{p=1}^{w} \sinh\left[(w+1-p)\beta_j\right]$, the same first order expansion results in

$$N_j = \frac{1}{\beta_j \sqrt{2\sum_{p=1}^{w} p^2}} . \tag{B.6}$$

Thus, for normalized eigenvectors in the vicinity of the transition point one has

$$\begin{pmatrix} \tilde{c}_{2p-1}^{(j)} \\ \tilde{c}_{2p}^{(j)} \end{pmatrix} = \frac{1}{\sqrt{2N_c}} \begin{pmatrix} \pm(w+1-p) \\ p \end{pmatrix} , \tag{B.7}$$

where

$$N_c = \sum_{p=1}^{w} p^2 = \frac{w(w+1)(1+2w)}{6} \tag{B.8}$$

The same result can be obtained starting from the eigenvectors (2.30) and their normalization constant specified as $N_j = 1/\sqrt{2\sum_{p=1}^{w} \sin^2 p\theta_j}$, therefore wave functions approaching k_t from the left and from the right attain the same value. As a result of this seamless transition of one type of functions into another, the VMEs can be obtained as smooth functions of electron wave vector k for the lowest conduction (higherst valence) subbands, i.e. for $j = 1$.

It is to be mentioned here that the edge states can be also obtained in zigzag carbon nanotubes with finite length [139]. Unlike the case of the infinite ribbon the number of such states is finite in tubes. Recently, it has been shown that this number is related to the winding number [301, 178]. However, the state at the transition point, the charge density of which decays quadratically towards the structure center, seems to be less likely in the finite tubes.

Appendix C

Periodic boundary conditions

In this appendix, we demonstrate how the fixed end ('hard wall') boundary condition employed in this paper for zigzag ribbon investigation is related to the periodic boundary condition that is used for carbon nanotubes. A carbon nanotube of the armchair type (see Ref. [11] for tubes classification) is unrolled into a graphene nanoribbon with zigzag edges. The tight-binding Hamiltonian of the armchair nanotube differs from that of the zigzag ribbon by the upper right and lower left non-zero elements. For instance, for the ribbon Hamiltonian given by Eq. (2.1) an equivalent tube Hamiltonian is

$$H = \begin{pmatrix} 0 & \gamma q & 0 & \gamma \\ \gamma q & 0 & \gamma & 0 \\ 0 & \gamma & 0 & \gamma q \\ \gamma & 0 & \gamma q & 0 \end{pmatrix} . \tag{C.1}$$

Despite these differences the eigenproblem of such a Hamiltonian reduces to the same transfer matrix equation as Eq. (2.7). The periodic boundary condition, however, requires $C_{N+1} = C_1$, whence it follows that the secular equation is $\det(T^w - I) = 0$. To obtain the explicit form of the secular equation, one can use (2.18), but there is a faster way if one uses the following relation [141]:

$$\det\left(T^w - I\right) = \det T^w + \det I - \mathrm{Tr}\left(T^w\right) . \tag{C.2}$$

Using the above relation and taking into account that $\det T = 1$, the secular equation can be recasted as

$$\mathrm{Tr}\,(T^w) = 2\,. \tag{C.3}$$

The cyclic property of the trace operation allows further simplification of the secular equation:

$$\mathrm{Tr}\left(S^{-1}\Lambda^w S\right) = \mathrm{Tr}\left(\Lambda^w S S^{-1}\right) = \mathrm{Tr}\,(\Lambda^w) = 2\,, \tag{C.4}$$

where Λ is a diagonal form of the transfer matrix T with the diagonal elements given by $\lambda_{1,2} = e^{\pm i\theta}$, i.e. a new variable θ is defined as $A = \cos\theta$ (cf. with Eq. (2.11)), S, S^{-1} are given by Eqs. (2.17). Such treatment is equivalent to that with $\lambda_{1,2}$ given by Eq. (2.11), the difference is in subband enumeration similar to that mentioned for the 'hard wall' boundary condition. In Figure 2.4, the tube's band enumeration, we refer to as direct one, corresponds to $A = -\cos\theta$. The above chosen inverse enumeration, $A = \cos\theta$, is shown in the right panel of Fig. 2.5. It was chosen to obtain the tube's energy bands in a form close to graphene energy bands [50, 65, 11]. Thus, for an armchair tube secular equation we end up with

$$\lambda_1^w + \lambda_2^w = 2\cos(w\theta) = 2; \Leftrightarrow \cos(w\theta) = 1\,, \tag{C.5}$$

whence it is evident that $\theta_j = 2\pi j/w$ with j being an integer numbering solutions and $w = N/2$ with N being the number of carbon atoms in the tube's unit cell. To obtain the tube energy bands θ_j should be substituted into $\pm\gamma\sqrt{q^2 + 2q\cos\theta + 1}$, which yields:

$$E_j(k) = \pm\gamma\sqrt{4\cos^2\frac{k}{2} + 4\cos\frac{k}{2}\cos\frac{2\pi j}{w} + 1}\,. \tag{C.6}$$

where we use j for the band numbering.

In the case of the 'hard wall' boundary condition and variable θ introduced as above, i.e. with the reverse enumeration of the ribbon bands, the secular equation has the form:

$$\sin w\theta + 2\cos\frac{k}{2}\sin\left[(w+1)\theta\right] = 0\,. \tag{C.7}$$

The proper energy is obtained by substituting solutions of this equation into $\pm\gamma\sqrt{q^2 + 2q\cos\theta + 1}$. Solutions of (C.7) can be found in the zero approximation by setting $k = 0$; ideally, one should set $q = 2\cos(k/2) \to \infty$. This leads to

$\sin[(w+1)\theta] = 0$ with $\theta_j = \pi j/(w+1)$ being solution. Equating θ_j obtained for a tube and ribbon, one gets:

$$\frac{2\pi j}{N_t/2} = \frac{\pi j}{N_r/2+1}\,, \tag{C.8}$$

where $N_{t,r}$ is the number of atoms in the unit cell of the tube and ribbon, respectively. As follows from (C.8) if

$$N_t = 2N_r + 4 \tag{C.9}$$

then the proper energies are approximately equal at $k = 0$. It is also possible to consider the opposite limit when $k = \pi$, which leads to $\theta_j = \pi j/w$ in the case of the ribbon. The usage of this θ_j results in a better match of the ribbon and tube energies close to the edge of the Brillouin zone, i.e. at $k = \pi$, if the following relation holds between the number of atoms in the structures: $N_t = 2N_r$.

Appendix D

Armchair nanotube selection rules

In this section, we derive selection rules for transitions in armchair carbon nanotubes (ACNTs). In spite of being known for a long time [134, 129, 135, 136, 137, 138] they have not been derived from the full tight-binding Hamiltonian. The purpose of this exercise is to provide deeper understanding of the difference in the optical properties of zigzag graphene nanoribbons and ACNTs and also to show their relation to the graphene single layer sheet.

To calculate velocity operator matrix elements one needs the wave functions. Substitution of Eq. (C.5) solution $\theta_j = \frac{2\pi j}{w}$ into $T^w - I$ gives a zero matrix. Hence, the boundary condition $C_{N+1} = C_1; \to (T^w - I)C_1 = 0$ is fulfilled for any components of the initial vector C_1. We see that for the periodic boundary condition the initial vector C_1 can be an arbitrary one. The most reasonable choice of C_1 is one of the eigenvectors (2.15). Let it be V_2. Then, with $\lambda_{1,2} = e^{\pm i\theta}$ the wave function components can be found from Eq. (2.7) as follows:

$$c_{2p-1}^{(j)} = \pm e^{-i\theta_j(p-1)} \frac{f_j}{|f_j|}; \qquad c_{2p}^{(j)} = e^{-i\theta_j p}\,, \tag{D.1}$$

where $p = 1 \ldots w$, $f_j = 1 + qe^{-i\theta_j}$, and we have changed the order of the components as it was done for Eq. (2.25). Introducing new function $\widetilde{f}_j = e^{i\theta_j/3} f_j$ into Eq. (D.1) and applying the unitary transform $U_j = \{u_{2p-1,2p-1}, u_{2p,2p}\} = \{e^{i\theta_j(p-2/3)}, e^{i\theta_j p}\}|_{p=1\ldots w}$ to the vector $\left|c^{(j)}\right\rangle$, we obtain

$$\widetilde{c}_{2p-1}^{(j)} = \pm \frac{\widetilde{f}_j}{|\widetilde{f}_j|}; \qquad \widetilde{c}_{2p}^{(j)} = 1\,, \tag{D.2}$$

where $p = 1 \dots w$. The normalization constant $N_j = 1/\sqrt{2w}$ for $\left|\widetilde{c}^{(j)}\right\rangle$ and it is independent of θ_j.

As one can see, the unitary matrix U_j depends on the band index j, therefore the new Hamiltonian that preserves the matrix element upon the transfromation of the $\left|c^{(n,m)}\right\rangle$ vectors is $\widetilde{H} = U_n H U_m^\dagger$. However, such a Hamiltonian satisfies the time independent Schrodinger equation only if $n = m$. This is the selection rule for ACNT optical transitions, which also means all transitions $c \to c$ and $v \to v$ are forbidden.

For $\widetilde{H} = U_j H U_j^\dagger$ the components of the vectors $\left|\widetilde{\zeta}^{(j)}\right\rangle$ are

$$\begin{aligned} \widetilde{\zeta}^{(j)}_{2p-1} &= -\frac{\gamma a}{\hbar}\sin(\frac{k}{2})e^{-2i\theta_j/3}\,; \qquad p = 1\dots w \\ \widetilde{\zeta}^{(j)}_{2p} &= \mp\frac{\gamma a}{\hbar}\sin(\frac{k}{2})e^{-2i\theta_j/3}\frac{\widetilde{f}_j}{|\widetilde{f}_j|}\,, \end{aligned} \tag{D.3}$$

with the upper "−" (lower "+") being used for the conduction (valence) subbands. By putting Eqs. (D.2) and (D.3) into Eq. (2.39), and accounting for the normalization constant N_j, for allowed transitions we have

$$\begin{aligned} M_{n(c),n(v)} &= -\frac{\gamma a}{\hbar}\sin(\frac{k}{2})\frac{\widetilde{f}_n^* e^{-2i\theta_j/3} - \widetilde{f}_n e^{2i\theta_n/3}}{2|\widetilde{f}_n|}\,, \\ &= \frac{\gamma a}{\hbar}\frac{\widetilde{f}_n^*(d\widetilde{f}_n/dk) - \widetilde{f}_n(d\widetilde{f}_n^*/dk)}{2|\widetilde{f}_n|}\,. \end{aligned} \tag{D.4}$$

Similarly, calculations for the group velocity yield

$$M_{n(s),n(s)} = \pm\frac{\gamma a}{\hbar}\frac{\widetilde{f}_n^*(d\widetilde{f}_n/dk) + \widetilde{f}_n(d\widetilde{f}_n^*/dk)}{2|\widetilde{f}_n|} \tag{D.5}$$

where "+" ("−") refers to the conduction (valence) subbands.

The same result is obtained from the graphene Hamiltonian and eigenvectors: $\langle c_c|\,\partial H/\partial k_y\,|c_v\rangle$ with $H_{11} = H_{22} = 0$,

$$H_{12} = H_{21}^* = \gamma\left(e^{ik_x a/\sqrt{3}} + 2e^{-ik_x a/2\sqrt{3}}\cos(k_y a/2)\right) \tag{D.6}$$

and $k_x = 2\pi j/C_h$, where C_h is the tube circumference and $a = 2.46$ Å is the graphene lattice constant. If $\theta_j = \sqrt{3}k_x a/2$, $k = k_y a$, and the tube chiral index is $w/2$, then $k_x = 4\pi j/(\sqrt{3}aw) = 2\pi j/C_h$. Hence, Eq. (D.4) can be restored by cutting graphene's optical transition matrix elements along the lines specified by the quantization of k_x. Finally, we note that a calculation of the matrix elements with the eigenvectors (D.1) and the Hamiltonian (C.1) also provides straightforward justification of the selection rules for it results in zero matrix elements when $n \neq m$.

Appendix E

Supplementary results

For the sake of completeness, in Fig. E.1 we present VME curves obtained for transitions between the lower (higher) energy valence (conduction) subbands. These

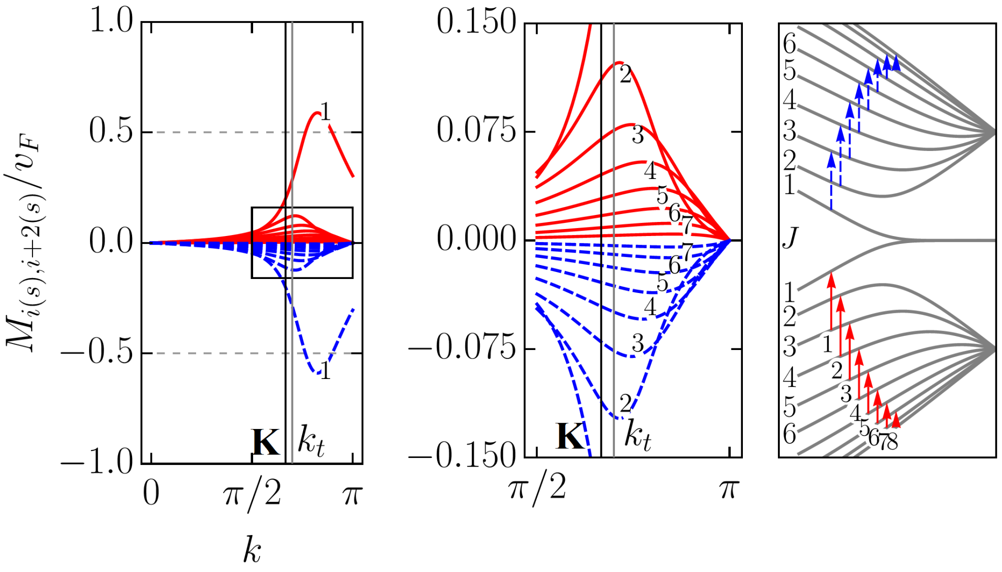

Figure E.1: The same as Fig. 2.6 (b) but for transitions between valence (conduction) subbands of lower (higher) energy: $v \to v; c \to c; \Delta J = 2$. As the plot is symmetric with respect to $k = 0$, only half of the BZ is presented. The part of the plot denoted by a rectangle is zoomed in the right panel followed by the transition scheme. The VME curves correspond to the transitions labeled with the same number in the scheme.

transitions can be referred to as $j(s) \to (j+2)(s)$, where $j = 1, \ldots, w-2$. Noticing that the curve labeled by '1' in Fig. E.1 is the same as the curve labeled by '2' in Fig. 2.6 (b), one easily sees that the transitions labeled from '2' to '7' are much weaker compared to the transitions in Fig. 2.6. Unlike the VME curves in Fig. 2.5 (a) and Fig. 2.6, all curves of $j(s) \to (j+2)(s)$ transitions converge to zero at the edge of the BZ and have extrema decreasing in magnitude and shifting from the $\mathbf{K}(\mathbf{K}')$ point towards the BZ edge for greater j's.

Figure E.2 shows that temperature has a similar influence on the absorption spectra to doping. The observed changes are explained in the same way as presented for Fig. 2.7. The peak due to the transitions $1(c) \to 3(c)$ is weaker and broader for ZGNR(9) compared to that in ZGNR(6). At the same time the peak at $\omega = \gamma$ due to transitions $1(c) \to 5(c)$ is quite intense.

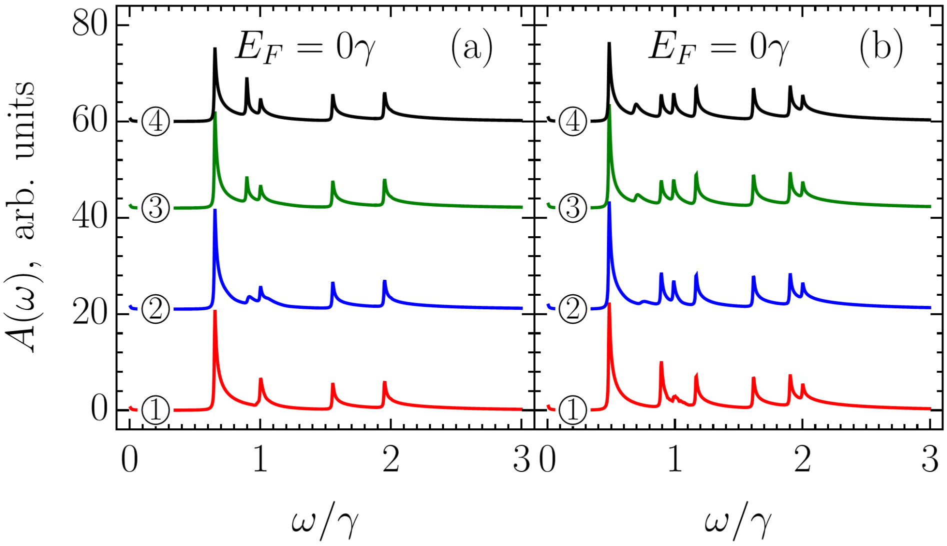

Figure E.2: The absorption spectra of zigzag ribbons with (a) $w = 6$ and (b) $w = 9$ for different temperatures: $T = 0$, 4, 77 and 300 K/γ for curves ①, ②, ③ and ④, respectively. Absorption spectra are shifted vertically for clarity.

Appendix F

A dielectric phosphorene quantum dot

In this appendix we demonstrate that dielectric phosphorene quantum dots without quasi-zero energy states (QZES) are possible though they are to be much more rare compared to those with QZES. Figure F.1 shows the energy levels and absorption spectrum of a dielectric phosphorene cluster of round shape with $N = 412$. Note that it is not the shape but rather the phosphorous atoms pairing with t_2 hopping that defines the absence of the QZES. The round phosphorene clusters with different size have QZES in their electronic spectra. The inset of Fig. F.1(a) demonstrates that the above mentioned condition for dielectric cluster existence is fulfilled leading to the empty energy gap of about 2 eV. This gap is also present in the absorption spectrum in Fig. F.1(b). As one can see, in this case the spectrum is entirely defined by the x-polarized transitions between valence and conduction band states, and y-polarized absorption, which is strong for transitions involving QZES, is negligible. According to our calculations the application of an electric field normal to the structure plane up to $E = 0.4$ V/Å, does not noticeably change the presented energy levels and optical spectrum.

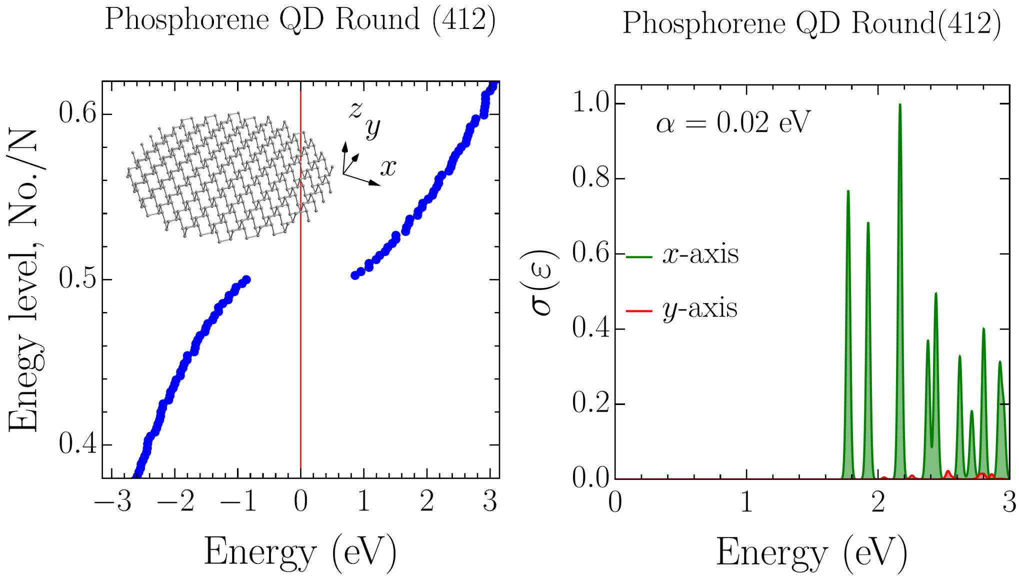

Figure F.1: The energy levels (a) and optical absorption cross-section (b) for a dielectric phosphorene quantum dot. The inset in (a) shows how the coordinate system is oriented with respect to the cluster.

Bibliography

[1] S. Cahangirov, M. Topsakal, E. Aktürk, H. ahin, and S. Ciraci, Phys. Rev. Lett. **102**, 236804 (2009).

[2] K. S. Novoselov *et al.*, Science **306**, 666 (2004).

[3] P. Vogt *et al.*, Phys. Rev. Lett. **108**, 1 (2012).

[4] C.-L. Lin *et al.*, Appl. Phys. Express **5**, 045802 (2012), 0811.4412.

[5] A. Fleurence *et al.*, Phys. Rev. Lett. **108**, 1 (2012).

[6] M. Derivaz *et al.*, Nano Lett. **15**, 2510 (2015).

[7] H. Liu *et al.*, ACS Nano **8**, 4033 (2014).

[8] A. H. Woomer *et al.*, ACS Nano **9**, 8869 (2015).

[9] C. C. Liu, H. Jiang, and Y. Yao, Phys. Rev. B - Condens. Matter Mater. Phys. **84**, 195430 (2011), 1108.2933.

[10] A. N. Rudenko and M. I. Katsnelson, Phys. Rev. B **89**, 201408 (2014).

[11] R. Saito, G. Dresselhaus, and M. Dresselhaus, *Physical Properties of Carbon Nanotubes* (Imperial College Press, London, 1998).

[12] V. A. Saroka, K. G. Batrakov, and L. A. Chernozatonskii, Phys. Solid State **56**, 2135 (2014).

[13] V. A. Saroka and K. G. Batrakov, Russ. Phys. J. **59**, 633 (2016).

[14] V. A. Saroka, K. G. Batrakov, V. A. Demin, and L. A. Chernozatonskii, J. Phys.: Condens. Matter **27**, 145305 (2015).

[15] V. A. Saroka and K. G. Batrakov, Dirac Electrons of Graphene Nanoribbons Tunable by Tranverse Electric Field, in *Physics, Chemistry and Applications of Nanostructures*, pp. 240–243, World Scientific, 2015.

[16] S. Iijima, Nature **354**, 56 (1991).

[17] B. Aufray *et al.*, Appl. Phys. Lett. **96**, 1 (2010).

[18] P. De Padova *et al.*, Appl. Phys. Lett. **96**, 2008 (2010).

[19] T. Maruyama, A. Kozawa, T. Saida, S. Naritsuka, and S. Iijima, Carbon N. Y. **116**, 128 (2017).

[20] X. Wei *et al.*, Nat. Commun. **7**, 12899 (2016).

[21] X. Tu, S. Manohar, A. Jagota, and M. Zheng, Nature **460**, 250 (2009).

[22] X. Tu, A. R. Hight Walker, C. Y. Khripin, and M. Zheng, J. Am. Chem. Soc. **133**, 12998 (2011).

[23] J. Cai *et al.*, Nature **466**, 470 (2010).

[24] H. Zhang *et al.*, J. Am. Chem. Soc. **137**, 4022 (2015).

[25] P. Ruffieux *et al.*, Nature **531**, 489 (2016).

[26] F. Schulz *et al.*, J. Phys. Chem. C **121**, 2896 (2017).

[27] T. H. Vo *et al.*, Nat. Commun. **5**, 3189 (2014).

[28] J. Lu, P. S. E. Yeo, C. K. Gan, P. Wu, and K. P. Loh, Nat. Nanotechnol. **6**, 247 (2011).

[29] X. Wang and H. Dai, Nat. Chem. **2**, 661 (2010), 1007.3226.

[30] X. Zhang *et al.*, ACS Nano **7**, 198 (2013), 1205.3516.

[31] L. Tapasztó, G. Dobrik, P. Lambin, and L. P. Biró, Nat. Nanotechnol. **3**, 397 (2008).

[32] G. Z. Magda *et al.*, Nature **514**, 608 (2014).

[33] J. Wu *et al.*, Macromolecules **36**, 7082 (2003).

[34] Y. Arakawa, Appl. Phys. Lett. **40**, 939 (1982).

[35] B. Ferguson and X.-C. Zhang, Nat. Mater. **1**, 26 (2002).

[36] M. Tonouchi, Nat. Photonics **1**, 97 (2007).

[37] M. Dragoman and D. Dragoman, Prog. Quantum Electron. **32**, 1 (2008).

[38] I. F. Akyildiz, J. M. Jornet, and C. Han, Phys. Commun. **12**, 16 (2014).

[39] V. Ryzhii *et al.*, J. Appl. Phys. **106**, 084507 (2009), 0908.2488.

[40] V. Ryzhii *et al.*, J. Appl. Phys. **113**, 1 (2013), 1305.5012.

[41] K. Batrakov and V. Soroko, Electron beam instability in graphene, in *Physics, Chemistry and Applications of Nanostructures*, pp. 307–310, World Scientific, 2011.

[42] V. Saroka, Reduction of Plasmon-Polariton Phase Velocity in a Double-Layer Graphene, in *Physics, Chemistry and Applications of Nanostructuress*, pp. 218–221, World Scientific, 2013.

[43] K. G. Batrakov, V. A. Saroka, S. A. Maksimenko, and C. Thomsen, J. Nanophoton. **6**, 061719 (2012).

[44] K. Batrakov and V. Saroka, Surface Plasmon Retardation in Graphene Bilayer, in *Nanomater. Imaging Tech. Surf. Stud. Appl.*, Springer Proceedings in Physics, Vol. 146, chap. 9, pp. 103–115, Springer, New York, 2013.

[45] K. Batrakov and S. Maksimenko, Phys. Rev. B **95**, 205408 (2017).

[46] R. R. Hartmann, J. Kono, and M. E. Portnoi, Nanotechnology **25**, 322001 (2014).

[47] A. J. Cohen, P. Mori-Sánchez, and W. Yang, Chem. Rev. **112**, 289 (2012).

[48] M. H. N. Assadi and D. A. H. Hanaor, J. Appl. Phys. **113**, 233913 (2013).

[49] J. C. Inkson, *Many-Body Theory of Solids* (Springer US, Boston, MA, 1984).

[50] P. R. Wallace, Phys. Rev. **71**, 622 (1947).

[51] D. C. Elias *et al.*, Nat. Phys. **7**, 701 (2011).

[52] Y. Zhang, Y.-W. Tan, H. L. Stormer, and P. Kim, Nature **438**, 201 (2005).

[53] K. S. Novoselov *et al.*, Science **315**, 1379 (2007).

[54] Y. Zheng and T. Ando, Phys. Rev. B **65**, 245420 (2002).

[55] R. R. Nair *et al.*, Science **320**, 1308 (2008).

[56] K. F. Mak, L. Ju, F. Wang, and T. F. Heinz, Solid State Commun. **152**, 1341 (2012).

[57] O. Klein, Zeitschrift Phys. **53**, 157 (1929).

[58] G. W. Semenoff, Phys. Rev. Lett. **53**, 2449 (1984).

[59] D. P. DiVincenzo and E. J. Mele, Phys. Rev. B **29**, 1685 (1984).

[60] M. I. Katsnelson, K. S. Novoselov, and a. K. Geim, p. 15 (2006), 0604323.

[61] Y. Wang *et al.*, Science **340**, 734 (2013).

[62] H. Kataura *et al.*, Synth. Met. **103**, 2555 (1999).

[63] R. B. Weisman and S. M. Bachilo, Nano Lett. **3**, 1235 (2003).

[64] K. Liu *et al.*, Nat. Nanotechnol. **7**, 325 (2012).

[65] R. Saito, M. Fujita, G. Dresselhaus, and M. S. Dresselhaus, Phys. Rev. B **46**, 1804 (1992).

[66] C. L. Kane and E. J. Mele, Phys. Rev. Lett. **78**, 1932 (1997).

[67] M. Ouyang, J. L. Huang, C. L. Cheung, and C. M. Lieber, Science **292**, 702 (2001).

[68] C. Zhou, J. Kong, and H. Dai, Phys. Rev. Lett. , 3 (2000).

[69] Y. Matsuda, J. Tahir-Kheli, and W. A. Goddard, J. Phys. Chem. Lett. **1**, 2946 (2010).

[70] K. Nakada, M. Fujita, G. Dresselhaus, and M. S. Dresselhaus, Phys. Rev. B **54**, 17954 (1996).

[71] S. Wang *et al.*, Nat. Commun. **7**, 11507 (2016).

[72] H.-C. Chung, C.-P. Chang, C.-Y. Lin, and M.-F. Lin, Phys. Chem. Chem. Phys. **18**, 7573 (2016).

[73] A. N. Rudenko, S. Yuan, and M. I. Katsnelson, Phys. Rev. B **92**, 085419 (2015).

[74] Y. Takao and A. Morita, Phys. B+C **105**, 93 (1981).

[75] Y. Takao, H. Asahina, and A. Morita, J. Phys. Soc. Japan **50**, 3362 (1981).

[76] J.-Y. Wu, S.-C. Chen, G. Gumbs, and M.-F. Lin, Phys. Rev. B **95**, 115411 (2017).

[77] M. Ezawa, New J. Phys. **16**, 115004 (2014), 1404.5788.

[78] E. Taghizadeh Sisakht, M. H. Zare, and F. Fazileh, Phys. Rev. B **91**, 085409 (2015).

[79] X. Zhang *et al.*, Angew. Chemie Int. Ed. **54**, 3653 (2015).

[80] L. L. Li, D. Moldovan, W. Xu, and F. M. Peeters, Nanotechnology **28**, 085702 (2017).

[81] J.-Y. Wu, S.-C. Chen, G. Gumbs, and M.-F. Lin, Phys. Rev. B **94**, 205427 (2016).

[82] H.-C. Chung, C.-W. Chiu, C.-N. Chen, and M.-F. Lin, (2017), 1705.06016.

[83] C. Weisbuch and B. Vinter, *Quantum Semiconductor Structures: Fundamentals and Applications* (Academic Press, San Diego, 1991).

[84] V. A. Saroka, M. V. Shuba, and M. E. Portnoi, Phys. Rev. B **95**, 155438 (2017).

[85] V. Saroka, Solving the Secular Equation for Zigzag and Bearded Graphene Nanoribbons, in *http://demonstrations.wolfram.com/SolvingTheSecularEquationForZigzagAndBeardedGrapheneNanoribb/*, Wolfram Demonstrations Project, 2017.

[86] V. Saroka, Optical Selection Rules for Zigzag Graphene Nanoribbons, in *http://demonstrations.wolfram.com/OpticalSelectionRulesForZigzagGrapheneNanoribbons/*, Wolfram Demonstrations Project, 2017.

[87] M. E. Portnoi, V. A. Saroka, R. R. Hartmann, and O. V. Kibis, Terahertz Applications of Carbon Nanotubes and Graphene Nanoribbons, in *2015 IEEE Comput. Soc. Annu. Symp. VLSI*, pp. 456–459, IEEE, 2015.

[88] V. A. Saroka, R. R. Hartmann, and M. E. Portnoi, Terahertz Transitions in Narrow-Gap Carbon Nanotubes and Graphene Nanoribbons, in *Physics, Chemistry and Applications of Nanostructures*, pp. 176–179, World Scientific, 2017.

[89] S. V. Rotkin and K. Hess, Appl. Phys. Lett. **84**, 3139 (2004).

[90] A. Srivastava, H. Htoon, V. I. Klimov, and J. Kono, Phys. Rev. Lett. **101**, 087402 (2008).

[91] C. Chang *et al.*, Carbon N. Y. **44**, 508 (2006).

[92] H. Abdelsalam, M. H. Talaat, I. Lukyanchuk, M. E. Portnoi, and V. A. Saroka, J. Appl. Phys. **120**, 014304 (2016).

[93] M. Fujita, K. Wakabayashi, K. Nakada, and K. Kusakabe, J. Phys. Soc. Japan **65**, 1920 (1996).

[94] D. Klein, Chem. Phys. Lett. **217**, 261 (1994).

[95] S. Kivelson and O. L. Chapman, Phys. Rev. B **28**, 7236 (1983).

[96] K. Tanaka, S. Yamashita, H. Yamabe, and T. Yamabe, Synth. Met. **17**, 143 (1987).

[97] Y. Miyamoto, K. Nakada, and M. Fujita, Phys. Rev. B **59**, 9858 (1999).

[98] K. Wakabayashi, M. Fujita, H. Ajiki, and M. Sigrist, Phys. Rev. B **59**, 8271 (1999).

[99] M.-F. Lin and F.-l. Shyu, J. Phys. Soc. Japan **69**, 3529 (2000).

[100] K. Wakabayashi, Phys. Rev. B **64**, 125428 (2001).

[101] L. Brey and H. A. Fertig, Phys. Rev. B **73**, 235411 (2006).

[102] K.-I. Sasaki, S. Murakami, and R. Saito, J. Phys. Soc. Japan **75**, 074713 (2006).

[103] Y.-W. Son, M. L. Cohen, and S. G. Louie, Nature **444**, 347 (2006).

[104] Y.-W. Son, M. L. Cohen, and S. G. Louie, Phys. Rev. Lett. **97**, 216803 (2006).

[105] M. Kohmoto and Y. Hasegawa, Phys. Rev. B **76**, 205402 (2007).

[106] L. Yang, C.-H. Park, Y.-W. Son, M. L. Cohen, and S. G. Louie, Phys. Rev. Lett. **99**, 186801 (2007).

[107] L. Malysheva and A. Onipko, Phys. Rev. Lett. **100**, 186806 (2008).

[108] A. Onipko, Phys. Rev. B **78**, 245412 (2008).

[109] K. Wakabayashi, K.-I. Sasaki, T. Nakanishi, and T. Enoki, Sci. Technol. Adv. Mater. **11**, 054504 (2010).

[110] S. Dutta and S. K. Pati, J. Mater. Chem. **20**, 8207 (2010).

[111] H. C. Chung, M. H. Lee, C. P. Chang, and M. F. Lin, Opt. Express **19**, 23350 (2011).

[112] K. Wakabayashi and S. Dutta, Solid State Commun. **152**, 1420 (2012).

[113] H.-Y. Deng, K. Wakabayashi, and C.-H. Lam, J. Phys. Soc. Japan **82**, 104707 (2013).

[114] H.-Y. Deng and K. Wakabayashi, Phys. Rev. B **90**, 115413 (2014).

[115] J. M. Luck and Y. Avishai, J. Phys. Condens. Matter **27**, 025301 (2015).

[116] L. Brey and H. A. Fertig, Phys. Rev. B **75**, 125434 (2007).

[117] H. Hsu and L. E. Reichl, Phys. Rev. B **76**, 045418 (2007).

[118] K.-I. Sasaki *et al.*, Phys. Rev. B **80**, 155450 (2009).

[119] Z. Duan, W. Liao, and G. Zhou, Adv. Condens. Matter Phys. **2010**, 258019 (2010).

[120] K.-I. Sasaki, K. Kato, Y. Tokura, K. Oguri, and T. Sogawa, Phys. Rev. B **84**, 085458 (2011).

[121] K. Gundra and A. Shukla, Phys. Rev. B **83**, 075413 (2011).

[122] G. D. Sanders, A. R. T. Nugraha, R. Saito, and C. J. Stanton, Phys. Rev. B **85**, 205401 (2012).

[123] G. D. Sanders *et al.*, J. Phys. Condens. Matter **25**, 144201 (2013).

[124] W. H. Zhu, G. H. Ding, and B. Dong, J. Appl. Phys. **113**, 103510 (2013).

[125] L. Yang, M. L. Cohen, and S. G. Louie, Nano Lett. **7**, 3112 (2007).

[126] D. Prezzi, D. Varsano, A. Ruini, A. Marini, and E. Molinari, Phys. Rev. B **77**, 041404 (2008).

[127] M. Berahman and M. H. Sheikhi, J. Comput. Theor. Nanosci. **8**, 90 (2011).

[128] K. Gundra and A. Shukla, Phys. B Condens. Matter **406**, 3538 (2011).

[129] A. Grüneis *et al.*, Phys. Rev. B **67**, 165402 (2003).

[130] R. Saito *et al.*, Appl. Phys. A Mater. Sci. Process. **78**, 1099 (2004).

[131] T. Ando, Y. Zheng, and H. Suzuura, J. Phys. Soc. Japan **71**, 1318 (2002).

[132] T. Ando, J. Phys. Soc. Japan **74**, 777 (2005).

[133] C. T. White, J. Li, D. Gunlycke, and J. W. Mintmire, Nano Lett. **7**, 825 (2007).

[134] H. Ajiki and T. Ando, Phys. B Condens. Matter **201**, 349 (1994).

[135] J. Jiang, R. Saito, A. Grüneis, G. Dresselhaus, and M. Dresselhaus, Carbon N. Y. **42**, 3169 (2004).

[136] S. V. Goupalov, Phys. Rev. B **72**, 195403 (2005).

[137] E. Malić, M. Hirtschulz, F. Milde, A. Knorr, and S. Reich, Phys. Rev. B **74**, 195431 (2006).

[138] A. Zarifi and T. G. Pedersen, Phys. Rev. B **80**, 195422 (2009).

[139] S. Compernolle, L. Chibotaru, and A. Ceulemans, J. Chem. Phys. **119**, 2854 (2003).

[140] L. Molinari, J. Phys. A. Math. Gen. **30**, 983 (1997).

[141] E. H. Kerner, Phys. Rev. **95**, 687 (1954).

[142] H. Schmidt, Phys. Rev. **105**, 425 (1957).

[143] J.-I. Hori and T. Asahi, Prog. Theor. Phys. **17**, 523 (1957).

[144] H. Matsuda, Prog. Theor. Phys. Suppl. **23**, 22 (1962).

[145] J. E. Lennard-Jones, Proc. R. Soc. A Math. Phys. Eng. Sci. **158**, 280 (1937).

[146] C. A. Coulson, Proc. R. Soc. A Math. Phys. Eng. Sci. **164**, 383 (1938).

[147] M. M. Mestechkin, J. Chem. Phys. **122**, 074305 (2005).

[148] D. E. Rutherford, Proc. R. Soc. Edinburgh. Sect. A. Math. Phys. Sci. **62**, 229 (1948).

[149] D. E. Rutherford, Proc. R. Soc. Edinburgh. Sect. A. Math. Phys. Sci. **63**, 232 (1952).

[150] T. Muir, *A Treatise on the Theory of Determinants* (Dover Publications, New York, 1960).

[151] L. D. Landau and E. M. Lifshitz, *Quantum Mechanics. Non-relativistic theory (Volume 3 of Course of Theoretical Physiscs)*, 3rd ed. (Pergamon Press, Oxford, 1977).

[152] E. Blount, Formalisms of Band Theory, in *Solid State Phys.*, edited by F. Seitz and D. Turnbull Vol. 13, pp. 305–373, Academic Press, New York, 1962.

[153] L. G. Johnson and G. Dresselhaus, Phys. Rev. B **7**, 2275 (1973).

[154] L. C. Lew Yan Voon and L. R. Ram-Mohan, Phys. Rev. B **47**, 15500 (1993).

[155] M. F. Lin and K. W. K. Shung, Phys. Rev. B **50**, 17744 (1994).

[156] A. Anselm, *Introduction to Semiconductor Treory*, 2nd ed. (Mir Publishers, Moscow, 1981).

[157] T. Ando, J. Phys. Soc. Japan **75**, 124701 (2006).

[158] H. Ajiki and T. Ando, J. Phys. Soc. Japan **62**, 1255 (1993).

[159] H. Ajiki and T. Ando, J. Phys. Soc. Japan **65**, 505 (1996).

[160] J. J. Palacios, J. Fernández-Rossier, L. Brey, and H. A. Fertig, Semicond. Sci. Technol. **25**, 033003 (2010).

[161] M. E. Portnoi, M. Rosenau da Costa, O. V. Kibis, and I. A. Shelykh, Int. J. Mod. Phys. B **23**, 2846 (2009).

[162] R. Moradian, R. Chegel, and S. Behzad, Phys. E Low-dimensional Syst. Nanostructures **42**, 1850 (2010).

[163] R. Chegel and S. Behzad, Opt. Commun. **313**, 406 (2014).

[164] Y. Oyama *et al.*, Carbon N. Y. **44**, 873 (2006).

[165] T. Vuković, I. Milošević, and M. Damnjanović, Phys. Rev. B **65**, 045418 (2002).

[166] R. Loudon, Am. J. Phys. **27**, 649 (1959).

[167] L. Yang, M. L. Cohen, and S. G. Louie, Phys. Rev. Lett. **101**, 186401 (2008).

[168] Y. Lu, W. Lu, W. Liang, and H. Liu, Phys. Rev. B **88**, 165425 (2013).

[169] T. Ando, J. Phys. Soc. Japan **66**, 1066 (1997).

[170] J. Jiang *et al.*, Phys. Rev. B **75**, 035407 (2007).

[171] R. R. Hartmann, I. A. Shelykh, and M. E. Portnoi, Phys. Rev. B **84**, 035437 (2011).

[172] L. Bányai, I. Galbraith, C. Ell, and H. Haug, Phys. Rev. B **36**, 6099 (1987).

[173] T. Ogawa and T. Takagahara, Phys. Rev. B **43**, 14325 (1991).

[174] T. Ogawa and T. Takagahara, Phys. Rev. B **44**, 8138 (1991).

[175] F. Wang, G. Dukovic, L. E. Brus, and T. F. Heinz, Science **308**, 838 (2005).

[176] J. Shaver *et al.*, Nano Lett. **7**, 1851 (2007).

[177] G. G. Samsonidze *et al.*, J. Nanosci. Nanotechnol. **3**, 431 (2003).

[178] W. Izumida, R. Okuyama, A. Yamakage, and R. Saito, Phys. Rev. B **93**, 195442 (2016).

[179] H. Y. Deng and K. Wakabayashi, Phys. Rev. B **91**, 035425 (2015).

[180] R. Elliott, Phys. Rev. **108**, 1384 (1957).

[181] R. Elliott and R. Loudon, J. Phys. Chem. Solids **15**, 196 (1960).

[182] K. Batrakov, S. Maksimenko, P. Kuzhir, and C. Thomsen, Phys. Rev. B **79**, 125408 (2009), 0807.3091.

[183] V. Ryzhii, A. A. Dubinov, V. Y. Aleshkin, M. Ryzhii, and T. Otsuji, Appl. Phys. Lett. **103**, 163507 (2013).

[184] D. Svintsov, V. Ryzhii, A. Satou, T. Otsuji, and V. Vyurkov, Opt. Express **22**, 19873 (2014).

[185] O. V. Kibis, D. G. W. Parfitt, and M. E. Portnoi, Phys. Rev. B **71**, 035411 (2005).

[186] O. V. Kibis, M. Rosenau da Costa, and M. E. Portnoi, Nano Lett. **7**, 3414 (2007).

[187] M. Portnoi, O. Kibis, and M. Rosenau da Costa, Superlattices Microstruct. **43**, 399 (2008).

[188] T. P. Collier, V. A. Saroka, and M. E. Portnoi, Tuning THz Transitions in a Quantum Ring with Two Gates, in *Physics, Chemistry and Applications of Nanostructures*, pp. 172–175, World Scientific, 2017.

[189] J.-C. Charlier and S. Roche, Rev. Mod. Phys. **79**, 677 (2007).

[190] R. R. Hartmann and M. E. Portnoi, *Optoelectronic Properties of Carbon-based Nanostructures: Steering electrons in graphene by electromagnetic fields* (Lambert Academic Publishing, Saarbrucken, 2011).

[191] L. Matthes, P. Gori, O. Pulci, and F. Bechstedt, Phys. Rev. B **87**, 035438 (2013).

[192] C. T. White, J. Li, D. Gunlycke, and J. W. Mintmire, Nano Lett. **7**, 825 (2007).

[193] H. Zheng, Z. Wang, T. Luo, Q. Shi, and J. Chen, Phys. Rev. B **75**, 165414 (2007).

[194] D. Gunlycke and C. T. White, Phys. Rev. B **77**, 115116 (2008).

[195] M. Dvorak, W. Oswald, and Z. Wu, Sci. Rep. **3**, 2289 (2013).

[196] E. V. Castro *et al.*, Phys. Rev. Lett. **99**, 216802 (2007).

[197] A. B. Kuzmenko, I. Crassee, D. van der Marel, P. Blake, and K. S. Novoselov, Phys. Rev. B **80**, 165406 (2009).

[198] T. Khodkov, I. Khrapach, M. F. Craciun, and S. Russo, Nano Lett. **15**, 4429 (2015).

[199] T. Kampfrath *et al.*, Phys. Rev. Lett. **101**, 267403 (2008).

[200] A. Ugawa, A. G. Rinzler, and D. B. Tanner, Phys. Rev. B **60**, R11305 (1999).

[201] G. Y. Slepyan, M. V. Shuba, S. A. Maksimenko, C. Thomsen, and A. Lakhtakia, Phys. Rev. B **81**, 205423 (2010).

[202] M. V. Shuba *et al.*, Phys. Rev. B **85**, 165435 (2012).

[203] L. Ren *et al.*, Phys. Rev. B **87**, 161401 (2013).

[204] J.-Y. Park *et al.*, Nano Lett. **4**, 517 (2004).

[205] L. V. Titova *et al.*, Nano Lett. **15**, 3267 (2015).

[206] R. Denk *et al.*, Nat. Commun. **5**, 4253 (2014).

[207] L. A. Chernozatonskii, P. B. Sorokin, and J. W. Bruning, Appl. Phys. Lett. **91**, 183103 (2007).

[208] L. A. Chernozatonskii and P. B. Sorokin, J. Phys. Chem. C **114**, 3225 (2010).

[209] Y. Yao, F. Ye, X. L. Qi, S. C. Zhang, and Z. Fang, Phys. Rev. B **75**, 041401R (2007).

[210] N. A. Merkulov, V. I. Perel, and M. E. Portnoi, JEPT **72**, 669 (1991).

[211] T. Cao *et al.*, Nat. Commun. **3**, 887 (2012).

[212] W. Yao, D. Xiao, and Q. Niu, Phys. Rev. B **77**, 235406 (2008).

[213] G. Giovannetti, P. A. Khomyakov, G. Brocks, P. J. Kelly, and J. van den Brink, Phys. Rev. B **76**, 073103 (2007).

[214] S. Y. Zhou *et al.*, Nat. Mater. **6**, 916 (2007).

[215] A. Mattausch and O. Pankratov, Phys. Rev. Lett. **99**, 076802 (2007).

[216] Z. Ni *et al.*, Nanoscale **6**, 7609 (2014).

[217] W.-F. Tsai *et al.*, Nat. Commun. **4**, 1500 (2013).

[218] S. B. Kumar and J. Guo, Appl. Phys. Lett. **98**, 222101 (2011).

[219] L. Liang and V. Meunier, Phys. Rev. B **86**, 195404 (2012).

[220] V. I. Artyukhov and L. Chernozatonskii, J. Phys. Chem. C **114**, 9678 (2010).

[221] C. H. Lui, Z. Li, K. F. Mak, E. Cappelluti, and T. F. Heinz, Nat. Phys. **7**, 944 (2011).

[222] I. A. Luk'yanchuk, Y. Kopelevich, and M. El Marssi, Phys. B Condens. Matter **404**, 404 (2009).

[223] M. Ezawa, J. Supercond. Nov. Magn. **28**, 1249 (2015).

[224] E. McCann and M. Koshino, Rep. Prog. Phys. **76**, 056503 (2013).

[225] T. Ohta, A. Bostwick, T. Seyller, K. Horn, and E. Rotenberg, Science **313**, 951 (2006).

[226] M. Koshino, New J. Phys. **15**, 015010 (2013).

[227] A. G. Kvashnin, D. G. Kvashnin, O. P. Kvashnina, and L. A. Chernozatonskii, Nanotechnology **26**, 385705 (2015).

[228] P. B. Sorokin, P. V. Avramov, L. a. Chernozatonskii, D. G. Fedorov, and S. G. Ovchinnikov, J. Phys. Chem. A **112**, 9955 (2008).

[229] B. Sahu, H. Min, A. MacDonald, and S. Banerjee, Phys. Rev. B **78**, 045404 (2008).

[230] B. Sahu, H. Min, and S. K. Banerjee, Phys. Rev. B **81**, 045414 (2010).

[231] W. J. Yu and X. Duan, Sci. Rep. **3**, 1248 (2013).

[232] Y. C. Huang, C. P. Chang, and M. F. Lin, J. Appl. Phys. **104**, 103714 (2008).

[233] M. Ezawa, Phys. Rev. B **76**, 245415 (2007).

[234] Z. Z. Zhang, K. Chang, and F. M. Peeters, Phys. Rev. B **77**, 235411 (2008).

[235] L. A. Chernozatonskii, D. G. Kvashnin, O. P. Kvashnina, and N. A. Konstantinova, J. Phys. Chem. C **118**, 1318 (2014).

[236] J. Fernández-Rossier and J. J. Palacios, Phys. Rev. Lett. **99**, 177204 (2007).

[237] P. Potasz, A. D. Güçlü, and P. Hawrylak, Phys. Rev. B **81**, 033403 (2010).

[238] D. P. Kosimov, A. A. Dzhurakhalov, and F. M. Peeters, Phys. Rev. B **81**, 195414 (2010).

[239] T. Espinosa-Ortega, I. A. Luk'Yanchuk, and Y. G. Rubo, Superlattices Microstruct. **49**, 283 (2011).

[240] T. Espinosa-Ortega, I. A. Luk'yanchuk, and Y. G. Rubo, Phys. Rev. B **87**, 205434 (2013).

[241] H. Abdelsalam, T. Espinosa-Ortega, and I. Luk'yanchuk, Low Temp. Phys. **41**, 396 (2015).

[242] I. Ozfidan, A. D. Güçlü, M. Korkusinski, and P. Hawrylak, Phys. status solidi - Rapid Res. Lett. **10**, 102 (2016).

[243] M. Zarenia, A. Chaves, G. A. Farias, and F. M. Peeters, Phys. Rev. B **84**, 245403 (2011).

[244] D. da Costa, M. Zarenia, A. Chaves, G. Farias, and F. Peeters, Carbon N. Y. **78**, 392 (2014).

[245] A. D. Güçlü, P. Potasz, and P. Hawrylak, Phys. Rev. B **84**, 035425 (2011), 1104.3108.

[246] H. Abdelsalam, T. Espinosa-Ortega, and I. Lukyanchuk, Superlattices Microstruct. **87**, 137 (2015).

[247] D. R. da Costa, M. Zarenia, A. Chaves, G. A. Farias, and F. M. Peeters, Phys. Rev. B **92**, 115437 (2015).

[248] D. R. da Costa, M. Zarenia, A. Chaves, G. A. Farias, and F. M. Peeters, Phys. Rev. B **93**, 085401 (2016).

[249] T. Yamamoto, T. Noguchi, and K. Watanabe, Phys. Rev. B **74**, 121409 (2006).

[250] M. Ezawa, New J. Phys. **14**, 033003 (2012), 1201.3687.

[251] S. Lee *et al.*, Phys. Rev. B **66**, 235307 (2002).

[252] K. Leung and K. B. Whaley, Phys. Rev. B **56**, 7455 (1997).

[253] K. Leung, S. Pokrant, and K. B. Whaley, Phys. Rev. B **57**, 12291 (1998).

[254] S. Schulz, S. Schumacher, and G. Czycholl, Phys. Rev. B **73**, 245327 (2006).

[255] A. Castellanos-Gomez *et al.*, 2D Mater. **1**, 025001 (2014).

[256] Y. Y. Li, M. X. Chen, M. Weinert, and L. Li, Nat. Commun. **5**, 4311 (2014).

[257] J. Qiao, X. Kong, Z.-X. Hu, F. Yang, and W. Ji, Nat. Commun. **5**, 4475 (2014).

[258] P. Miró, M. Audiffred, and T. Heine, Chem. Soc. Rev. **43**, 6537 (2014).

[259] F. Schwierz, R. Granzner, and J. Pezoldt, Nanoscale **7**, 8261 (2015).

[260] M. Salmani-Jelodar, S. Kim, K. Ng, and G. Klimeck, Appl. Phys. Lett. **105**, 083508 (2014).

[261] X. Jia *et al.*, Science **323**, 1701 (2009).

[262] Z. Sun *et al.*, Angew. Chemie Int. Ed. **54**, 11526 (2015).

[263] P. Masih Das *et al.*, ACS Nano **10**, 5687 (2016).

[264] X. Niu, Y. Li, H. Shu, and J. Wang, J. Phys. Chem. Lett. **7**, 370 (2016).

[265] M. M. Grujić, M. Ezawa, M. Ž. Tadić, and F. M. Peeters, Phys. Rev. B **93**, 245413 (2016).

[266] H. von Koch, Ark. Mat. **1**, 681 (1904).

[267] V. Saroka, Koch Curve Randomization and Crystal Edge Disorder, in *http://demonstrations.wolfram.com/KochCurveRandomizationAndCrystalEdgeDisorder/*, Wolfram Demonstrations Project, 2017.

[268] H. Haug and S. W. Koch, *Quantum Theory of the Optical and Electronic Properties of Semiconductors*, 4th ed. (World Scientific Publishing Co. Pte. Ltd., Singapore, 2003).

[269] G. Montambaux, F. Piéchon, J.-N. Fuchs, and M. O. Goerbig, Phys. Rev. B **80**, 153412 (2009).

[270] V. Pereira and A. Castro Neto, Phys. Rev. Lett. **103**, 046801 (2009).

[271] L. Matthes, O. Pulci, and F. Bechstedt, Phys. Rev. B **94**, 205408 (2016).

[272] H. Guo, N. Lu, J. Dai, X. Wu, and X. C. Zeng, J. Phys. Chem. C **118**, 14051 (2014).

[273] V. Sorkin, Y. Cai, Z. Ong, G. Zhang, and Y. W. Zhang, Crit. Rev. Solid State Mater. Sci. **42**, 1 (2017).

[274] D. Golberg, Y. Bando, C. C. Tang, and C. Y. Zhi, Adv. Mater. **19**, 2413 (2007).

[275] J. Deslippe, C. D. Spataru, D. Prendergast, and S. G. Louie, Nano Lett. **7**, 1626 (2007).

[276] F. Wang *et al.*, Phys. Rev. Lett. **99**, 227401 (2007).

[277] K. Wakabayashi and K. Harigaya, J. Phys. Soc. Japan **72**, 998 (2003), 0210685.

[278] Z. L. Guo, Z. R. Gong, H. Dong, and C. P. Sun, Phys. Rev. B **80**, 195310 (2009), 0906.1634.

[279] E. W. S. Caetano, V. N. Freire, S. G. Dos Santos, D. S. Galvão, and F. Sato, J. Chem. Phys. **128**, 164719 (2008), 0903.2080.

[280] E. W. S. Caetano *et al.*, Langmuir **25**, 4751 (2009).

[281] T. Korhonen and P. Koskinen, Comput. Mater. Sci. **81**, 264 (2014).

[282] D. M. Walba, R. M. Richards, and R. C. Haltiwanger, J. Am. Chem. Soc. **104**, 3219 (1982).

[283] R. Vaxenburg, A. Rodina, A. Shabaev, E. Lifshitz, and A. L. Efros, Nano Lett. **15**, 2092 (2015).

[284] M. Achermann, A. P. Bartko, J. A. Hollingsworth, and V. I. Klimov, Nat. Phys. **2**, 557 (2006).

[285] V. Kharchenko and M. Rosen, J. Lumin. **70**, 158 (1996).

[286] P. Roussignol *et al.*, Appl. Phys. Lett. **51**, 1882 (1987).

[287] F. Wang, Y. Wu, M. S. Hybertsen, and T. F. Heinz, Phys. Rev. B **73**, 245424 (2006).

[288] K. Bulashevich, R. Suris, and S. Rotkin, Int. J. . . . (2003).

[289] T. Pedersen, Phys. Rev. B **67**, 2 (2003).

[290] R. H. Dicke, Phys. Rev. **93**, 99 (1954).

[291] F. Xia, M. Steiner, Y.-M. Lin, and P. Avouris, Nat. Nanotechnol. **3**, 609 (2008).

[292] D. Legrand *et al.*, Appl. Phys. Lett. **102**, 153102 (2013).

[293] R. Miura *et al.*, Nat. Commun. **5**, 5580 (2014).

[294] A. Graf, L. Tropf, Y. Zakharko, J. Zaumseil, and M. C. Gather, Nat. Commun. **7**, 13078 (2016).

[295] O. Voznyy, A. D. Güçlü, P. Potasz, and P. Hawrylak, Phys. Rev. B **83**, 165417 (2011).

[296] P. Bugajny, L. Szulakowska, B. Jaworowski, and P. Potasz, Phys. E Low-Dimensional Syst. Nanostructures **85**, 294 (2017).

[297] B. Jaworowski, P. Potasz, and A. Wójs, Superlattices Microstruct. **64**, 44 (2013).

[298] S. Yuan, A. N. Rudenko, and M. I. Katsnelson, Phys. Rev. B - Condens. Matter Mater. Phys. **91**, 1 (2015), 1411.1681.

[299] A. Arbouet *et al.*, Phys. Rev. Lett. **93**, 127401 (2004).

[300] T. Devkota, M. S. Devadas, A. Brown, J. Talghader, and G. V. Hartland, Appl. Opt. **55**, 796 (2016).

[301] W. Izumida, R. Okuyama, and R. Saito, Phys. Rev. B **91**, 235442 (2015).